Struvite Precipitation modelling using Extended Quadrature Method of Moments and Drift-Flux Model

Submitted by

Bernardas Jankauskas

to the University of Exeter as a thesis for the degree of Doctor of Philosophy in Engineering, September 2019.

This thesis is available for Library use on the understanding that it is copyright material and that no quotation from the thesis may be published without proper acknowledgement.

I certify that all material in this thesis which is not my own work has been identified and that no material has previously been submitted and approved for the award of a degree by this or any other University.

.....

Bernardas Jankauskas

Abstract

The primary fertilisers used in the agricultural industry are phosphorus based. The production of phosphorus is mainly based on the mining operations, however it is a current consensus that in $50 - 100$ years time the quality and the availability of phosphorus ores will decrease substantially and the deposits will be either completely depleted or the quality of the obtainable phosphorus will be too toxic to be used in the agriculture. Taking into account the current population growth trends the food production will have to be increased even more and therefore the global food shortage is an event of high potential. To address that alternative sources of phosphorus based fertilisers must be found and numerous technological research have been taking place to limit the impact that phosphorus shortage might cause in the future.

The aim of this study is to present a potential technology that could be used for phosphorus recovery. It is known that there is a significant amount of phosphorus in the wastewater therefore most of the technological developments have been focussed towards the recovery of phosphorus from the wastewater streams. The Hydrodynamic Vortex Separator (HDVS) is a product developed by Hydro International®that is primarily used for solid-liquid separation. However this study proposes the potential use of the HDVS as a reaction vessel for phosphorus recovery through magnesium-ammonium-phosphate precipitation.

The study presents a development and application of a mathematical model of the two-phase system that is coupled with the formation of a dispersed phase through a precipitation process. Hydrodynamics of the system is modelled using an Eulerian

approach, specifically the drift flux mixture model (DFM)[81]. The precipitation process and the change of the dispersed phase properties, namely the mean diameter of the particulates, is modelled using the Population Balance Equation (PBE)[115], which is solved using the Extended Quadrature Method of Moments (EQMOM) method [149]. The affects of the changes observed in the dispersed phase properties were coupled to the hydrodynamics using two new settling models that depend on the size of the particulate phase.

The model has been applied to a horizontal settling tank and the HDVS geometries in order to understand the potential of the precipitation process in these type of wastewater treatment tools. In both of the cases the model predicted reasonable values of the dispersed phase mean diameter.

Acknowledgements

I would like to express my gratitude to my supervisors Prof. Gavin Tabor and Dr. Daniel Jarman for their support throughout the course of this project and the opportunity to work on a challenging and interesting project.

I am also indebted to my colleagues and now friends at the research group. Especially I would like to thank Dr. Recep Kahraman and Matthew Riella, it would not have been achieved without those coffee breaks during which the most useful ideas have come into existence.

Furthermore I would like to acknowledge the STREAM Industrial Doctorate Centre for Water Sector that made this whole project possible. The range of skills and opportunities that have been provided over the course of this PhD have helped to develop necessary skills for this project.

Last but not least I would also like to express my greatest gratitude to my parents Vilma Jankauskienė and Rytis Jankauskas for their constant support, encouragement and pushing me to go forwards at each step of this journey. I am indebted for life for everything that they have done for me.

Contents

Nomenclature

Greek letters

α_d Dispersed phase volume fraction

α_l Liquid phase volume fraction

$\beta(\xi, \xi')$ Aggregation kernel

$\delta_\alpha(\xi - \xi_\alpha)$ Dirac-delta

$\delta_\sigma(\xi, \xi_\alpha)$ Kernel density function

γ_i Activity coefficient of species i

μ Fluid viscosity

μ_m Mixture viscosity

μ_k kth moment of the size distribution function

ν Kinematic viscosity

Ω Supersaturation ratio

ω Activity coefficient

ω_α Quadrature weight

ϕ_a Surface shape factor

ϕ_v Volume shape factor

ρ Density

ρ_d Dispersed phase density

ρ_l Liquid phase density

σ Relative saturation

ξ Internal coordinate of the number density function

ξ_α Quadrature abscissa

Roman letters

$\mathbf{a}$ General vector quantity

$\mathbf{U}$ Velocity vector

$\mathbf{U}_m$ Mixture velocity vector

$\mathbf{U}_0$ Terminal velocity vector

$\mathbf{U}_{dr,d}$ Drift velocity vector

$\{A\}$ Ionic activity

$a(\xi)$ Breakage kernel

A_{DH} Debye-Hückel constant

C Molar concentration

c Mass concentration

d_{32} Sauter mean diameter

G Growth rate

g Gravity

G_{Gibbs} Gibbs free energy

I Ionic strength

IAP Ionic activity product

J Nucleation rate

K Equilibrium constant

k_B Boltzmann constant

K_{SP} Equilibrium solubility product

$n(\xi, \mathbf{x}, t)$ Number density function

P Pressure

P_m Mixture pressure

S Absolute saturation

SI Saturation Index

Y Transported species

Z Ionic charge

Subscripts

agg Aggregation

br Breakage

c Continuous phase

d Dispersed phase

l Liquid phase

m Mixture

eq Equilibrium

Superscripts

a Aggregation

br Breakage

T Total

Acronyms

$ASMM$ Algebraic slip mixture model

CM Classes Method

CSD Crystal size distribution

CV Control Volume

DFM Drift Flux Model

$DPBM$ Discrete Poplation Balance Method

$DQMOM$ Direct Quadrature Method of Moments

$EQMOM$ Extended Quadrature Method of Moments

FBR Fluidised Bed Reactor

FV Finite Volume

$HDVS$ Hydrodynamic Vortex Separator

MAP Magnesium Ammonium Phosphate

MC Monte Carlo method

ME Multi Environment

MOM Method of Moments

NDF Number density function

PBE Population Balance Equation

PBM Population Balance Model

$PISO$ Pressure Implicit with Splittin of Operators

$QMOM$ Quadrature Method of Moments

TFM Two-Fluid Model

$WWTP$ Wastewater Treatment Plant

List of Figures

List of Tables

Chapter 1

Introduction

1.1 Project motivation

Phosphorus and nitrogen are crucial part of agriculture as these elements are used as fertilisers for the produce. Currently the primary way to produce phosphorus ore is through mining the deposits that have been formed through millions of years below the surface of the Earth. There is however one issue with this method - just like in a case of any fixed resource, these ore deposits are limited and will run out eventually. In addition to that, the largest amounts of accessible phosphorus is scattered along a small number of locations around the world, which, when the phosphorus deposits starts to run out, will lead to political and economical tensions around the world. This can all be avoided if alternative and more sustainable sources for phosphorus and other agriculturally important fossil ores are found and extraction methods are developed.

Currently one of the most promising areas for producing nutrients is through their recovery from wastewater. Substantial amounts of nutrients are contained in the wastewater and for the most part these are not being recovered from it and landfilled together with the waste products. In addition excessive amounts of phosphorus, nitrogen and magnesium in the wastewater influent tends to cause spontaneous precipitation of the magnesium ammonium phosphate which creates scaling on the

treatment plant pipes and eventually requires interruption in the treatment plant operation in order to clear these deposits. Therefore there is an economical interest from the Wastewater Treatment Plant (WWTP) operators to prevent that in order for the treatment plant to operate with no unnecessary stoppage. In addition, recovery of the nutrients in a fertiliser form would create a useful revenue stream for the plant that could potentially mean that the operation would be profitable.

A brief overview of the possible recovery methods will be covered in the following section, however it is deemed that recovery through reactive crystallisation or precipitation is a very attractive avenue due to the time scales that the process takes, e.g. crystallisation plants have to operate for a matter of days in order to obtain a good quality products whereas precipitation processes usually occur at the time-scales lower than an hour, therefore a product can be produced at a much quicker rates.

1.2 Aim of the project

This project has been proposed by the Hydro International®that specialise in primary wastewater treatment. One of the main product range developed by Hydro International®are the Hydrodynamic Vortex Separators - passive solid-liquid separators. Basic diagram of the HDVS is shown in Figure 1.1. The main idea behind the project was to use Computational Fluid Dynamics (CFD) modelling in order to investigate the viability of a vortex separator as a reaction vessel for the precipitation of magnesium ammonium phosphate. The precipitation process of struvite is complex, involving multiple length and time-scales and, from the physics perspective, still not very well understood. Therefore the modelling methodology has to cover all necessary length and time-scales at an appropriate accuracy. One approach to capture all important processes at all of the scales would be to model the system using the Direct Numerical Simulation (DNS), however it is currently not a viable option as it requires very large computing capabilities and therefore is not possible to use when it comes down to the complex geometries such as HDVS.

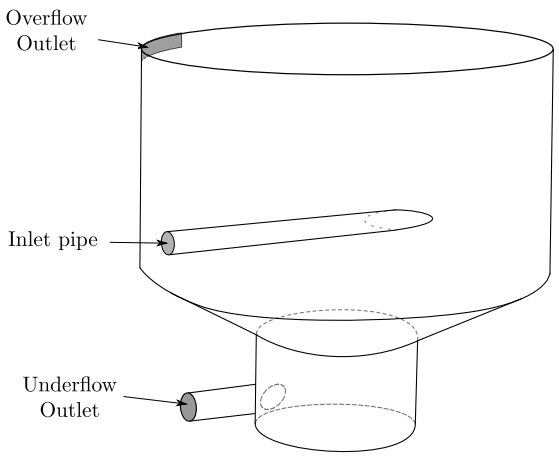

Figure 1.1: Diagram showing typical geometry of the hydrodynamic vortex separator

The alternative would be to solely rely on the macroscale formulation of the problem, however during precipitation process the solid phase quality parameters are also evolving with time (e.g. the size of the particulates are changing). Using the macroscale approach would mean that these internal changes of the particulate phase would have to be either modelled of assumed to be constant which would then reduce the physical reliability of the model. Marchisio and Fox [85] discusses another type of formulation - mesoscale models that stand in between the micro and macro scale formulations. The schematic representation is shown in Figure 1.2. In mesoscale formulations the dispersed phase is essentially treated as a stochastic representation of the kinetic equation solution, whereas the macroscale approach of the multiphase system the dispersed phase is treated by employing the hydrodynamic description to it. The benefit of the mesoscale models stems from the fact that it allows to track the evolution of the internal changes of the dispersed phase which is one of the main interests in the precipitation process modelling.

The primary aim of this research project was formulated as follows: "to write a computational framework capable of simulating precipitation processes, specifically struvite precipitation. The framework should be able to capture physics at all length scales referred to as micro, macro, meso scales". In order to know whether the aim was achieved a set of specific goals have been formulated as follows:

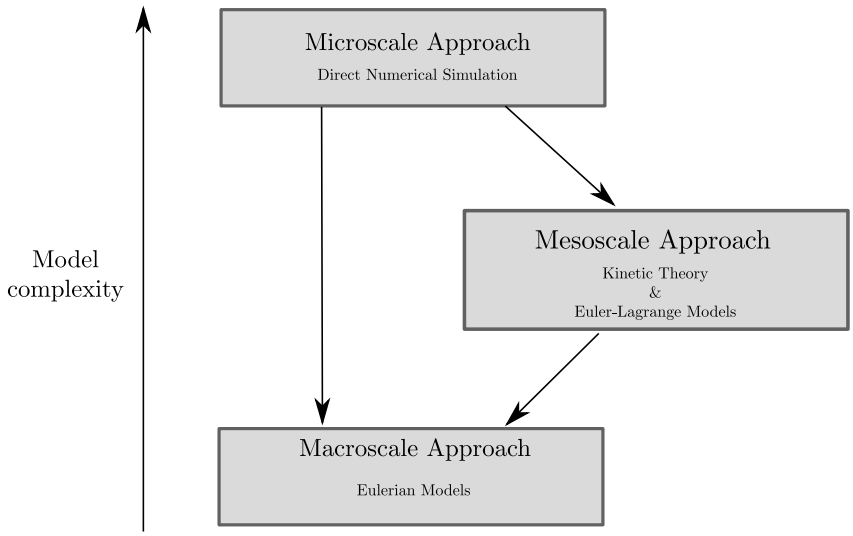

Figure 1.2: Schematic showing modelling framework of dispersed flows (adapted from Marchisio and Fox [85])

- Formulate a computational framework for struvite precipitation processes that would incorporate the hydrodynamics, equilibrium thermodynamics and dispersed phase evolution modelling;
- Verify the framework performance where possible;
- Apply the built tools to a set of test cases: two-dimensional setling tank geometry, the HDVS geometry.

1.3 Contributions and novelties of this work

Literature review of research on precipitation processes of different materials has shown that there is a significant lack of a complete and versatile framework capable of capturing different stages of such complex processes. None of the available computational tools are capable in capturing all three pilars of precipitation process: 1) physics of hydrodynamics; 2) equilibrium thermodynamics of chemical ionic species; 3) evolution of the dispersed phase that is created due to reactive process taking place.

Therefore the principal contribution of this research project is to fill this gap by

providing a framework that is capable of capturing all layers of physics involved.

This work also proposes two new settling velocity models for dispersed phase in the system. The need for such extension stems from the fact that up until this point there is no complete computational toolkit that deals with multiphase hydrodynamics where dispersed phase size distribution is varying over time. Proposed settling velocity models allow these details to be captured and therefore gives a better representation of physics in the systems where precipitation processes occur.

1.4 Thesis layout

This thesis is organised in the following manner:

- Chapter 2 covers the literature survey and discusses the methodologies chosen for the project.
- Chapter 3 provides fundamentals of the mathematical formulations of the multiphase flow, precipitation kinetics and thermodynamics. Finally the chapter covers the mathematical formulation behind the population balance modelling and specifically the methods of moments.
- Chapter 4 covers the background of the finite volume discretisation procedures and the numerical intricacies behind the Extended Quadrature Method of Moments.
- Chapter 5 is dedicated to the verification studies of the solver against the one dimensional semi-analytical solutions. Different kinetic models from the literature were compared and effects of the appropriate equilibrium thermodynamics are discussed.
- Chapter 6 presents the results from the horizontal settling tank by Dahl [35] and the hydrodynamic vortex separator simulations.
- Chapter 7 summarises the work done, the results and the insights drawn from the work. Finally the chapter covers the future avenues that require

exploration.

Chapter 2

Literature review

2.1 Global outlook of phosphorus

Since the discovery of elemental form of phosphorus by Brandtl in 1669 it has retained the interest of people [46]. It was initially thought that phosphorus would be the so called "philosopher's stone" as it was postulated that it should possess the ability to transform any metal to gold. This turned out not to be true, however in mid 19th century a more important discovery was made by Justus von Leibig. His research confirmed that plant growth rate is affected by inorganic salts such as phosphorus and nitrogen. This discovery meant that the value of phosphorus as a valuable material has grown significantly. Fast forwarding to the current date: the world population has passed the 7.6 billion mark and is estimated to reach 9 billion by the year 2050. Such projection implies that food production will have to be increased by 30% and with 90% of total mined phosphorus being used in agriculture this means that even more will need to be produced [32, 38, 127]. It is estimated that in order to satisfy the growing demand for food, the overall phosphorus production will have to increase 70% and even by 100% in developing countries [49].

Similarly to crude oil, phosphorus is not a renewable resource because rock deposits of phosphorus have formed over a period of $10-15$ million years [8]. An exact date

when these deposits will be exhausted is not clear and this topic causes heated debates all over the world. Since 2008, more and more pessimistic predictions for the amount of high quality phosphorus accessible through mining have been proposed. The latest consensus is that the main deposits will be exhausted within 50 to 100 years [32]. In addition to the depletion of currently existing ore deposits it is also reported that the quality of the products are declining and it is known that currently only 20% of produced phosphorus is acceptable for use in agriculture. Some authors estimate that by year 2200 none of the deposits will contain satisfactory quality ores. In addition, the mined products will contain large quantities of heavy metals (eg. cadmium) and radioactive elements (eg. radon, uranium)[31, 70, 127].

Concerns mentioned above are amplified on a geopolitical scale due to the fact that the largest phosphorus ore reserves are located in a small number of countries around the world. United States, China, Morocco, South Africa and Jordan contain the main global phosphate rock deposits [127]. Phosphorus scarcity concerns in combination with the 2008 recession have resulted in a spike in the global phosphorus price. This relatively 'short' crisis period has already had an impact on the phosphorus industry. China has started imposing a 135% export tariff on phosphates in order to preserve local reserves, consequentially halting its exports. The US has only decades left of phosphorus in its reserves even though it was previously regarded as the largest exporter, importer, producer and consumer country of phosphorus [32, 67, 70, 127].

All of the aforementioned concerns have to be taken seriously and awareness has to be raised, so that a sustainable solution can be established and followed through. A possible sustainable solution would be to rely on creating phosphorus (as well as nitrogen) recovery methods from wastewater, as it is known that wastewater is rich in this material and currently most of it ends up in landfill. Currently the laws in European Union prohibit land-filling of sludge that is not applicable in agriculture. In addition, the European Water Framework Directive in 2000/60/EC imposes maximum allowed treated wastewater effluent limits of $< 2.2mg/L$ for nitrates and $< 0.15mg/L$ for phosphates [31]. To address these imposed restrictions and

requirements in the next section we will cover the issues that arise when large phosphate levels are present in wastewater and treated sludge.

2.1.1 Phosphorus in wastewater

It has been known for centuries that bone meal is exceptionally good for use as a fertiliser. In fact, we now know that it contains large amounts of both organic and inorganic phosphorus. Globally, bonemeal production is small and not sufficient to use as a long-term solution. On the other hand sewage sludge is produced in large quantities everywhere on the world, therefore it is regarded as a very promising source of phosphates [8, 33].

Regulations regarding phosphate and nitrate effluent concentrations mentioned above are being imposed due to several reasons. Wastewater effluent stream containing high levels of phosphorus can increase the level of eutrophication when brought to water bodies such as the natural reservoirs, sea, rivers. Eutrophication is a process in which the water body is enriched with dissolved nutrients (eg. phosphorus) which in turn stimulates growth of organisms such as algea. If the area affected is left untreated for an extended period of time it eventually creates dead zones where regular flora and fauna cannot survive [8].

Additionally, sufficient concentrations of phosphorus in wastewater influent stream can induce spontaneous precipitation of Magnesium Ammonium Phosphate (abbreviation MAP, better known as struvite, together with the chemical name will be used interchangeably throughout this thesis). Such spontaneous formations create layers of struvite in pipes and other surfaces of WWTP which have to be cleared using sulphuric acid or broken down manually. Wastewater treatment plants have to be shutdown for maintenance every 6-12 months in order to prevent major damage caused to the equipment by struvite depositions. Avoiding this would increase the operational efficiency and cost-effectiveness of the plant [43, 128].

Today various different technologies have been developed all over the world. Over 30 different solutions for phosphorus recovery from sewage sludge have been re-

ported [31, 33]. Unfortunately, not every technological solution is economically viable or suitable for industrial commercialization, therefore currently these are rarely adapted by the WWTPs. This present study is focused on modelling a recovery method of phosphorus, however to cover all the background the following section is dedicated to summarising currently existing phosphorus removal methods and ideas.

2.2 Overview of phosphorus recovery and removal methods

Development of phosphorus removal technologies began in the 1950's. Since then, different technological approaches have been researched and developed. These technologies include direct phosphorus recovery from urine separation at the source, secondary effluent treatment at the wastewater treatment plant, recovery from sewage sludge ash, digester supernatant and sewage sludge [44]. Figure 2.1 presents access points at different stages of the wastewater treatment path. Phosphorus source access points marked on the diagram correspond to the following: (1) recovery through urine separation; (2) recovery from the secondary treated effluent; (3.1) recovery directly from sewage sludge; (3.2) recovery from digester supernatant; (4.1) recovery from untreated digested sewage sludge; (4.2) recovery from thickened and digested sludge; (4.3) recovery from dewatered and digested sludge; (5) recovery from incinerated sludge ash.

The interest of the current study was to investigate phosphorus recovery from an aqueous phase which would correspond to the access points (2) and (3) in Figure 2.1. Depending on the stage of the wastewater treatment, different technologies can be employed. Although there are various different attempts available in the industry, here only the most successful have been considered and these are summarised in Table 2.1. All of the aforementioned technologies are using one of three recovery methods or a combination of the following methodologies: ion-exchange (**REM-NUT®**), crystallisation (**AirPrex®**, **DHV Crystalactor®**, **P-RoC®**, **PRISA**)

Table 2.1: Major phosphorus recovery from aqueous phase technologies (other technologies are presented by Shokouhi [123]).

P recovery technologies from aqueous phase	Reference
Ostara Pearl Reactor®	[1]
P-RoC®	[15]
DHV Crystalactor®	[23]
AirPrex®	[57]
REM-NUT®	[77, 78]
PRISA	[93]

and precipitation (**REM-NUT®**, **AirPrec®**, **PRISA**).

The primary motivation of the study presented in this thesis was to investigate nutrient recovery from an aqueous phase through precipitation, where the potential reactor would be the Hydrodynamic Vortex Separator (HDVS) developed by Hydro International®. Due to the nature of the product, ion exchange processes would not be applicable therefore no further investigation in this area has been done. Crystallisation processes are known to produce products that need less further processing, however the time scales over which these processes occur are in the range of several days [44] and residence times in HDVS are much lower. On the other hand, although precipitation processes produce powdery amorphous material that requires further processing (e.g. dewatering, pelletising and drying), the time scales are much lower ($t < 1$h), which would be more applicable when considering HDVS, therefore this particular process has been considered as worthy of further investigation. Until now, HDVS products have been used as solid- liquid separators for primary wastewater treatment. Technologies that perform both precipitation and solid-liquid separation are not currently available therefore it represents a gap in the market and most importantly in the scientific knowledge as to whether system conditions observed in HDVS are sufficient for precipitation processes.

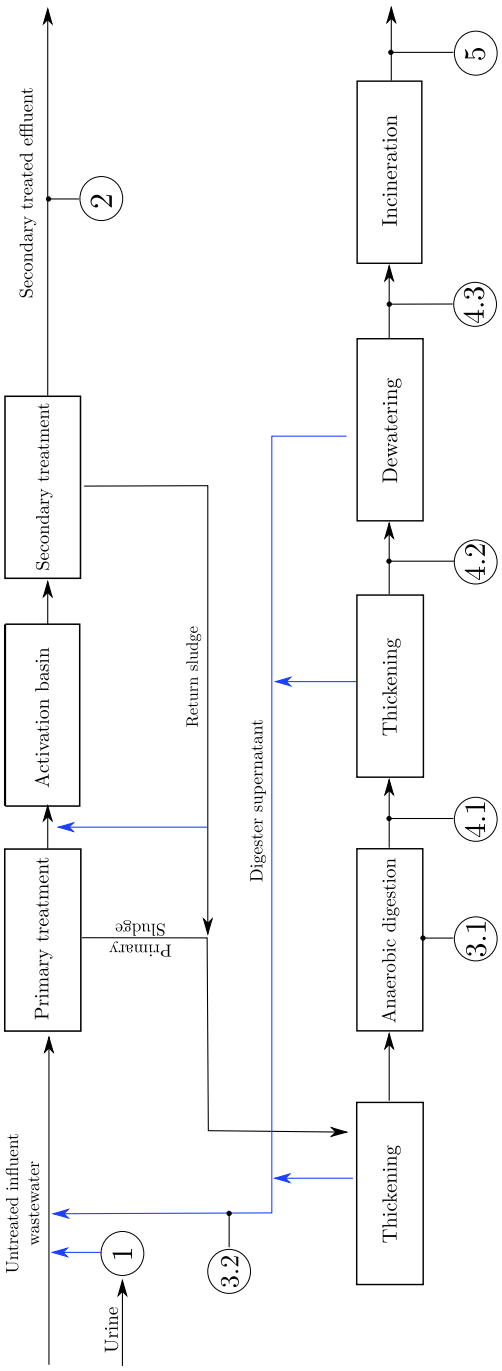

Figure 2.1: Phosphorus recovery access points over the course of wastewater treatment. (adapted from Egle et al. [44])

2.3 Operational conditions of struvite precipitation

Struvite formation has been studied by numerous authors using different experimental setups. The quality and the amount of precipitated struvite depends on specific conditions, and extensive research has been carried out to better understand which are the important parameters affecting MAP crystal formation. It has been found that factors such as the level of pH in the system, PO_4:Mg molar ratio and the type of reactors used efficiency all affect the product quality, as discussed below.

pH

The level of pH in the system is an important parameter that dictates the efficiency of struvite precipitation. Although struvite precipitation can occur between $pH = (7.0 - 11.5)$ Hao et al. [56] showed that the range of the most efficient production is $pH = (7.5 - 9.0)$. The level of acidity/alkalinity of the system affects the total solubility of the precipitated crystals and the rates at which the process occurs. It is known that during precipitation the level of pH tends to decrease, so Bouropoulos and Koutsoukos [19] have used it as an indicator to predict the state of nucleation or crystal birth stage. In processes where the ammonia stripping method was used, various authors investigated the effects of pH on the removal efficiency of $NH_4{}^+$ ions from the solution (Battistoni et al. [12], Celen and Türker [25], Ohlinger et al. [100]). Studies have concluded that the phosphorus and nitrogen removal efficiency is proportional to the level of pH in the system and it has been established that the level of solubility of struvite decreases with increasing alkalinity of the solution (Snoeyink and Jenkins [124]).

Recent studies by Xavier et al. [140] concluded that the most cost-effective conditions for struvite precipitation with nitrogen and phosphate are in stoichiometric ratio of $[PO_4^{3-}] : [NH_4^+] = 0.13$ are at the pH 10. Similarly Shalaby [122] showed that highest phosphorus recovery rates of 86% were observed when $pH = 10.89$

Reactant molar ratios

The molar ratio of the reactants althers the amount of reactive ions active in the solution and therefore the level of saturation of the solution. There is a consensus that the optimum molar ratios for struvite precipitation are Mg^{2+}:PO_4^{3-}:$NH_4{}^+$ = 1 : 1 : 1 (Doyle and Parsons [42]). Other authors have investigated how different molar ratios of all three reactants affect the level of nitrogen and Chemical Oxygen Demand (COD) removal rates [148]. It has been found that the removal rates nitrogen and COD were observed to be larger when the molar ratios between Mg^{2+} and PO_4^{3-} where 1.5 : 1 and 1 : 1.5 as opposed to the cases were the ratios were molar concentrations of some constituents were lower than 1. In the end it has been concluded that equimolar ratios are recommended and would be sufficient for efficient nitrogen and COD removal. Similar research by Zhang et al. [150] concluded that molar ratios of Mg^{2+}:$NH_4{}^+$:PO_4^{3-} = 1.15 : 1 : 1 are sufficient in order to avoid higher concentrations of phosphorus at the effluent stream and effectively remove nitrogen.

More recently a study by Shokouhi [123] showed how an increase in molar ratio between Mg^{2+} and PO_4^{3-} can significantly increase the amount of precipitated struvite. Interestingly, authors also observed that an increase in reaction time from 40min to 60min substantially decreased the amount of precipitated struvite, which indicates that depending on the system there exists an optimal residence time for struvite precipitation to occur.

Interestingly there have been reports on how the ratios of the reactant constituents affect the crystal sizes of the final products. Kozik et al. [72] have shown how within a 30 minute period the average size of MAP crystals have increased to $58\mu m$ at a ratio of Mg^{2+}:PO_4^{3-} = 1.2 : 1 as opposed to $42\mu m$ at a ratio of 1 : 1. A similar trend continued further where the sizes of the crystals were reported to be $80\mu m$ for 1.2 : 1 and $67\mu m$ for 1 : 1. Similar results have been reported by other authors as well (Hutnik et al. [62] [61], Martynia et al. [87]).

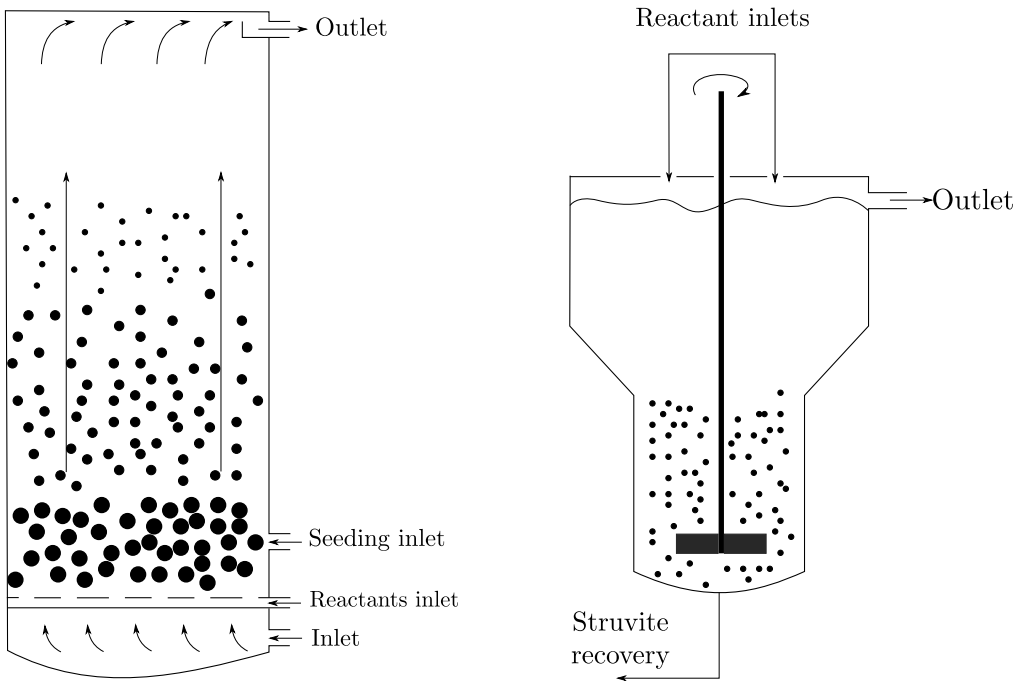

(a) Fluidised bed reactor

(b) Stirred reactor

Figure 2.2: Reactor types

Reactor type

The type of reactor dictates the type of products that can be obtained as well as the quality of products, and very different characteristics have been achieved using various setups. Two major types of the reactors that are currently being used throughout the industry are the fluidised bed reactors and the stirred tank reactors. The latter type of reactors can either be operated at a continuous flow regime where the fluid and solids are being taken out of the system continuously; or the batch reactor regime where the fluid and solids are kept in the system for extended periods of time in order to grow larger sized crystals. The schematic examples for both types of reactors are shown in Figures 2.2a, 2.2b.

Rahman et al. [114] have designed a continuous feed reactor with inflow rates of $0.73 Lmin^{-1}$. The produced crystals were irregular and white and up to 93% phosphorus and 31% nitrogen removal rates were observed. A different continuous flow design by Hutnik et al. [61] included a temperature control jacket and a paddled propeller draft tube. This design produced elongated shape crystals at varied

reactant molar ratios; however the authors reported that the total yield of the process was small and the cost efficiency of the product was low. Martynia et al. [87] successfully used jet-pump crystallisers at different scales and the process has been operated in a continuous regime.

Two pilot-scale studies conducted by Regy [117] and Pastor et al. [108] investigated struvite precipitation in mechanically stirred reactors. Both experimental studies showed how substantial levels of phosphorus removal can be achieved using stirred tank reactors (60% and 90% respectively). The authors also observed that struvite mean crystal sizes were reasonable - between 300μm to 425μm.

A fluidised bed reactor combined with an external clarifier and a storage tank for anaerobic digester supernatant has been used by Bhuiyan et al. [18]. The reactor precipitated larger crystals than observed by other studies, reaching sizes of $0.5mm - 3.5mm$. Ali and Schneider [4] used a batch reactor to predict struvite growth kinetics. The study aimed to investigate the kinetic relationships in a highly controlled scenario. The levels of pH and the reactor temperature were fixed and constantly monitored in order to accurately determine the precipitation kinetic rates. Authors also used the research to establish mathematical relationships between the dispersed phase particle size and the supersaturation of the solution.

A pilot scale reactor design by Le Corre [75] has been used in multiple studies by the authors to investigate the effects of foreign particles in the system and the order of the precipitation kinetics. The continuous feed reactor included two concentric stainless steel meshes purposefully fitted at the upper section of the reactor in order to precipitant scaling on the foreign surfaces. Using this reactor struvite precipitation rates observed were $7.6gm^{-2}h^{-1}$ and the removal rate of phosphates at optimal operational conditions was 81%. A three layered continuous flow reactor by Suzuki et al. [129] provided specific aeration and settling zones which produced $65.0kg$ of struvite over a period of 70 days which meant that the recovery rates of struvite was $171g$ per m^3 of wastewater. These results were achieved at influent loading rates of $5.3m^3day^{-1}$.

2.4 Kinetic mechanism studies

Struvite precipitation occurs as interplay of multiple different factors, all of which affect the performance of a specific reactor and the quality of the products. Thermodynamics, kinetics and hydrodynamics all affect the final outcome [113] and all of these areas have been investigated separately.

Most of the work up to date has been dedicated to understanding the thermodynamics of the process. Using different water-chemistry software packages various authors have tried to determine the equilibrium speciation of the solutions and from this the potential of crystal formation. A process model by Galbraith et al. [50] using the PHREEQC software package incorporated nucleation, growth and aggregation of struvite. This thermodynamically driven kinetics study incorporated mass conservation with population balance methodology. The authors parameter fitted empirical relationships for each of the kinetic mechanisms and showed how aggregation mechanism can participate in struvite formation which until now has been deemed to be negligible. They also incorporated an extension of the growth model that would take into account the potential affects of limited second order growth mechanism similar to the model given by Bekker et al. [14] in studies of aluminium oxide trihydrate. Miles and Ellis [92] used MINTEQA2 to duplicate experimental bench scale conditions. This study was able to replicate species concentrations, pH level and the molar ratios that match results obtained from the experiments. Çelen et al. [26] also performed a chemical equilibrium study of struvite in liquid swine manure wastewater. Comparison against experiments showed that the thermodynamic equilibrium model over-predicts the data, however only by a small margin as the model prediction for phosphorus removal was 99.5% whereas the experiments showed 98% removal rates. More recently Hanhoun et al. [55] used a combination of thermodynamic equilibrium modelling and the population balance method to show that struvite nucleation can possibly follow a classical nucleation mechanism derived from first principles rather than empirical power mechanism which is used more often by the researchers due to it's mathematical simplicity.

They also provided the growth rate kinetic parameter values that was based on the experiments.

Thermodynamic studies are an important part of research that help increase the understanding of the kinetic mechanisms behind the precipitation, however the characteristics of products cannot be explained solely by such studies. Fattah et al. [47] studied different operating conditions of an upflow crystalliser. It has been shown how the shape and the size of the struvite pellets depend on the upflow velocities. They also show how the crushing strength of the pellets was affected by the level of supersaturation in the system. Koralewska et al. [71] investigated draft-tube magma type crystallisers under two different operating conditions (DTM-upflow and DTM-downflow). It has been concluded that the the downflow configuration resulted in precipitated products that two times larger than then the ones observed in the the upflow configuration. Both studies showed the importance of hydrodynamics in precipitation processes which is not captured in pure chemical-equilibrium methodologies.

Even though the need to couple the precipitation thermodynamics, kinetics with hydrodynamics modelled using CFD can seem like an intuitive and therefore necessary part of the methodology, it has been neglected in a lot of research that has investigated struvite precipitation. The main reasons for that stems from significantly larger computational requirements and therefore has been deemed to be not viable. As discussed earlier one of the aims of the study was to investigate the potential of the hydrodynamic vortex separator to be used as a reaction vessel for the struvite precipitation. Hydrodynamics plays a key role on the operation of the HDVS, therefore excluding hydrodynamics from the modelling procedure would be misrepresentative of the system. Therefore it is crucial that in order to understand how the precipitation processes would occur in HDVS a model had to be formulated by imposing all three physical aspects: precipitation thermodynamics, kinetics and hydrodynamics.

2.5 CFD studies of precipitation

Coupling of hydrodynamics with precipitation thermodynamics and kinetics is not a trivial task due to the range of time and length scales that the modelling has to take into account. Microscale CFD models, usually referred to as Direct Numerical Simulations (DNS), resolve the systems at all length and time scales, but unfortunately the computational expense of such approaches is incredibly high and application of DNS for complicated engineering systems such as precipitation reactors is not viable. On the other hand, solely macroscale formulations do not capture the microscale effects on the particulate phase properties and therefore information about the system is lost. The current approaches found in the literature rely on coupling of a mesoscale methodology that provides an understanding of the property evolution of the dispersed phase (usually achieved through Population Balance Model (PBM)), with a macroscale model, e.g. two-fluid model [85].

Population balance equation introduces its own set of challenges and there have been different methodologies devised to obtain a solution. Two of the most popular solution methods - the Classes Method and the Method Of Moments both rely on different types of discretisation procedures of the size distribution function and more in depth discussion on these methods together with discussion on the alternatives will be given in Chapter 3. The basic principle behind the Classes Method relies on discretisation of a size distribution function in terms of a finite set of size classes. The Methods of Moments rely on the moment transform in order to reformulate the Crystal Size Distribution (CSD) in terms of its statistical moments which are then transported through space and time. Further, the density function is approximated as a finite polynomial of weighted kernel density functions. Figures 2.3a and 2.3b present representation of these approaches.

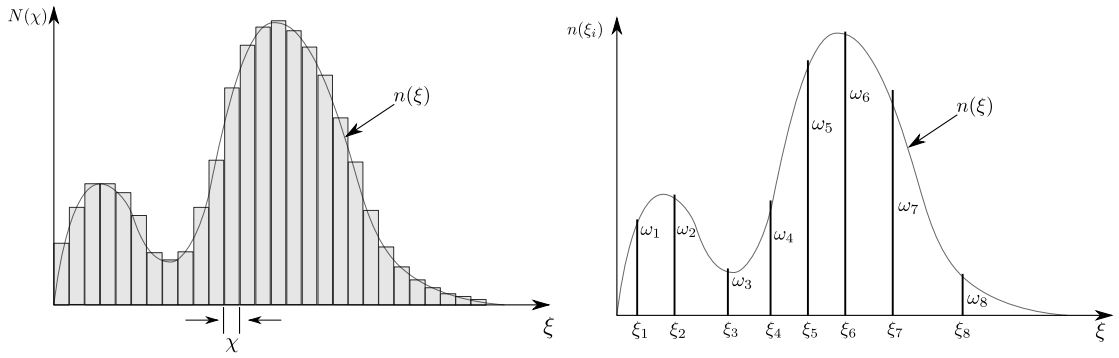

(a) Classes Method discretisation

(b) Method of Moments discretisation

Figure 2.3: Number density function discretisation approaches.

One approach to obtain a solution of the Population Balance Equation (PBE) coupled with CFD would be to compartmentalise the domain and limit the regions where population balance equation is being solved, therefore reducing the computational time; these are known as compartment models. A two compartment model implemented by Alexopoulos et al. [2] investigated turbulence inhomogeneities within a CFD framework in a cylindrical stirred reactor. Hydrodynamic simulation results dictated the construction of two compartments that were used to solve the PBE. Similarly, Bałdyga and Bourne [9] employed an assumption that the turbulent energy around the impeller is being dissipated, therefore the model can be reduced to a single compartment case. In work done by Alopaeus et al. [5], [6] the stirred tank reactor has been compartmentalised into eleven zones. The zones were based on the distribution of the turbulent energy dissipation rates that were calculated using a single-phase flow simulations and the results were vastly superior against the model used by Bałdyga and Bourne [9].

Another group of models have been focussed towards the studies of turbulence effects on the dispersed phase evolution at micro length scales. Bałdyga and Orciuch [11] studied the effects of micromixing on the precipitation of $BaSO_4$ in a coaxial pipe reactor using the formulation proposed in their previous publication [10]. They proposed using Reynolds Averaging of the moments transport equations which in turn takes into account the effects caused by the turbulent fluctuations.

The model however requires previous identification of the mixedness of the system which is not always available. The model was in good agreement with experimental data where in both cases the increase of Reynolds number resulted in a decrease in the mean crystal size. The authors also investigated the formulation where concentration fluctuations were neglected and it showed worse correlation against the experimental data. Alternative approaches are the Multi-Environment (ME) models; Öncül et al. [104] provide a comparison study of different methodologies that implement ME methods. The micromixing models are formulated using two probability density functions: one representing the local mixture fraction values of the reactants, the other used to indicate different environments (or modes) in each computational element. They found that micromixing models have significant influence at high supersaturation levels and lower Re values, whereas at higher Reynolds numbers and lower saturations these effects would be negligible or even in some cases show poorer correlation against experimental data, therefore in some cases the micromixing effects can be neglected.

Another popular approach is a group of models often classified as Discrete Population Balance Methods (DPBM) or Class Methods (CM), based on discretisation of the population balance equation in terms of discrete size bins which are then transported individually. Graphical representation of Class Method discretisation is shown in Figure 2.3a. Becker [13] has used this approach to study oil emulsification in water in a static mixer SMX+ geometry. As in previous cases this work relied on a single phase flow model to model the hydrodynamics of the flow, which was then coupled to the PBE using a multi-scale class method. Even though the work was focussed on bubble dynamics the results prove that the procedure can be applied to complex three dimensional cases. Cheng et al. [29] modelled barium sulphate precipitation in a stirred tank reactor using the multi-class method. The numerical results showed good agreement with published data, however the authors pointed out that the class method was found to be very computationally intensive.

A class of solution methods often very well regarded due to its computational efficiency relative to the alternatives is the Method Of Moments (MOM). These

models rely on the transformation of the number density function in terms of a finite set of its statistical moments. Figure 2.3b shows a graphical representation of the discretisation method. Öncül et al. [103] applied standard method of moments to study $BaSO_4$ precipitation in a stirred tank reactor. The simulations were found to be very stiff, therefore small time-steps were necessary in order to advance the solution and some of the results showed considerable discrepancies against numerical results by Wei and Garside [136]. The quadrature method of moments first formulated by McGraw [89] has recently been used for struvite nucleation and growth in a fluidised bed reactor and was coupled with the algebraic slip mixture model (ASMM) used to model the two-phase flow hydrodynamics (Ye et al. [146]). The authors investigated different inlet configurations of the reactor and found that the supersaturation levels in the system, solid concentrations and CSDs were highly dependent on different operational conditions of the reactor. To address some issues related to the QMOM formulation Marchisio and Fox [82] proposed an extension to it known as the Direct Quadrature Method Of Moments (DQMOM). Selma et al. [121] has studied bubbly flow dynamics using this approach and the results validated well against the experimental data. The main problem associated with the QMOM and DQMOM formulations is that in certain cases the set of transported moments does not represent physical crystal size distribution. The most recent attempt to address these issues have been by Madadi-Kandjani and Passalacqua [80] in the Extended Quadrature Method Of Moments (EQMOM). The formulation has been implemented by Passalacqua et al. [107] and it has been validated for aggregation, breakup and size-independent cases; however application of this model in a precipitation system has not been attempted as of this date. It has therefore been decided that EQMOM formulation due to its recent development will be suitable to model struvite precipitation processes.

Chapter 3

Mathematical model

Systems that involve struvite precipitation involve a wide array of complex physics all of which has to be modelled appropriately. Multiphase flows, equilibrium thermodynamics, reaction kinetics and solid phase evolution modelling are all important aspects in systems of struvite precipitation.

There are different formulations when it comes to modelling multiphase flows. Some are more efficient but less accurate due to certain assumptions being made, some are less efficient, however these would capture more intricate aspects of the physics. In this chapter lagrangian, eulerian and the mixture model formulation are presented and discussed. For this study it has been decided to use the drift flux model which is a specific formulation of the mixture model and the particular implementation has been tailored and validated in the wastewater systems, hence the choice for it to be used for this particular problem.

Precipitation reactions are controlled by the equilibrium thermodynamics. There are quite a few aspects that affect the accuracy of the model, such as the appropriate ways to evaluate the supersaturation level in the system and the ionic speciation calculations that allows us to calculate the concentrations of the reactive ions in the solution. Both of these key points are presented and discussed in this chapter.

Finally,the modelling of the change of the dispersed phase properties is presented.

This is achieved using the population balance approach. Because solution of the population balance equation is not a trivial problem the different approaches for the solution methods are presented and their benefits and drawbacks are shown. The extended quadrature method of moments has been chosen as a methodology to solve the population balance equation, therefore at the end of this chapter the final equations are presented.

3.1 General conservation equations

The governing equations of motion describing flows of fluids have been postulated by Claude-Louis Navier and George Gabriel Stokes. The Navier-Stokes equations describe mass and momentum continuity in an Eulerian frame of reference and for variable density flows:

$$\frac{\partial \rho}{\partial t} + \nabla \cdot (\rho \mathbf{U}) = 0, \tag{3.1}$$

$$\frac{\partial \rho \mathbf{U}}{\partial t} + \nabla \cdot (\rho \mathbf{U}\mathbf{U}) = \nabla \cdot \sigma + \mathbf{F} \tag{3.2}$$

where ρ is the density of the fluid, $\mathbf{U}$ is the velocity of the fluid, t is time, $\nabla\cdot$ is spatial divergence operator, σ is the fluid stress tensor and $\mathbf{F}$ are all of the external forces acting on the fluid.

The generalised form of the stress tensor for Newton's law is defined as:

$$\sigma = -\Big(p + \frac{2}{3}\mu \nabla \cdot \mathbf{U}\Big)\mathbf{I} + \mu[\nabla \mathbf{U} + (\nabla \mathbf{U})^T] \tag{3.3}$$

Combining Equations 3.1, 3.2, 3.3 produces a set of partial differential equations of mass and momentum conservation for Newtonian fluids:

$$\frac{\partial \rho}{\partial t} + \nabla \cdot (\rho \mathbf{U}) = 0 \tag{3.4}$$

$$\frac{\partial \rho \mathbf{U}}{\partial t} + \nabla \cdot (\rho \mathbf{U}\mathbf{U}) = \rho \mathbf{g} - \nabla\Big(P + \frac{2}{3}\mu \nabla \cdot \mathbf{U}\Big) + \mu[\nabla \mathbf{U} + (\nabla \mathbf{U})^T] \tag{3.5}$$

These Equations can be further simplified for incompressible fluids, i.e. $\rho = \text{const}$. Using ν for kinematic viscosity and p for kinematic pressure the equations are as follows:

$$\nabla \cdot (\rho \mathbf{U}) = 0 \tag{3.6}$$

$$\frac{\partial \mathbf{U}}{\partial t} + \nabla \cdot (\mathbf{U}\mathbf{U}) = \mathbf{g} - \nabla p + \nabla \cdot (\nu \nabla \mathbf{U}) \tag{3.7}$$

3.2 Mathematical formulation of two-phase flow

Multi-phase flows can be classified as flows that involve different substances that have different immiscible physical states. Constituent components are categorized by the phase specific properties and by the topology of the interface between the different phases (Ishii and Hibiki [63]). The difficulty in modelling arises due to the vast array of classifications of multi-phase flow possible. For two-phase flows the possible system classification can be gas-liquid, gas-solid, liquid-solid and liquid-liquid. From a topological perspective the flows can be classified as dispersed, separated or mixed.

As can already be seen, the range of physics that multi/two-phase flows include is overwhelming and there has to be a lot of consideration and care taken in order to model the system appropriately. Therefore in this section we present two different mathematical descriptions of two-phase flows: lagrangian and eulerian approaches.

3.2.1 Lagrangian approach

The Lagrangian approach treats the dispersed phase of the system as a statistically significant set of point particles that are tracked throughout the domain and the trajectories are used to extract the information about the properties of the flow. The Lagrangian mechanics equations of motion are formulated in such a way that the reference frame follows the trajectory of the particle and a distinctive equation of motion (EOM) is prescribed to each point particle. This results in the following general equation:

$$\rho_d \frac{\mathrm{d}\mathbf{u}_d}{\mathrm{d}t} = \sum \mathbf{F} \tag{3.8}$$

where $\mathbf{u}_d$ is the velocity of the particle, ρ_d is the dispersed phase density and $\mathbf{F}$ are all of the forces acting on the particle. Treatment of the forces term in the equation above is an ongoing research subject, and Elghobashi [45], Brennen [22] provide reviews for it.

Two-phase flow analysis using a Lagrangian approach requires a statistically significant number of particles to be followed throughout the flow domain. Relevant information on the averaged nature of the flow can be obtained from the trajectories of the particles.

The Lagrangian formulation requires a large set of equations of motion to be solved in order to extract statistically reliable information. For example, the settling tanks studied by Brennan [21] would require more than 10^6 particles per ml in order to resolve the dispersed phase flow field reliably. The current study is investigating similar types of systems, hence this approach is not viable. Instead, the continuous phase in the two-phase system is treated using the Eulerian framework and the formulation of such framework is described in Section 3.2.2.

Even though the Lagrangian approach is not used for this study, it has been successfully used in different research areas, eg. bubble dispersion and spray combustion [20, 141]. Other researchers have also discussed methodologies that could be used to make an optimal choice for a number of particles used in a Lagrangian simulation, see Graham and Moyeed [54].

3.2.2 Eulerian approach

The Eulerian formulation treats both dispersed phase and fluid/gas phase as a continuous medium. Rather than describing the fluid as a set of discrete particles as discussed in the previous section, in the Eulerian formulation specific locations of the fluid are tracked through the passage of time. Therefore the flow variables are represented by functions of space and time, eg. velocity of the fluid $\mathbf{U}(\mathbf{x}, t)$ [96]. The most common approach for two-phase system modelling is usually referred to as the *Two-fluid model* (TFM) (Ishii and Hibiki [63]) in which it is assumed that both fluid phases are coexisting at the same points in space inter-penetrating each other.

Conservation equations for the two-fluid model are derived from the general conservation equations of mass, momentum and (depending on the physics of the system) energy. The two-fluid conservation equations are obtained through the use of appropriate averaging methods applied to the whole physical system.

Section 3.2.2.2 presents the formulation of this model based on the work by Weller [137] and Hill [58]. The conditional averaging procedure used to derive the equations is described in Section 3.2.2.1.

Hill [58] comments that two-fluid models are applicable in the entire flow regimes of multi-phase flows. However, the drawbacks of such generality are that in order for the model to be applicable to a specific flow regime investigated it requires careful consideration of the inter-phase models. In cases when the flows do not occur in well defined regimes or if there are transitions between the flow regimes closure models are difficult to formulate, because the physical mechanisms governing the phenomena are not well understood.

Depending on the problem of interest, simplifications of the two-fluid model are possible, eg. Algebraic Slip Mixture Model (ASMM) and Drift-Flux Model (DFM) [65]. The main principle behind these models is the reformulation of the key parameters from the two-fluid model as phase fraction weighted sums, where new

parameters are referred to as mixture parameters. Both ASMM and DFM formulations are presented in this section and even though there can be alternative formulations, these two models have been used in the literature and both showed promising results.

3.2.2.1 Averaging

Conservation equations can be averaged using volume, time or ensemble averaging [58]. A general scalar quantity ϕ can be averaged as follows:

$$\overline{\phi} = \frac{1}{V}\int_V \phi \, \mathrm{d}V \tag{3.9}$$

$$\overline{\phi} = \frac{1}{T}\int_T \phi \, \mathrm{d}T \tag{3.10}$$

$$\overline{\phi} = \lim_{N\to\infty} \frac{1}{N}\sum_{r=0}^{N} \phi_r \tag{3.11}$$

where V and T are the averaging domains for volume and time respectively; N is the number of realisations in the ensemble, with ϕ_r being a particular realisation of the scalar parameter. It is widely recognised that ensemble averaging is more fundamental than the other two counterparts. In contrast to volume or time averaging, ensemble averaged equations are valid throughout the infinitesimal time and space domains, whereas time and volume averaging impose restrictions on the time and length scale validity of the equations.

Hill [58] and Weller [137] have developed an equation conditioning procedure that ensures that phase contributions to the averaged equations would come only from the regions that contain that phase. The equations are first multiplied by an indicator function ψ_n:

$$\psi_n(\mathbf{x}, t) = \begin{cases} 1 & \text{if phase } \alpha \text{ is present;} \\ 0 & \text{Anywhere else.} \end{cases} \tag{3.12}$$

The indicator function mathematically is defined as the Heaviside function of some imaginary scalar phase function $\psi_n = \mathbf{H}\{f(\mathbf{x}, t)\}$. This definition allows one to

perform differential operations on the indicator function shown bellow, see Hill [58] for details.

$$\nabla\psi_n = \delta(f_\alpha)\mathbf{n}_\alpha \tag{3.13}$$

$$\frac{\partial\psi_n}{\partial t} = -\mathbf{v}_i \cdot \nabla\psi_n \tag{3.14}$$

Hill [58] also introduces a weighting function defined as follows:

$$\overline{\phi} = \frac{\overline{\psi_n \Phi}}{\alpha_n} \tag{3.15}$$

where α_n is defined as the phase fraction ϕ is the quantity under consideration, eg. $U(\mathbf{x}, t)$, $\rho(\mathbf{x}, t)$.

Conditioned local conservation equations are then ensemble averaged to give the two-fluid conservation equations. The procedure is illustrated in the following couple of sections.

3.2.2.2 Two Fluids Model

Conservation of Mass

Recall the equation for local mass conservation (Equation 3.1):

$$\frac{\partial\rho}{\partial t} + \nabla \cdot (\rho\mathbf{U}) = 0$$

First assuming that the flow is incompressible and no phase change is present in the system, one can then apply conditional averaging followed by ensemble averaging (denoted by an overbared quantities) procedures to obtain the following expression:

$$\overline{\psi_n \frac{\partial\rho}{\partial t}} + \overline{\psi_n \nabla \cdot (\rho\mathbf{U})} = 0 \tag{3.16}$$

where subscripts denote phase. The equation can now be rearranged and by making use of equations [3.13, 3.14, 3.15] the phase continuity equation is derived to be:

$$\frac{\partial\alpha_n\rho_n}{\partial t} + \nabla \cdot (\alpha_n\rho_n\mathbf{U}) = 0 \tag{3.17}$$

Note that an overbar symbol has been omitted for clarity.

Conservation of Momentum

Similarly to Equation 3.17, phase momentum conservation equation can be derived:

$$\frac{\partial \alpha_n \rho_n \mathbf{U}_n}{\partial t} + \nabla \cdot (\alpha_n \rho_n \mathbf{U}_n \mathbf{U}_n) = -\alpha_n \nabla p + \nabla \cdot (\alpha_n \mathbf{R}_n^{\text{eff}}) + \alpha_n \rho_n \mathbf{g} + \mathbf{M} \tag{3.18}$$

where $\mathbf{R}_n^{\text{eff}}$ is a term combining Reynolds (turbulent) and viscous stresses and $\mathbf{M}$ is the averaged inter-phase momentum transfer term. Both the stress term and the momentum exchange term requires modelling to achieve closure, see Hill [58], Riella et al. [118], Rusche [119] for details.

3.2.2.3 Mixture models

The most common simplifications of the two-fluid model are referred to as mixture models. The main idea behind these models is to combine the existing phase conservation equations and then to reformulate in terms of mixture parameters. This reduces the number of equations of motion that require solution which is computationally more efficient. However, the generality loss of the two-fluid formulation has to be compensated for by employing empirical formulations for the relative velocity term that arises during the derivation.

There are different formulations available, for example the diffusion mixture model, algebraic slip model, drift flux model and classical homogeneous mixture model [65]. In this section, descriptions of the algebraic slip model and the drift flux model are provided. In this study the decision has been made to use the drift flux model, due to its previous application in the wastewater settling studies done by Brennan [21], however since the start of this research project there has been reports in the literature of the algebraic slip model being used for struvite precipitation which have showed some promising results [144].

Mixture properties

For the two phase system an additional continuity restriction has to be defined and imposed:

$$\alpha_1 + \alpha_2 = 1 \tag{3.19}$$

Mixture density and mixture pressure can be defined as a phase fraction weighted sum of the respective phase properties. as follows:

$$\rho_m = \alpha_1\rho_1 + \alpha_2\rho_2 \tag{3.20}$$

$$P_m = \alpha_1 p_1 + \alpha_2 p_2 \tag{3.21}$$

Finally, the center of mass mixture velocity is defined as:

$$U_m = \frac{\alpha_1\rho_1 U_1 + \alpha_2\rho_2 U_2}{\rho_m} \tag{3.22}$$

Algebraic slip mixture model

One available formulation of the mixture model is the Algebraic Slip Mixture Model (ASMM). Similarly as in the two-fluid model it is first of all assumed that the different phases can be treated as two interpenetrating continua where both phases are allowed to move at different velocities. The ASMM also relies on the assumption that over short spatial length scales a local inter-phase equilibrium is established.

The benefit of the ASMM formulation is that it does not require solution of momentum and mass for each phase separately, therefore reducing the total number of equations that need to be solved. A comparison between TFM and ASMM models in bubble columns has been reported by Chen et al. [28] and both formulations produced comparable results.

The mixture momentum conservation in ASMM is expressed in equation 3.23.

$$\frac{\partial\rho_m\mathbf{U}_m}{\partial t} + \nabla\cdot(\rho_m\mathbf{U}_m\mathbf{U}_m) = -\nabla P_m + \nabla\cdot(\tau_m + \tau_m^t + \tau_m^d) + \rho_m\mathbf{g} + \mathbf{M}_m \tag{3.23}$$

$$\frac{\partial\alpha_d\rho_d}{\partial t} + \nabla\cdot(\alpha_j\rho_j\mathbf{U}_m + \alpha_j\rho_j\mathbf{U}_{dr,s}) = 0 \tag{3.24}$$

where τ_m, τ_m^t, τ_m^d are the mixture viscosity, mixture turbulence and the diffusion stresses which are defined as follows:

$$\tau_m = \sum_{j=1}^{n}\alpha_j\tau_j \tag{3.25}$$

$$\tau_m^t = -\sum_{j=1}^{n}\alpha_j\overline{\rho_{lk}\mathbf{U}_j'\mathbf{U}_j'} \tag{3.26}$$

$$\tau_m^d = -\alpha_j\rho_k\mathbf{U}_{dr,s}\mathbf{U}_{dr,s} \tag{3.27}$$

Where the last two terms in Equation 3.27 represent the relative velocity of the solid phase with respect to the mixture mass center. These terms are usually referred to as drift velocity and are defined below.

$$\mathbf{U}_{dr,s} = \mathbf{U}_s - \mathbf{U}_m \tag{3.28}$$

where $\mathbf{U}_s$ is the velocity of the dispersed phase. In addition the slip velocity between the two phases is defined in Equation 3.29.

$$\mathbf{U}_{sl} = \mathbf{U}_s - \mathbf{U}_l \tag{3.29}$$

where the subscripts $\mathbf{U}_s$ and $\mathbf{U}_l$ stand for solid and liquid phase velocities respectively. Combining expressions 3.28, 3.29, 3.22, the final expression for drift velocity can be obtained:

$$\mathbf{U}_{dr,s} = \mathbf{U}_{sl} - \frac{\alpha_s \rho_s}{\rho_m}\mathbf{U}_{sl} \tag{3.30}$$

An appropriate closure has to be chosen for the slip velocity, for example Yan et al. [142] provides the following closure for turbulent flows:

$$\mathbf{U}_{sl} = \frac{(\rho_s - \rho_m)d_s^2}{18\mu_t f_{\text{drag}}}\left(\mathbf{g} - \frac{\partial \mathbf{U}_m}{\partial t}\right) - \frac{\mu_m}{\alpha_s \sigma_D}\nabla\alpha_l \tag{3.31}$$

where σ_D is the Prandtl dispersion coefficient, μ_t is the turbulent viscosity and d_s is the diameter of the dispersed phase. The drag function f_{drag} is defined below.

$$f_{\text{drag}} = \frac{K_{sl} d_s^2}{18\alpha_s \mu_l} \tag{3.32}$$

with K_{sl} being the interphase exchange coefficient.

Drift-Flux Model

The derivation procedure behind the drift flux model follows similar principles as in the case of the algebraic slip model. Both the ASMM and DFM are derived from the time-averaged two-fluid model equations, however the drift flux model is expressed in terms of mass and phase weighted variables.

In the DFM the drift velocity of the jth phase is defined relative to the mixture velocity:

$$\mathbf{U}_{dr,j} = \langle \mathbf{U}_j \rangle^{\alpha_j \rho_j} - \sum_j \alpha_j \langle \mathbf{U}_j \rangle^{\alpha_j \rho_j} = \langle \mathbf{U}_j \rangle^{\alpha_j \rho_j} - \mathbf{j}_m \tag{3.33}$$

where $\mathbf{j}_m$ is the volumetric flux of the mixture. The dispersed phase flux can be defined as in below:

$$\mathbf{J}_{dr,s} = \alpha_s (\langle \mathbf{U}_s \rangle^{\alpha_s \rho_s} - \mathbf{j}_m) = \alpha_s \mathbf{U}_{dr,s} \tag{3.34}$$

Using the drift and mixture relationships the conservation equations for momentum and the continuity equations for mass and dispersed phase can be rewritten in the final form (note that averaging symbols previously indicated by $\langle\rangle$ have been removed for simplicity):

$$\frac{\partial \rho_m}{\partial t} + \nabla \cdot (\rho_m \mathbf{U}_m) = 0, \tag{3.35}$$

$$\frac{\partial \alpha_s}{\partial t} + \nabla \cdot (\alpha_s \mathbf{U}_m) = -\nabla \cdot \left(\frac{\alpha_s \rho_l}{\rho_m} \mathbf{U}_{dr,s} \right) + \nabla \cdot \Gamma \nabla \alpha_s, \tag{3.36}$$

$$\begin{aligned} \frac{\partial \rho_m \mathbf{U}_m}{\partial t} + \nabla \cdot (\rho_m \mathbf{U}_m \mathbf{U}_m) = & -\nabla P_m \\ & + \nabla \cdot [\tau + \tau^t] \\ & - \nabla \cdot \left(\frac{\alpha_s}{1 - \alpha_s} \frac{\rho_l \rho_s}{\rho_m} \mathbf{U}_{dr,s} \mathbf{U}_{dr,s} \right) \\ & + \rho_m \mathbf{g} + M_m \end{aligned} \tag{3.37}$$

where subscripts m, l, s stand for mixture, liquid and solid respectively. Relative velocity or settling velocity $\mathbf{U}_{dr,s}$ has to be modelled using empirical relationships. Takács et al. [130] provide two empirical expressions for the settling velocity (NB terms settling and drift are used interchangeably throughout this thesis). The first empirical model referred to as the *Simple model* is defined in eq. 3.38:

$$U_{dr,s} = U_0 \mathrm{e}^{(-kC)} \tag{3.38}$$

where U_0 is the terminal settling velocity, k is the empirical coefficient ($k \approx 5 \cdot 10^{-4}$) and C represents solids concentration in mg/l. Concentration is usually expressed in terms of solids volume fraction and solids density: $C = 1000 \alpha_d \rho_d$. The *Simple*

model assumes that all particles in the dispersed phase are uniform in size; this is of course a rough assumption. To work around these limitations Takács et al. [130] studied suspended solids and identified 3 different regimes:

$$C \in (500; \infty] \text{ mg/l} \qquad \text{Slowly settlable solids} \tag{3.39}$$

$$C \in [100; 500] \text{ mg/l} \qquad \text{Highly settlable solids} \tag{3.40}$$

$$C \in [1; 10] \text{ mg/l} \qquad \text{Non-settlable solids} \tag{3.41}$$

Using this classification a modified model (referred to as the *General model*) is devised:

$$U_{dr,s} = U_0 \left[\mathrm{e}^{(k(C - C_{\min}))} - \mathrm{e}^{-k_1 (C - C_{\min})} \right] \tag{3.42}$$

where k_1 is the settling exponent for poorly-settling particles (generally $k_1 \approx 0.015$) and $C_{\min}$ is the upper concentration limit for the non-settlable flocs.

Terminal velocity of spherical particles

The drift flux model formulation relies on the assumption that the terminal settling velocity of the dispersed phase is fixed due to the fact that the internal qualities of the dispersed phase are not changing with time. This is however not the case, when formation of the dispersed phase due to the chemical processes is being considered. Therefore an extension of the settling velocity models has been proposed here, where the terminal velocity would change with respect to the change of the internal properties of the dispersed phase, specifically the mean diameter of the solid phase. It is well known that the terminal velocity of the spherical particles in the Stokes Flow regime can be described as shown in Equation 3.43 [21, 34]:

$$U_0 = \frac{\mathbf{g} d^2}{18 \mu} (\rho_s - \rho_l) \tag{3.43}$$

where $\mathbf{g}$ is the gravitational constant vector, μ is the dynamic viscosity of the continuous phase, ρ_s and ρ_l are the densities of the dispersed and continuous phases respectively and d is the diameter of the particle.

As will be described in the later sections, the inception and the evolution of the solid phase is controlled by the precipitation kinetics, the properties of the solid

phase change with respect to time and space and are modelled using the population balance approach. An important parameter that can be extracted from the moments equations described in Section 3.4 is the Sauter Mean Diameter d_{43} [13]:

$$d_{43} = \frac{\mu_4}{\mu_3}, \tag{3.44}$$

where μ_3 and μ_4 are the third and the fourth moments of the crystal size distribution (see Section 3.4 for full description).

In order to account for the variation of the terminal velocity of the dispersed phase at different locations of the system being modelled two new settling models are proposed. Depending on whether the model is a derivation of the Equation 3.38 or Equation 3.42 these are named as *Simple-varying* settling velocity model or *General-varying* settling velocity model. Both formulations are defined as follows:

***Simple-Varying* settling velocity model**

$$U_{dr,s} = \frac{\mathbf{g} d_{43}^2}{18\mu}(\rho_s - \rho_l)\mathrm{e}^{(-kC)} \tag{3.45}$$

***General-Varying* settling velocity model**

$$U_{dr,s} = \frac{\mathbf{g} d_{43}^2}{18\mu}(\rho_s - \rho_l)\left[\mathrm{e}^{(k(C-C_{\min}))} - \mathrm{e}^{-k_1(C-C_{\min})}\right] \tag{3.46}$$

Numerous authors have examined the crystal morphology of struvite [3, 55, 75, 126] and depending on the experimental conditions, struvite crystals have been reported to form needle type, rectangular platelet, star type, prismatic type, pyramidal type and dendritic type shapes [112]. Due to variety in the morphology of struvite crystals it has been assumed that the particles are spherical therefore equations 3.45, 3.46 are only valid for spherical particles.

This particular drift flux model implementation has been used in modelling of sludge settling in wastewater systems and showed good correlation against the experimental data [21]. It does however make strong assumptions with respect to the settling properties of the dispersed phase, which is not the case for the ASMM, however because of the solver performance against the experimental data in sludge

settling systems it is still regarded as a valid formulation to use when considering systems where precipitation mechanisms are involved.

3.3 Reaction Modelling

Fluid dynamics of the reactant species are modelled by solving the convection diffusion equation of the passive scalar Y_i, where the transported scalar represents the mass fraction of some chemical species involved in the reaction. Mass fractions are dimensionless variables and they carry one important property: a total sum of all mass fractions must add to unity, i.e. $\sum_i Y_i = 1$.

Struvite precipitation reaction chemistry is governed by equilibrium thermodynamics, which is covered in the second part of this section. This key aspect determines the amount of reactant chemical species in the solution as well as the speed of the reaction. The struvite precipitation reaction shown below involves three ionic reactant species which are formed in a solution of water. There are however other elements that form, therefore a methodology has to be established to calculate the amount of participating ions.

$$\mathrm{Mg^{2+}} + \mathrm{NH_4^+} + \mathrm{PO_4^{3-}} + 6\,\mathrm{H_2O} \longrightarrow \mathrm{MgNH_4PO_4 \cdot 6\,H_2O}$$

Depending on the amount of reacting ions available in the solution, the level of saturation can be determined which is done by using specific indicator functions. Section 3.3.2 will cover how supersaturation dictates the state of the reaction process and how it can be used as a control parameter that would help to obtain better quality products.

3.3.1 Species transport

Chemical species transport is modelled by solving a convection/diffusion equation. For the ith species the transport equations is as follows:

$$\frac{\partial(\rho Y_i)}{\partial t} + \nabla(\rho \mathbf{U} Y_i) + \nabla \cdot (\mathbf{J}_i) = R_i \tag{3.47}$$

where Y_i represents the mass fraction of the ith species; $\mathbf{J}_i$ is the diffusion flux for the ith species and the R_i terms are the source/sink term for the ith species due to the chemical reaction that is taking place. In this work the scalar transport equation is used to model the transport of the reactant ions (i.e. Mg^{2+}, NH_4^+, PO_4^{3-}) and the product (i.e. $MgNH_4PO_4 \cdot 6\,H_2O$).

Depending on the system analysed the diffusion flux term is manifested due to the gradients in concentration and temperature fields and is defined as follows [118]:

$$\mathbf{J}_i = \frac{\mu_t}{Sc_t}\nabla Y_i + D_{T,i}\frac{\nabla T}{T} \tag{3.48}$$

where μ_t is the turbulent viscosity, Sc_t is the turbulent Schmidt number (usually in the range of $Sc_t \in [0.5; 1.2]$) and $D_{T,i}$ is the thermal diffusivity coefficient. However, in this study temperature gradients were not of major concern hence the second term is omitted:

$$\mathbf{J}_i = \frac{\mu_t}{Sc_t}\nabla Y_i \tag{3.49}$$

Source/Sink terms R_i are proportional to the rate of change of the third moment M_3 of the number density function (see Section 3.4 for a description). The expression for the source/sink terms can be written as follows:

$$R_i = \pm\phi_v\rho_d\left(\frac{W_i}{W_d}\right)G\frac{\partial\mu_3}{\partial t} \tag{3.50}$$

where ϕ_v is a shape factor constant of the products; ρ_d is the density of the product species; W_i and W_d are the molecular weights of the species i and the product species. The last term in the sources is the rate of change of the third moment of the Number Density Function (NDF) and it is related to the growth rate, the supersaturation levels and the second moment of the NDF:

$$\frac{\partial\mu_3}{\partial t} = 2C_g f(C)\mu_2 \tag{3.51}$$

where C_g is the growth rate constant; $f(C)$ is a function indicating the level of supersaturation in the system.

In the following sections species thermodynamics and the precipitation kinetics modelling will be described.

3.3.2 Thermodynamic modelling

Solution chemistry plays a key role in modelling crystal formation through precipitation. Recall that struvite precipitation reaction occurs between free ions in the solution Mg^{2+}, $NH_4{}^+$, $PO_4{}^{3-}$ and can be written as in Equation 3.52.

$$Mg^{2+} + NH_4{}^+ + PO_4{}^{3-} + 6\,H_2O \longrightarrow MgNH_4PO_4 \cdot 6\,H_2O \tag{3.52}$$

However, other compounds can be formed which would reduce the availability of ions to participate in MAP formation. Solution containing magnesium, ammonium and phosphate molecules form the following complexes: Mg^{2+}, $MgOH^-$, $MgH_2PO_4^+$, $MgHPO_{4(aq)}$, $MgPO_4^-$, $H_3PO_{4(aq)}$, $H_2PO_4^-$, HPO_4^{2-}, PO_4^{3-}, $NH_{3(aq)}$, NH_4^+ (Ohlinger et al. [101], Rahaman et al. [113], Ye et al. [144]).

Thermodynamic equilibrium is characterised by equilibrium constants (depending on literature used these are often referred to as solubility products, therefore this term will be used interchangeably throughout the thesis). For example, the process of two constituents A and B and their product AB would have a process defined by the equation:

$$AB^+ \overset{K_{AB^+}}{\longleftrightarrow} A^{2+} + B^-$$

For such process the equilibrium constant would be defined as:

$$K_{AB} = \frac{\{A^{2+}\}\{B^-\}}{\{AB^+\}}$$

where curly brackets represent ionic activity and is related to the molar concentration of ion as:

$$\{A^+\} = \gamma_{A^+}[A^+] \tag{3.53}$$

Equations of formation for all of the compounds forming in the solution and their respective equilibrium constants are presented in Equations 3.54 to 3.63.

$$MgOH^+ \quad \overset{K_{MgOH^+}}{\longleftrightarrow} \quad Mg^{2+} + OH^-; \qquad K_{MgOH^+} \quad = \quad \frac{\{Mg^{2+}\}\{OH^-\}}{\{MgOH^+\}} \tag{3.54}$$

$$\mathrm{MgHPO_{4(aq)}} \xleftrightarrow{\mathrm{K_{MgHPO_4}}} \mathrm{Mg^{2+} + HPO_4{}^{2-}};\ \mathrm{K_{MgHPO_4}} = \frac{\{\mathrm{Mg^{2+}}\}\{\mathrm{HPO_4{}^{2-}}\}}{[\mathrm{MgHPO_{4(aq)}}]} \tag{3.55}$$

$$\mathrm{MgH_2PO_4{}^{+}} \xleftrightarrow{\mathrm{K_{MgH_2PO_4^-}}} \mathrm{Mg^{2+} + H_2PO_4{}^{-}};\ \mathrm{K_{MgH_2PO_4^+}} = \frac{\{\mathrm{Mg^{2+}}\}\{\mathrm{H_2PO_4{}^{-}}\}}{\{\mathrm{MgH_2PO_4{}^{+}}\}} \tag{3.56}$$

$$\mathrm{MgPO_4{}^{-}} \xleftrightarrow{\mathrm{K_{MgPO_4^-}}} \mathrm{Mg^{2+} + PO_4{}^{3-}};\quad \mathrm{K_{MgPO_4^-}} = \frac{\{\mathrm{Mg^{2+}}\}\{\mathrm{PO_4{}^{3-}}\}}{\{\mathrm{MgPO_4{}^{-}}\}} \tag{3.57}$$

$$\mathrm{H_3PO_{4(aq)}} \xleftrightarrow{\mathrm{K_{H_3PO_4}}} \mathrm{H^{+} + H_2PO_4{}^{-}};\quad \mathrm{K_{H_3PO_4}} = \frac{\{\mathrm{H^{+}}\}\{\mathrm{H_2PO_4{}^{-}}\}}{[\mathrm{H_3PO_{4(aq)}}]} \tag{3.58}$$

$$\mathrm{H_2PO_4{}^{-}} \xleftrightarrow{\mathrm{K_{H_2PO_4^-}}} \mathrm{H^{+} + HPO_4{}^{2-}};\quad \mathrm{K_{H_2PO_4}} = \frac{\{\mathrm{H^{+}}\}\{\mathrm{HPO_4^{2-}}\}}{[\mathrm{H_2PO_4^{-}}]} \tag{3.59}$$

$$\mathrm{HPO_4{}^{2-}} \xleftrightarrow{\mathrm{K_{HPO_4^{2-}}}} \mathrm{H^{+} + PO_4{}^{3-}};\quad \mathrm{K_{HPO_4^{2-}}} = \frac{\{\mathrm{H^{+}}\}\{\mathrm{PO_4{}^{3-}}\}}{[\mathrm{HPO_4{}^{2-}}]} \tag{3.60}$$

$$\mathrm{NH_4{}^{+}} \xleftrightarrow{\mathrm{K_{NH_4^+}}} \mathrm{H^{+} + NH_3};\quad \mathrm{K_{NH_4^+}} = \frac{\{\mathrm{H^{+}}\}[\mathrm{NH_3}]}{\{\mathrm{NH_4{}^{+}}\}} \tag{3.61}$$

$$\mathrm{H_2O} \xleftrightarrow{\mathrm{K_{H_2O}}} \mathrm{H^{+} + OH^{-}};\quad \mathrm{K_{H_2O}} = \frac{\{\mathrm{H^{+}}\}\{\mathrm{OH^{-}}\}}{[\mathrm{H_2O}]} \tag{3.62}$$

$$\gamma_{H^+}[\mathrm{H^{+}}] = 10^{-\mathrm{pH}} \tag{3.63}$$

In ionic reactions the product precipitates once, the species concentration exceeds the solubility product, therefore the system reaches the metastable regime. The thermodynamic solubility product of struvite K_{sp} is defined as:

$$K_{sp} = \{\mathrm{Mg^{2+}}\}\{\mathrm{NH_4{}^{+}}\}\{\mathrm{PO_4{}^{3-}}\} \tag{3.64}$$

Equilibrium constants found in the literature are usually provided at the standard temperature of 25°. In order to calculate the solubility product at any temperature a correction factor has to be introduced. This is achieved using Van't Hoff equation [113] as follows:

$$\ln K = \ln K_{25} - \frac{\Delta H^0}{R}\left[\frac{1}{T} - \frac{1}{T_0}\right] \tag{3.65}$$

where K_{25} is the equilibrium constant at 25°, $R = 0.008314$ kJ mol^{-1}deg^{-1} is the ideal gas constant and ΔH^0 is the enthalpy of reaction. Values for the enthalpies of reaction have been provided by Bhuiyan et al. [17].

In addition to Van't Hoff equation, the solubility product of struvite can also be

adjusted using an empirical formula [16] as follows:

$$\log_{10} K_{sp} = -1157.45 - 0.784T - \frac{63.86}{T} + 556.83 \log_{10} T + \frac{19.54}{T^2} \tag{3.66}$$

Throughout this thesis however, all of the studies performed rely on the assumption of the standard temperature conditions, therefore values for the equilibrium constants used are the ones provided by the literature. Values of the solubility products used are provided in the table below:

Table 3.1: Equilibrium constant values at the standard temperature of 25°

Equilibrium constant	Value	Reference
K_{MgOH^+}	$10^{-2.56}$	[30]
K_{MgHPO_4}	$10^{-2.91}$	[86]
$K_{MgH_2PO_4^+}$	$10^{-0.45}$	[86]
$K_{MgPO_4^-}$	$10^{-4.80}$	[86]
$K_{H_3PO_4}$	$10^{-2.15}$	[86]
$K_{H_2PO_4^-}$	$10^{-7.20}$	[94]
$K_{HPO_4^{2-}}$	$10^{-12.35}$	[94]
$K_{NH_4^+}$	$10^{-9.25}$	[131]
K_{H_2O}	10^{-14}	[124]
K_{sp}	$10^{-13.26}$	[17]

Ionic activity coefficients γ defined in Equation 3.53 depend on the ionic strength of the solution and the valence charge of the species A^+ calculated either using Debye-Hückel equation, Debye-Hückel with Güntelberg approximation [97], Davies equation [37] or Bromley's method [24].

Debye-Hückel equation

$$\ln \gamma_i = -A_{DH} Z_i^2 \sqrt{I} \tag{3.67}$$

Debye-Hückel with Güntelberg approximation

$$\ln \gamma_i = -A_{DH} Z_i^2 \left(\frac{\sqrt{I}}{1 + \sqrt{I}} \right) \tag{3.68}$$

Davies equation

$$\ln \gamma_i = -A_{DH} Z_i^2 \left(\frac{\sqrt{I}}{1+\sqrt{I}} \right) - 0.3I \tag{3.69}$$

Bromley's method

$$\ln \gamma_i = -A_\gamma Z_i^2 \frac{\sqrt{I}}{1+\sqrt{I}} + \frac{(0.06 + 0.6 Z_i^2 B) I}{\left(1 + \frac{1.5}{Z_i^2} I\right)^2} + BI \tag{3.70}$$

where Z_i is the ionic charge of the ith specie. The Debye-Hückel constant A_{DH} varies depending on the temperature T in Kelvin and can be calculated using the formula

$$A_{DH} = 0.486 - 6.07 \times 10^{-3} T + 6.43 \times 10^{-6} T^2,$$

however temperature changes were not considered in this study and constant values were used throughout, e.g. $A_{DH}(25^\circ) = 0.509$. Constant B, used in Bromley's method, is calculated using the individual ion values (δ_+ and δ_-) together with the cation B_+ and anion B_- values as:

$$B = B_+ + B_- + \delta_+ \delta_-.$$

where individual ionic contributions are presented in Table 3.2.

Table 3.2: Individual ionic contributions of B_+, B_-, δ_+ and δ_- for constant B (Söhnel and Garside [125])

Ions	B_+	B_-	δ_+	δ_-
Mg^{2+}	0.057	-	0.157	-
$NH_4{}^+$	-0.042	-	-0.02	-
$PO_4{}^{3-}$	-	0.024	-	-0.07

Ionic strength of the solution is calculated as in equation 3.71:

$$I = \frac{1}{2} \sum_i C_i Z_i^2 \tag{3.71}$$

where total concentrations of Mg, PO_4, NH_4 are used to determine the ionic strength of the solution.

The Debye-Hückel equation can be applied for solutions with $I < 0.005M$ [97], whilst the Güntelberg approximation can be applied for sparingly soluble electrolytes and is valid for $I < 0.1M$ and the Davies equation is known to provide accurate values of the activity coefficients for ionic strengths of $I < 0.6M$ [102], whereas Bromley's method gives good estimates up to $I = 6M$ [97, 125]. For this study, Davies equation has been employed, because ionic strengths found in WWTPs usually do not exceed the model validity limit of $0.6M$ [143].

Mole balances in the solution of Mg, NH_3 and PO_4 can now be written as follows:

$$\begin{aligned} C_P^T &= [H_3PO_4] + [H_2PO_3^-] + [HPO_4^{2-}] + [PO_4^{3-}] \\ &\quad + [MgH_2PO_4^+] + [MgHPO_4] + [MgPO_4^-] \end{aligned} \tag{3.72}$$

$$C_{Mg}^T = [Mg^{2+}] + [MgOH^+] + [MgH_2PO_4^+] + [MgHPO_4] + [MgPO_4^-] \tag{3.73}$$

$$C_N^T = [NH_3] + [NH_4^+] \tag{3.74}$$

Solving for the concentrations $[Mg^{2+}]$, $[PO_4^{3-}$ and $[NH_4^+]$ the following equations are obtained:

$$[Mg^{2+}] = \frac{(K_1 C_{Mg}^T - K_A - K_1 C_P^T) + \sqrt{(K_1 C_{Mg}^T - K_A - K_1 C_P^T)^2 + 4K_B C_{Mg}^T}}{2K_1 K_2} \tag{3.75}$$

$$[PO_4^{3-}] = \frac{C_P^T}{K_0 + K_1[Mg^{2+}]} \tag{3.76}$$

$$[NH_4^+] = \frac{C_N^T}{K_3} \tag{3.77}$$

where K_0, K_1, K_2, K_3, K_A, K_B are the constants defined bellow:

$$
\begin{aligned}
K_0 &= \left(\left(\frac{\{\mathrm{H}\}^3}{K_{\mathrm{H_2PO_4^-}} K_{\mathrm{H_2PO_4^-}} K_{\mathrm{HPO_4^{2-}}}} + \frac{\{\mathrm{H}\}^2}{K_{\mathrm{H_2PO_4^-}} K_{\mathrm{HPO_4^{2-}}}} + \frac{\{\mathrm{H}\}}{K_{\mathrm{HPO_4^{2-}}}} \right) \gamma_{\mathrm{PO_4^{3-}}} + 1 \right) \\
K_1 &= \left(\frac{G_1 \{\mathrm{H}\}^2}{K_{\mathrm{MgH_2PO_4^+}} K_{\mathrm{H_2PO_4^-}} K_{\mathrm{HPO_4^{2-}}}} + \frac{G_2 \{\mathrm{H}\}}{K_{\mathrm{MgHPO_4}} K_{\mathrm{HPO_4^{2-}}}} + \frac{G_3}{K_{\mathrm{MgPO_4^-}}} \right) \gamma_{\mathrm{PO_4^{3-}}} \gamma_{\mathrm{Mg^{2+}}} \\
K_2 &= \frac{\gamma_{\mathrm{Mg^{2+}}} \{\mathrm{OH^-}\}}{K_{\mathrm{MgOH^+}}} + 1 \\
K_3 &= \frac{\gamma_{\mathrm{NH_4^+}} K_{\mathrm{NH_4^+}}}{\{\mathrm{H}\}} \\
K_A &= K_0 K_2; \\
K_B &= K_0 K_1 K_2.
\end{aligned}
$$

with constants G_1, G_2, G_3 here defined as:

$$
\begin{aligned}
G_1 &= \frac{1}{\gamma_{\mathrm{MgH_2PO_4^+}}} \\
G_2 &= \frac{1}{\gamma_{\mathrm{MgHPO_4}}} \\
G_3 &= \frac{1}{\gamma_{\mathrm{MgPO_4^-}}}
\end{aligned}
$$

Full derivation of Equations 3.75 - 3.77 can be found in Appendix B.

Having established the methodology for calculating the concentrations of the ions that are involved in the MAP precipitation reaction it is now important to cover the criteria that determine whether the process occurs or not. A solution that is in thermodynamic equilibrium with the solid phase, at a some temperature, is said to be saturated. When the concentration of the reactant species exceeds the level indicated by the solubility product, then the solution is supersaturated and the products species would form until the solution reaches the equilibrium region. The supersaturated region can be subdivided into two sub-regions, described as the metastable region and the labile region[97]. In both the precipitation processes can occur, however only in the labile region can spontaneous precipitation (sometimes referred to as homogeneous precipitation) happen, whereas in the metastable regime it is improbable and seeding crystals would be required for precipitation to occur (this can be referred to as heterogeneous precipitation).

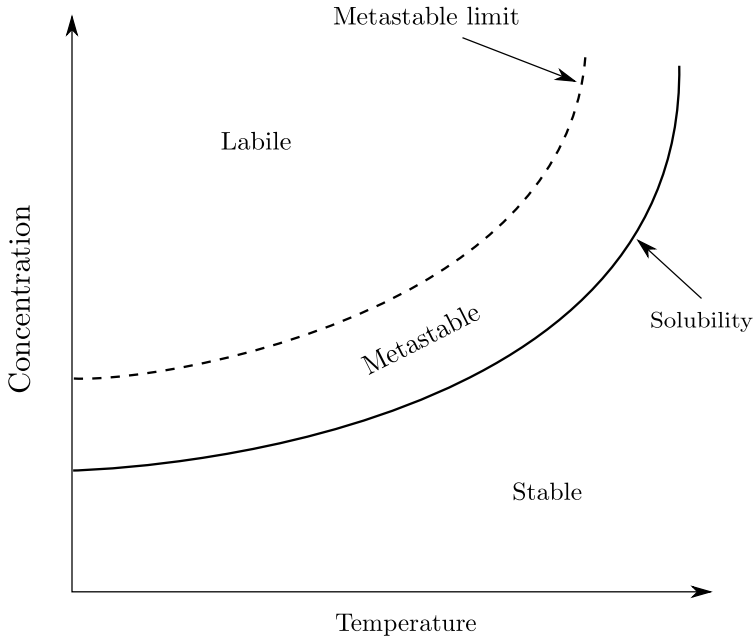

Figure 3.1: Solubility graph;

The solubility diagram of these three regions is shown in Figure 3.1. Metastable limit or supersolubility curve indicated by the dashes is not well defined, but it is well known that such a region exists [97].

Table 3.3 provides the summary of these region properties w.r.t. the types of precipitation.

Table 3.3: Solution saturation region properties

Region	Heterogeneous precipitation	Homogeneous precipitation
Stable	No	No
Metastable	Yes	Improbable
Labile	Yes	Yes

Definitions of supersaturation

The level of supersaturation in the system can be expressed in multiple ways and,

as will be seen later in this thesis, different expressions are used in the literature. For a single component the simplest way to indicate the level of supersaturation of the solution is to define it in terms of the concentration driving force ΔC:

$$\Delta C = C - C_{\text{eq}} \tag{3.78}$$

where C_{eq} is the equilibrium concentration value, i.e. solubility curve threshold at a given temperature. For systems involving struvite precipitation concentration the driving force is usually calculated w.r.t. the concentration of phosphate. It has to be pointed out that equation 3.78 should only be used for single reactant systems, therefore it is not an acceptable indicator for struvite precipitation.

Other single specie based indicators are the supersaturation ratio Ω and the relative supersaturation σ defined below:

$$\Omega = \frac{C}{C_{\text{eq}}} \tag{3.79}$$

$$\sigma = \frac{\Delta C}{C_{\text{eq}}} = \Omega - 1 \tag{3.80}$$

Supersaturation of sparingly soluble salts should be formulated with respect to the solubility product (as defined in Equation 3.64) and ionic activity product [97, 99], therefore the supersaturation ratio and the ionic activity product are as follows:

$$\Omega = \left(\frac{IAP}{K_{sp}}\right)^{1/N} \tag{3.81}$$

$$IAP = \prod_{i=1}^{N} \{A_i\} \tag{3.82}$$

where N is the number of participating reactants in precipitation and $\{A_i\}$ is the ionic activity as described in Equation 3.53. Similarly the absolute and the relative supersaturation indicators are defined as:

$$S = IAP^{1/N} - K_{sp}^{1/N} \tag{3.83}$$

$$\sigma = \frac{S}{K_{sp}^{1/N}} = \Omega - 1 \tag{3.84}$$

In conjunction with these parameters, the saturation index is also often used (eq. 3.85). Specific examples will be given later in the discussion where precipitation

kinetics mechanisms are discussed.

$$S_I = \log_{10}(IAP) - \log_{10}(K_{sp}) = \log_{10}\left(\frac{IAP}{K_{sp}}\right) \tag{3.85}$$

For the struvite precipitation system these parameters can be expressed as presented in the following equations:

$$IAP = \{PO_4^{3-}\}\{NH_4^+\}\{Mg^{2+}\} \tag{3.86}$$

$$\Omega = \left(\frac{\{PO_4^{3-}\}\{NH_4^+\}\{Mg^{2+}\}}{K_{sp}}\right)^{1/3} \tag{3.87}$$

$$S = \left(\{PO_4^{3-}\}\{NH_4^+\}\{Mg^{2+}\}\right)^{1/3} - K_{sp}^{1/3} \tag{3.88}$$

$$\sigma = \left(\frac{\{PO_4^{3-}\}\{NH_4^+\}\{Mg^{2+}\}}{K_{sp}}\right)^{1/3} - 1 \tag{3.89}$$

$$S_I = \log_{10}\left(\frac{\{PO_4^{3-}\}\{NH_4^+\}\{Mg^{2+}\}}{K_{sp}}\right) \tag{3.90}$$

This thermodynamic description of the system is now sufficient to provide a consistent and physically valid results for the struvite reaction. In the following section it is shown how two dominant processes in MAP precipitation, i.e. nucleation and growth, are controlled by the levels of supersaturation in the system.

As it has been mentioned earlier, precipitation kinetics found in the literature are often formulated using one or a combination of saturation indicators eqs. 3.87-3.90. Therefore, throughout this study all of these indicators will be used.

3.3.3 Precipitation kinetic models of struvite

Formation of struvite crystals is a complicated process that can be controlled by different possible kinetic mechanisms that tend to differ between different product compounds. Fundamentally there can be 4 types of mechanisms involved in crystallisation process:

- Nucleation dictates the rate of birth of crystals inside the liquid. It is the first state of the crystalization process where crystal embryos are being formed due to supersaturation levels in the liquid;

- Growth mechanism describes the change in size of the crystal embryos, until the equilibrium state has been achieved;
- Aggregation process dictates the rate at which particles due cluster together to form a larger particles through collision process;
- Breakage dictates the rate at which larger particle clusters are broken up into smaller clusters due to collisions in the particulate system.

Depending on the chemical and physical properties of the reactants and the products some of these mechanisms can be more dominant than others. As of the current date it has been reported that nucleation and growth are the main mechanisms participating in struvite precipitation [55, 75], although the exact rates at which these processes occur and the mathematical relationships vary depending on the experimental setups and conditions, the dependency has been confirmed. Galbraith et al. [50] also reported effects of size-independent aggregation on struvite formation, however there is little evidence from other sources that aggregation is a dominant enough process to be considered in this study.

Nucleation mechanisms

Through the nucleation process the ions in the liquid solution combine to form crystal embryos (Mullin [97]). There are two types of nucleation possible: a) Primary; b) Secondary.

Homogenous primary nucleation occurs in the solution due to high levels of supersaturation [100], therefore this is the mechanism behind spontaneous precipitation. Heterogeneous primary nucleation is induced by the presence of foreign particles or the surfaces of the system (e.g. pipe walls) both of which serve as a foundation site for struvite crystals to form.

Secondary nucleation is induced by the crystals themselves and can be understood as the process that occurs due to the interaction between the micro-crystals and the macro-crystals in the liquid solution [75].

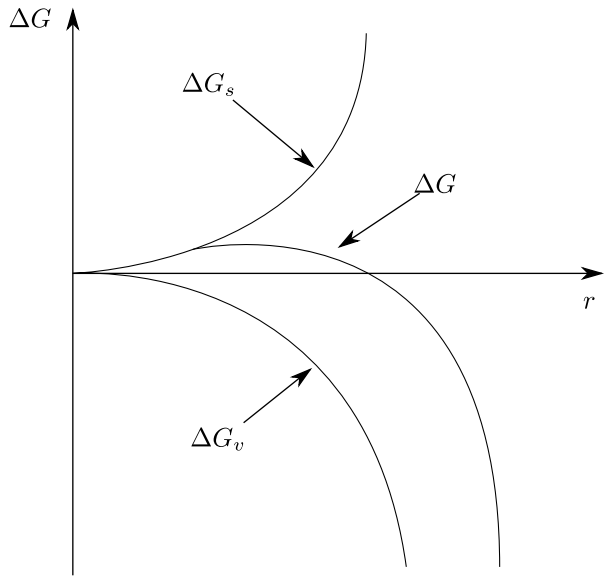

Figure 3.2: Gibbs free energy against the radius r of the nucleus (adapted from Mersmann [91])

Thermodynamically the nucleation process is manifested by a balance between the excess free energy due to volume ΔG_v and the excess free energy of the surface ΔG_s [91, 97]. Therefore the total change in Gibbs free energy ΔG_{Gibbs} can be calculated as follows.

$$\Delta G_{\text{Gibbs}} = \Delta G_s + \Delta G_v \tag{3.91}$$

The volume excess energy is defined as the free energy between the solute in the liquid solution and the volume of an infinitely large particle, whereas the surface excess energy is defined as the free energy between the surface and the bulk of the particle, therefore proportionality relationships with respect to the radius of the nucleus r are:

$$\Delta G_s \propto r^2$$
$$\Delta G_v \propto r^3$$

Figure 3.2 illustrates the fundamental relationship between excess energies involved in nucleus formation processes. Assuming the particles are spherical then the free energy can be expressed as follows (Randolph and Larson [116]:

$$\Delta G_{\text{Gibbs}} = 4\pi r^2 \gamma + \left(\frac{4}{3}\pi r^3\right)\Delta G_v \tag{3.92}$$

where δ is the specific surface energy and r is the radius of the nucleus.

Homogeneus nucleation

Based on classical nucleation theory [97, 99] the free energy of homogeneous nucleation can be written as:

$$\Delta G_{\text{Gibbs}} = -\left(\frac{v_p}{v_m}\right) k_B T \ln(\Omega) + \gamma a \tag{3.93}$$

where $v_p = \phi_v r^3$ is the volume of the aggregate; $a = \phi_a r^2$ is the surface of the aggregate; v_m is the molecular volume of the precipitated nucleus; k_B is the Boltzmann constant; T is the absolute temperature, and ϕ_v, ϕ_a are the volume and surface shape factors respectively. Commonly known as the Volmer and Weber equation [110], the nucleation rate is expressed as follows:

$$J = A \exp\left(-\frac{16\pi\gamma^3 v_m^2}{3k_B^3 T^3 \ln(\Omega)}\right) \tag{3.94}$$

where A is the nucleation rate factor with dimensions of $\left[\text{nuclei}\, m^{-3}\right] s^{-1}$. Most often in the literature the terms inside the exponential are combined in to a single activation energy parameter B. The values of the rate coefficient and the activation parameter are then determined through parameter fitting to the available experimental data (e.g. Hanhoun et al. [55]):

$$J = A \exp\left(-\frac{B}{\ln(\Omega)}\right) \tag{3.95}$$

It has been shown by Nielsen [99] that in barium sulphate precipitation the nucleation can be approximated by power law equations. Even though such a kinetic law was first formulated for the barium sulphate system it has been applied to struvite precipitation and it has been shown to produce good correlation with the experimental data [55]. Slightly different power law formulations can and have been used in the literature [50, 50, 145], all of which differ by the choice of the supersaturation indicator, however they all follow the same principles. The possible

power law formulations are as follows:

$$J = k_J S^{n_J} \tag{3.96}$$

$$J = k_J \sigma^{n_J} \tag{3.97}$$

$$J = k_J S_I^{n_J} \tag{3.98}$$

where the kinetic rate k_J and the nucleation order n_J parameters are estimated through parameter fitting against the experimental data.

Heterogeneous nucleation

Heterogeneous nucleation occurs in the presence of foreign surfaces and it is the most likely primary nucleation process to happen as it requires lower saturation levels than homogeneous nucleation [75]. The rates at which heterogeneous nucleation occurs can be represented by the same laws presented in Equations (3.95, 3.96, 3.97, 3.98), however the kinetic parameters such as A, B or k_J, n_J would have different values which will have to be determined through experiments.

Secondary nucleation

The secondary nucleation mechanism is likely to dominate the process when the precipitant crystals are already present in the solution. Experimentally the presence of precipitant in a solution is usually achieved by specially seeding the solution prior to the experiment [90]. Similarly as before the nucleation rate can be characterised using a power law expression, however a secondary nucleation threshold has to be introduced. Mehta and Batstone [90] determined secondary nucleation rates for struvite in a pre-seeded solution, where the kinetic law was expressed in terms of relative saturation indicator σ and the threshold saturation σ_i:

$$J = k_J(\sigma - \sigma_i)^{n_J} \tag{3.99}$$

Growth kinetic mechanism

During the crystal growth stage of precipitation, newly formed crystal embryos interact with each other, foreign molecules or with the impurities in the system

to form bigger particles that would be of a detectable size [75]. The process is either controlled by the mass transfer between the solid and liquid phases or by the kinetics of surface integration. The mass transfer processes would correspond to the transport of mass from the liquid to the solid through diffusion, convection controlled mechanisms or by both. Surface integration mechanisms occur due to integration of new molecules onto the surface of the nucleus crystal lattice due to the surface integration mechanism.

Growth kinetics are characterised by the growth rate G with dimensions $[m\,s^{-1}]$, therefore the growth can be understood as the velocity of the particle size. From the theoretical standpoint the growth rate has the following expression:

$$G(\xi) = \frac{\mathrm{d}\xi}{\mathrm{d}t} \tag{3.100}$$

Based on the diffusion-reaction theory the growth rate is proportional to the concentration driving force, which is formulated as follows:

$$G(\xi) = \frac{\mathrm{d}\xi}{\mathrm{d}t} = k_G(C - C^*)^{n_G} \tag{3.101}$$

where C^* is the threshold concentration for the growth mechanism to occur; k_G is specific growth rate, that is a function of the surface integration (k_r) and the diffusive mass transfer (k_d) coefficients (Mullin [97]).

For systems dominated by diffusive mass transfer growth, i.e. diffusion-limited, k_G is independent of the size of the crystals. If the growth process is diffusion-controlled then it is known that it should follow first-order kinetics, i.e. $n_G = 1$. For cases where $n_G > 1$ the growth is controlled by the surface integration, which depends on the particle size, crystal lattice structure, etc., therefore the growth rate might be size dependent.

Crystal growth mechanisms do not have a theory derived from the first principles, however there have been many proposed and discussions on those can be found in textbooks by Jones [69], Mullin [97], Randolph and Larson [116]. In addition to the lack of an established theory of crystal growth, the parameters for models

suggested in the textbooks mentioned are often difficult to determine experimentally, therefore from the engineering standpoint it is often better to determine the parameters in Equation 3.101 through parameter fitting. Also, most of the authors, use alternative formulation to Equation 3.101, and have it expressed in terms of one of the saturation indicators presented earlier in this chapter. The formulation found throughout the literature are presented as follows:

$$G(\xi) = k_G S^{n_G} \tag{3.102}$$

$$G(\xi) = k_G \sigma^{n_G} \tag{3.103}$$

$$G(\xi) = k_G S_I^{n_G} \tag{3.104}$$

3.4 Population balance modelling

A key difference between systems that involve reactive crystallization as opposed to other reactive systems is that the properties of the dispersed phase change over time whereas in other systems this would not be the case. There are four fundamental mechanisms that impact the properties of the crystals: nucleation, growth, aggregation and breakage. The nucleation mechanism represents the manifestation of new particles into the system due to precipitation reaction. The growth mechanism describes the enlargement of the crystals in the system. Aggregation and breakage represent the enlargement or shrinkage of the particles in the system due to collisions.

Standard practice in chemical engineering is to employ the Population Balance Equation (PBE) to model the effects of the aforementioned mechanisms on the size distribution of the crystals (sometimes PBE is referred to as particle number continuity equation). However, the analytical solutions are available only for a limited number of simplified cases, therefore in order to solve the PBE there have been different approximations and closure methods developed. Throughout this section these approximation and solution approaches are discussed.

3.4.1 Population Balance Equation

For this study a single internal coordinate systems were considered, where an internal coordinate would represent the radius of the particles. We present a formulation of general uni-variate based population balance equations (for full derivation see [80, 82, 84, 115]):

$$\underbrace{\frac{\partial n(t,\mathbf{x},\xi)}{\partial t}}_{\text{Temporal term}} - \underbrace{\nabla\cdot(\Gamma\nabla n(t,\mathbf{x},\xi))}_{\text{Diffusion}} + \underbrace{\nabla\cdot(n(t,\mathbf{x},\xi)\mathbf{U})}_{\text{Convection}} + \underbrace{\frac{\partial}{\partial\xi}(G(t,\mathbf{x},\xi)n(t,\mathbf{x},\xi))}_{\text{Internal coordinate diffusion}} = \underbrace{h(t,\mathbf{x},\xi)}_{\text{Sources/Sinks}} \tag{3.105}$$

where the $h(\xi,\mathbf{x},t)$ term represents all sources and sinks in the equation and $G(t,\mathbf{x},\xi)$ represents the specific growth rate of the NDF. In general PBE sources/sinks are attributed to either aggregation or breakup phenomena as shown in Equation 3.106 and each of the terms are defined by Equations (3.107,3.108, 3.109, 3.110).

$$h(t,x,\xi) = B_{agg}(t,x,\xi) - D_{agg}(t,x,\xi) + B_{br}(t,x,\xi) - D_{br}(t,x,\xi), \tag{3.106}$$

$$B_{agg}(\xi,\mathbf{x},t) = \frac{\xi^2}{2}\int_0^{\xi}\frac{\beta\left((\xi^2-\xi'^2)^{1/3},\xi'\right)}{(\xi^3-\xi'^3)^{2/3}}n\left((\xi^3-\xi'^3)^{1/3},\mathbf{x},t\right)n(\xi',\mathbf{x},t)\,\mathrm{d}\xi', \tag{3.107}$$

$$D_{agg}(\xi,\mathbf{x},t) = n(\xi,\mathbf{x},t)\int_0^{\infty}\beta(\xi,\xi')n(\xi',\mathbf{x},t)\,\mathrm{d}\xi', \tag{3.108}$$

$$B_{br}(\xi,\mathbf{x},t) = \int_{\xi}^{\infty}a(\xi')b(\xi|\xi')n(\xi',\mathbf{x},t)\,\mathrm{d}\xi', \tag{3.109}$$

$$D_{br}(\xi,\mathbf{x},t) = a(\xi)n(\xi,\mathbf{x},t). \tag{3.110}$$

where the terms in Equations 3.107 - 3.110 are defined as follows:

$\beta(\xi, \xi^{'}) =$ aggregation kernel representing the frequency at which two particles of sizes ξ and $\xi^{'}$ collide to form a new particle of size $\xi + \xi^{'}$;

$a(\xi) =$ breakage kernel representing specific breakage rate for a ξ sized particle;

$b(\xi|\xi^{'}) =$ fragment distribution function for particles of size ξ that carries information about the particle fragments created during breakage event.

3.4.2 PBE solution methods

Only a small number of cases allow analytical solutions to be obtained for the population balance equation, therefore some solution strategy has to be employed. Over the years there have been different methods proposed and used, each of which have positive and negative aspects (Class Method (CM) [73], Monte Carlo (MC) [115], Method Of Moments (MOM) [60] are amongst the most common and popular).

Monte Carlo methods provide flexibility and accuracy to track particle distribution changes in a multidimensional space. However, the methods have high accuracy only when a large number of particles is used, which then leads to large requirements of computational power and time that are required in order to obtain a viable solution. In addition to the computing power needed, it is reported that the coupling of a CFD framework to the MC methodology is not a straightforward process [147]. From an engineering standpoint the lack of flexibility in terms of computational resources required for MC means that this method would not be viable for the industrial engineering cases such as those found in WWTPs.

The other common methods used are the class method and the method of moments, both of which provide reasonably reliable solutions with lower computational expenses than MC methods. The main principles behind these methods are explained further in this section.

3.4.3 Class method

The Class method has received a significant amount of attention due fairly straightforward coupling with the CFD framework and the fact that the number density function is being solved directly. The main principle behind this approach is a discretisation of the NDF by a number of size classes. For illustrative purpose the discrete class method will be used here. Let us assume that the number density function $n(\mathbf{x}, t, \xi)$ can be discretised as follows:

$$n(\xi, \mathbf{x}, t) = \sum_{i=1}^{N} N_i(\mathbf{x}, t, \xi)\delta(\xi - \chi), \tag{3.111}$$

where N is the total number of classes that NDF is being discretised into; χ is the size of each class, which is constant in this particular example, in general this does not have to be the case. Graphically this process can be illustrated as presented in Figure 3.3.

Transport for each discrete size class can now be written as follows (for simplicity the growth term has been excluded):

$$\frac{\partial N_i(\mathbf{x}, t)}{\partial t} + \nabla \cdot (\mathbf{U}_{p,i} N_i(\mathbf{x}, t)) = h(\mathbf{x}, t) \tag{3.112}$$

where $\mathbf{U}_{p,i}$ is the local particle velocity.

Solution methods of the class equations, such as MUSIG [79], require the number of classes to be sufficiently large in order for the solution to be independent of the resolution of the internal coordinate ξ. Even though the computational requirements for class methods are lower than for the monte carlo methods, they are still very expensive to run when it comes down to working with realistic engineering cases [147].

3.4.4 Method of Moments

The method of moments first introduced by Hulburt and Katz [60] is considered to be a very practical approach to obtain reliable solutions of PBEs. The main principle behind method of moments and formulations based on it that have been

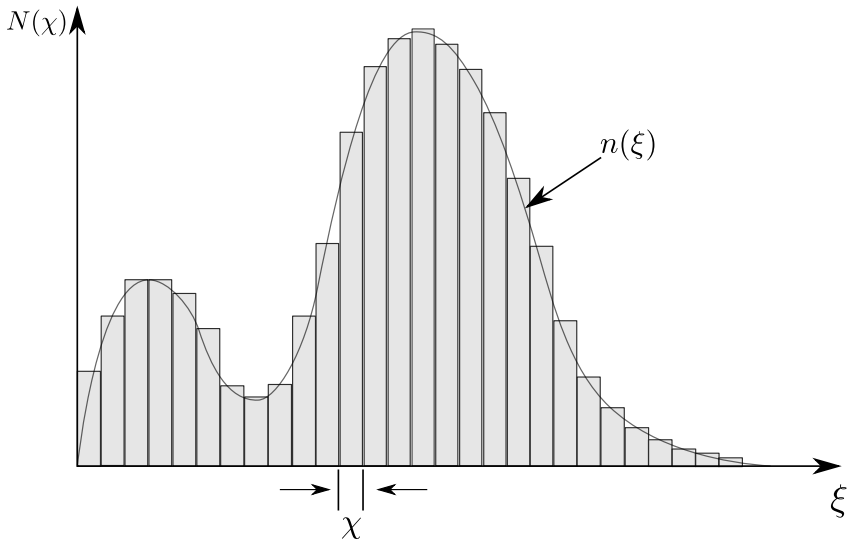

Figure 3.3: NDF phase space discretisation using Class method.

developed over the years rely on an approximation of the number density function in terms of a finite number of its statistical moments μ_i. This approach greatly reduces the dimensionality of the problem, because only the lower-order moments transport is being solved for. As will be described further in this section, the first five statistical moments of an NDF have a direct $1-1$ relation with physical properties of the system, which, from an engineers point of view, are the properties of interest when considering a particulate system evolution.

The kth moment of a crystal size distribution is given as:

$$\mu_k(\mathbf{x},t) = \int_0^{+\infty} n(\xi,\mathbf{x},t)\xi^k \,\mathrm{d}\xi$$

In order to transform the population balance equation 3.105 into a set of moment transport equations both sides are multiplied by the internal coordinate ξ^k and integrated with respect to the internal coordinate (note that for simplicity purposes the dependencies on the independent variables have been removed in the following equation):

$$\int_{\xi=0}^{\infty} \xi^k \Big(\frac{\partial n}{\partial t} - \nabla\cdot(\Gamma\nabla n) + \nabla\cdot(n\mathbf{U}) + \frac{\partial}{\partial\xi}(Gn)\Big)\,\mathrm{d}\xi = \int_{\xi=0}^{\infty} \xi^k (B_{agg} - D_{agg} + B_{br} - D_{br})\,\mathrm{d}\xi$$

Applying the moments transform identity the transport equation for individual moments is obtained (note that dependencies w.r.t. the independent variables have

been removed for simplicity):

$$\frac{\partial \mu_k(\mathbf{x},t)}{\partial t} + \nabla\cdot(\mu_k(\mathbf{x},t)\mathbf{U}) - \nabla\cdot(\Gamma\nabla\mu_k(\mathbf{x},t)) + G_k(\mathbf{x},t) = B_k^a(\mathbf{x},t) - D_k^a(\mathbf{x},t) + B_k^{br}(\mathbf{x},t) - D_k^{br}(\mathbf{x},t) + \mathcal{N}(\mathbf{x},t) \tag{3.113}$$

where $G_k(\mathbf{x},t)$ is the growth kernel for the kth moment; $B_k(\mathbf{x},t)$s and $D_k(\mathbf{x},t)$s are the birth and death source/sink terms respectively due to aggregation and breakage events; $\mathcal{N}(\mathbf{x},t)$ is the nucleation of term that carries information on the inception of new particles. Explicit definition of these terms is as follows:

$$G_k(\mathbf{x},t) = -k\int_0^\infty \xi^{k-1}G(\xi)n(\xi,\mathbf{x},t)\,\mathrm{d}\xi \tag{3.114}$$

$$B_k^\alpha(\mathbf{x},t) = \frac{1}{2}\int_0^\infty n(\xi',\mathbf{x},t)\int_0^\infty \beta(\xi,\xi')(\xi^3+\xi'^3)^{k/3}n(\xi,\mathbf{x},t)\,\mathrm{d}\xi\,\mathrm{d}\xi' \tag{3.115}$$

$$D_k^a(\mathbf{x},t) = \int_0^\infty \xi^k n(\xi,\mathbf{x},t)\int_0^\infty \beta(\xi,\xi')n(\xi',\mathbf{x},t)\,\mathrm{d}\xi'\,\mathrm{d}\xi \tag{3.116}$$

$$B_k^{br}(\mathbf{x},t) = \int_0^\infty \xi^k\int_0^\infty a(\xi')b(\xi|\xi')n(\xi',\mathbf{x},t)\,\mathrm{d}\xi'\,\mathrm{d}\xi \tag{3.117}$$

$$D_k^{br}(\mathbf{x},t) = \int_0^\infty \xi^k a(\xi)n(\xi,\mathbf{x},t)\,\mathrm{d}\xi \tag{3.118}$$

$$\mathcal{N}_k(\mathbf{x},t) = 0^k J(\mathbf{x},t) \tag{3.119}$$

Although the dimensionality of the equations have been reduced, the moment transport equations 3.113 are still too complicated to be solved straightforwardly. Having no access to the distribution function itself creates a closure problem, where assumptions have to be made in order to be able to solve the moments transport equations. In an attempt to do that one could assume the form of the CSD (e.g. Normal, log-normal, Gamma, Beta) which could be reconstructed from the lower order moments, however this approach removes the generality of the method and requires specific knowledge about the system that is not always attainable.

Alternatively, the Quadrature Method Of Moments (QMOM) proposed by McGraw [89] for studying nucleation and growth of aerosols and later extended for aggregation and breakage by Marchisio et al. [84] can be used. The method introduced the use of the Gaussian quadrature rule to close the unclosed terms in Equation 3.113. Using Gaussian quadrature a generic integral can be approximated using

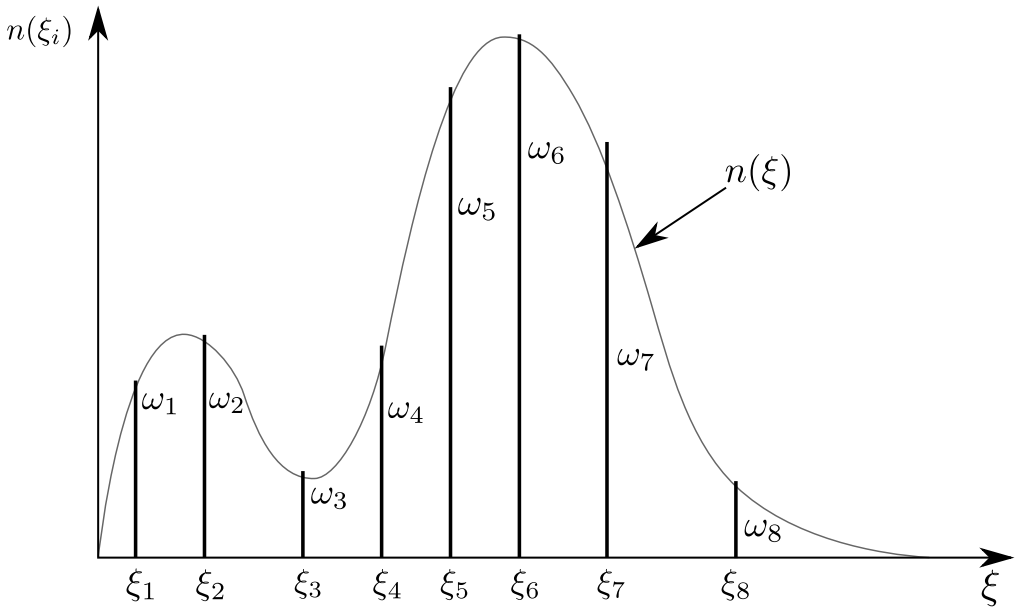

Figure 3.4: Graphical representation for quadrature approximation of the CSD.

the formula:

$$\int \omega(\xi) g(\xi)\, \mathrm{d}\xi \approx \sum_{\alpha=1}^{N} \omega_\alpha g(\xi_\alpha) + R_N(g) \tag{3.120}$$

where this quadrature formula is said to be Gaussian if and only if the abscissas ξ_α are the roots of an Nth order polynomial $p_N(\xi)$, which is orthogonal with respect to $n(\xi)$. If the polynomial $g(\xi)$ is of the order less than $2N$ then the formula is exact, i.e. $R_N(g) = 0$ [51].

Number density function in QMOM is approximated by with an Nth degree polynomial of Dirac-delta functions as follows:

$$n(\xi) \approx p_N(\xi) = \sum_{\alpha=1}^{N} \omega_\alpha \delta_\alpha(\xi - \xi_\alpha). \tag{3.121}$$

Graphical representation of this is shown in Figure 3.4. Applying equation 3.121 to the moment transform 3.113, the following approximation can be obtained:

$$\mu_k \approx \sum_{\alpha=1}^{N} \omega_\alpha \xi_\alpha^k \tag{3.122}$$

The main idea behind QMOM procedure is that the weights ω_α and the abscissas ξ_α can be specified from the lower order moments. It is sufficient to know the first $2N$ moments in order for the quadrature to be of the Nth order [83]. Even though

the use of the quadrature approach suffers from truncation errors it provides sufficient qualitative results for comparison against experimental data. The quadrature abscissas ξ_α and the weights ω_α can be obtained using the Product-Difference (PD) algorithm first proposed by Gordon [52] which is based on the theory of canonical moments by Dette and Studden [41] (see Marchisio et al. [83] for description of the PD algorithm). Once the abscissas and the weights are found the integrals involving the NDF can be computed using approximation 3.121.

The QMOM solution is provided in terms of the moments, therefore the size distribution is not present in the governing equations. This is not an issue, because the statistical moments have a direct relationship to the physical parameters (e.g. μ_0 represents the number of particles per volume), which are of more interest from an engineering perspective.

There is however one limitation of QMOM - kernel density functions are represented by the Dirac-delta function and it would be preferable if kernel density functions (KDF) were represented by some continuous distribution. Also, QMOM does not guarantee the positivity of the reconstructed CSD, i.e. the weights can become negative during the solution process [7]. In order to overcome these shortcomings, Yuan et al. [149] proposed an Extended Quadrature Method of Moments (EQMOM), which introduced a generalisation of quadrature formula with continuous KDF with finite or infinite support parameters:

$$n(\xi) \approx \sum_{\alpha=1}^{N} \omega_\alpha \delta_\sigma(\xi, \xi_\alpha) \tag{3.123}$$

where $\delta_\sigma(\xi, \xi_\alpha)$ is the KDF with a support parameter σ. The kernel density function can be represented by Gamma or Beta distributions as introduced by Yuan et al. [149], or by log-normal as shown by Madadi-Kandjani and Passalacqua [80]. Yuan et al. [149] also imposed a limiting requirement on the KDF, such that EQMOM is reduced to the QMOM formulation in the limit $\sigma \to 0$ as follows:

$$\lim_{\sigma \to 0} \delta_\sigma(\xi, \xi_\alpha) = \delta(\xi - \xi_\alpha) \tag{3.124}$$

In this study a log-normal distribution has been used throughout and it is formu-

lated as follows:

$$\delta_\sigma(\xi,\xi_\alpha)=\frac{1}{\xi\sigma\sqrt{2\pi}}\mathrm{e}^{-\frac{(\ln\xi-\xi_\alpha)^2}{2\sigma^2}},\quad \xi,\xi_\alpha,\sigma\in\mathbb{R}^+ \tag{3.125}$$

The support parameter σ in the equation 3.125 is determined by fixing an additional moment (i.e. moment set size in EQMOM is $2N+1$ as opposed to $2N$ as in QMOM). This introduction of an additional moment to the moment set has profound benefits over the QMOM procedure: as shown by Marchisio and Fox [85] it is now possible to reconstruct a non-negative and smooth distribution function that would closely reproduce the moment set. The reconstructed CSD would now be more likely to represent a physical crystal size distribution.

PBE using EQMOM

Using the relationships discussed throughout this section and applying them to the moments transport equation 3.113, the conservation equation is obtained:

$$\begin{aligned}\frac{\partial\mu_k(\mathbf{x},t)}{\partial t}&+\nabla\cdot(\mu_k(\mathbf{x},t)\mathbf{U})-\nabla\cdot(\Gamma\nabla\mu_k(\mathbf{x},t))+G_k(\mathbf{x},t)\\&=B_k^a(\mathbf{x},t)-D_k^a(\mathbf{x},t)+B_k^{br}(\mathbf{x},t)-D_k^{br}(\mathbf{x},t)+\mathcal{N}(\mathbf{x},t)\end{aligned} \tag{3.126}$$

where growth and source/sink terms are as follows:

- Growth term:

$$G_k(\mathbf{x},t)=-k\int_0^\infty\xi^{k-1}G(\xi)n(\xi,\mathbf{x},t)\,\mathrm{d}\xi\approx-k\sum_{\alpha=1}^{N}\omega_\alpha\sum_{\beta=1}^{N_\alpha}\omega_{\alpha\beta}\xi_{\alpha\beta}^{k-1}G(\xi_{\alpha\beta},\mathbf{x},t) \tag{3.127}$$

- Aggregation birth term:

$$\begin{aligned}B_k^\alpha(\mathbf{x},t)&=\frac{1}{2}\int_0^\infty n(\xi',\mathbf{x},t)\int_0^\infty\beta(\xi,\xi')(\xi^3+\xi'^3)^{k/3}n(\xi,\mathbf{x},t)\,\mathrm{d}\xi\,\mathrm{d}\xi'\\&\approx\frac{1}{2}\sum_{\alpha_1=1}^{N}\omega_{\alpha_1}\sum_{\beta_1=1}^{N_\alpha}\omega_{\alpha_1\beta_1}\sum_{\alpha_2=1}^{N}\omega_{\alpha_2}\sum_{\beta_2=1}^{N_\alpha}\omega_{\alpha_2\beta_2}(\xi_{\alpha_1\beta_1}^3+\xi_{\alpha_2\beta_2}^3)^{k/3})\beta_{\alpha_1\beta_1\alpha_2\beta_2}\end{aligned} \tag{3.128}$$

- Aggregation death term:

$$D_k^a(\mathbf{x},t) = \int_0^\infty \xi^k n(\xi,\mathbf{x},t) \int_0^\infty \beta(\xi,\xi^{'}) n(\xi^{'},\mathbf{x},t)\,\mathrm{d}\xi^{'}\,\mathrm{d}\xi \approx \sum_{\alpha_1=1}^{N} \omega_{\alpha_1} \sum_{\beta_1=1}^{N_\alpha} \omega_{\alpha_1\beta_1} \xi_{\alpha_1\beta_1}^k \sum_{\alpha_2=1}^{N} \omega_{\alpha_2} \sum_{\beta_2=1}^{N_\alpha} \omega_{\alpha_2\beta_2} \beta_{\alpha_1\beta_1\alpha_2\beta_2} \tag{3.129}$$

- Breakup birth term:

$$B_k^{br}(\mathbf{x},t) = \int_0^\infty \xi^k \int_0^\infty a(\xi^{'}) b(\xi|\xi^{'}) n(\xi^{'},\mathbf{x},t)\,\mathrm{d}\xi^{'}\,\mathrm{d}\xi \approx \sum_{\alpha=1}^{N} \omega_\alpha \sum_{\beta=1}^{N_\alpha} \omega_{\alpha\beta} a_\alpha b_{\alpha\beta}^k \tag{3.130}$$

- Breakup death term:

$$D_k^{br}(\mathbf{x},t) = \int_0^\infty \xi^k a(\xi) n(\xi,\mathbf{x},t)\,\mathrm{d}\xi \approx \sum_{\alpha=1}^{N} \omega_\alpha \sum_{\beta=1}^{N_\alpha} \omega_{\alpha\beta} \xi_{\alpha\beta}^k a_{\alpha\beta} \tag{3.131}$$

- Nucleation term:

$$\mathcal{N}_k(\mathbf{x},t) = 0^k J(\mathbf{x},t) \tag{3.132}$$

The final step required to close the moment conservation equations would be to provide appropriate breakage, aggregation, growth and nucleation kernels. Kinetic mechanisms involved struvite precipitation reactions have been discussed in section 3.3.3, therefore in this study the aggregation and breakage processes were not considered and only size independent growth and nucleation mechanisms were considered. The final transport equation used throughout this study can be written as follows:

$$\frac{\partial \mu_k(\mathbf{x},t)}{\partial t} + \nabla \cdot (\mu_k(\mathbf{x},t)\mathbf{U}) - \nabla \cdot (\Gamma \nabla \mu_k(\mathbf{x},t)) + G_k(\mathbf{x},t) = \mathcal{N}(\mathbf{x},t) \tag{3.133}$$

From the mathematical perspective the moment transport equations have been formulated using the extended quadrature method of moments methodology. The specific numerical aspects such as the spatial and temporal discretisation and moment inversion algorithm will be covered in Chapter 4.

3.5 Closure

First of all in this chapter different modelling approaches for multi-phase flow have been discussed: Lagrangian, Two-fluid model and mixture model. It has been concluded that the Lagrangian approach is not a viable choice due to the computational requirements associated with such approach. In order to get a statistically reliable solution using the Lagrangian approach the number of particles would be very large, therefore this modelling process is unsuitable for the industrial cases that this study was aimed for.

The Eulerian approach which follows the assumption that the phases can be treated as two inter-penetrating continua has been considered to be a more suitable option when it comes down to modelling precipitation processes and particle settling. The most general Eulerian formulation, the two-fluid model, has been described and different aspects of the derivation procedure have been covered. However, one of the issues with the two-fluid model is that separate transport equations have to be solved for each of the phases in the domain, therefore a simplification of the TFM model has been sought.

The group of simplified models discussed are the mixture models, that all still follow the assumption of the two-phase system as inter-penetrating fluids, however the main difference is the formulation of the key physical parameters in terms of the mixture parameter. Such simplification reduces the number of transport equations that require solution, which is a beneficial aspect when considering large industrial cases. The specific mixture model, namely the Drift-flux model, has been chosen as a formulation that will be used in this study due to its previous good results in sludge settling scenarios. One of the terms that requires empirical closure relationships in the drift-flux model is the settling velocity or drift velocity, which in the past has been assumed to have a fixed terminal velocity value. However, due to the nature of this study the properties of the dispersed phase are varying, therefore it has been proposed that the terminal velocity value would be varying with respect to the Sauter mean diameter, which is calculated from the population

balance transport and defined in Equation 3.44.

Other key aspects discussed were the specific aspects of the formulation behind the precipitation reaction modelling. Equilibrium thermodynamics plays a huge role behind such type of reactions therefore descriptions of the ionic speciation and the supersaturation modelling have provided. Also key kinetic mechanisms that are known to be dominant in struvite precipitation have been provided and the applications of those will be given in the later chapters.

In order to capture the change in the properties of the dispersed phase the chemical engineering industry standard modelling methodology is to use the population balance approach, which creates a set of issues on its own, let alone when coupled with the CFD framework. Different modelling approaches have been discussed, each of which have benefits and drawbacks. In the end an Extended Quadrature Method of Moments solution method has been used, and the mathematical formulation for the transport equations have been provided.

Chapter 4

Numerical implementation

This chapter is divided into two main parts. The first part covers key aspects of the Finite Volume (FV) discretisation procedure which is used to solve the multiphase flow equations described in Chapter 3. FV discretisation has now become one of the industry standard approaches and has been extensively covered throughout the literature, therefore only a brief discussion on computational domain and term by term discretisation has been included.

The second part is intended to look into specific numerical aspects of the Extended Quadrature Method of Moments. Any method of moments relies on the assumption that a given number density function can be approximated by a finite number of its statistical moments. This way the dimensionality and complexity of the initial problem is reduced significantly, unfortunately this comes with its own set of challenges and restrictions. The main problem arises when the set of moments that have been solved for cannot reproduce the mathematically valid NDF, therefore great care is needed to ensure that the moments solution is mathematically appropriate.

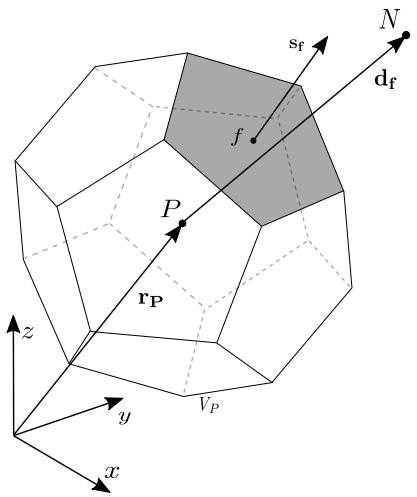

Figure 4.1: Control volume representation (adapted from Jasak [66]).

4.1 Finite Volume Discretisation

The Finite Volume Method like other numerical methods for fluid flow simulation [109] involves a transformation of a set of partial differential equations into a system of linear algebraic equations. This is achieved by performing two steps: *a*) transformation of the continuous domain into a computational mesh of a set of Control Volumes (CV) or cells; *b*) discretisation of partial differential equations.

The following few sections will briefly cover these two steps.

4.1.1 Discretisation of the Computational Domain

Discretisation of the physical domain produces a computational mesh. Finite volume method used in this study uses a whole domain subdivided into a set of non-overlapping control volumes. Information about all variables is of the stored at the centroids of each CV (i.e. staggered/collocated grid [48, 96]). The control volume has a general polyhedral shape and as seen in Figure 4.1 is geometrically bounded by a set of flat faces each of which can either be shared by another control

volume or by a domain boundary.

A complete description of the discretised physical domain is achieved by assigning each CV a set of parameters. The global positional vector $\mathbf{r_P}$ is prescribed with respect to the cartesian origin of the computational domain. Distance vectors between the owner cell P and it's neighbouring cells N are described with a vector $\mathbf{d_f}$ connecting the cell centres of P and N. The face area vector $\mathbf{S_f}$ is prescribed for each of the cell faces in such a way that the vector is pointing outwards of the cell, has a magnitude equal to the area of the face and is normal to the face.

4.1.2 Discretisation of the Conservation Equation

Finite volume discretisation can be illustrated by first considering a generic scalar $\phi(\mathbf{x}, t)$ conservation equation:

$$\frac{\partial(\rho\phi)}{\partial t} + \nabla \cdot (\rho \mathbf{U}\phi) - \nabla(\Gamma_\phi \nabla\phi) = S_\phi \tag{4.1}$$

In FV fashion the transport equation has to be integrated over each control volume V. The following equation is an integral form of 4.1 after applying integration.

$$\int_t^{t+\Delta t} \left(\frac{\partial}{\partial t} \int_V \rho\phi \, \mathrm{d}V + \int_V \nabla \cdot (\rho \mathbf{U}\phi) \, \mathrm{d}V - \int_V \nabla(\Gamma_\phi \nabla\phi) \, \mathrm{d}V \right) \mathrm{d}t = \int_t^{t+\Delta t} \left(\int_V S_\phi \, \mathrm{d}V \right) \mathrm{d}t \tag{4.2}$$

Spatial discretisation is achieved in two step process: first Gauss' divergence theorem is used to transform volume integrals into surface integrals (Ferziger and Perić [48]), then the surface integrals are approximated as discrete sums and expressions of the variables at the cell faces in terms of the variable cell values. To illustrate this process a generalised formulation for a scalar or a vector quantity ϕ conservation is used:

$$\int_V \nabla \cdot \boldsymbol{\phi} \, \mathrm{d}V = \int_{\delta S} \mathrm{d}\mathbf{S} \cdot \boldsymbol{\phi} \tag{4.3}$$

$$\int_V \nabla\phi \, \mathrm{d}V = \int_{\delta S} \mathrm{d}\mathbf{S}\phi \tag{4.4}$$

$$\int_V \nabla \times \boldsymbol{\phi} \, \mathrm{d}V = \int_{\delta S} \mathrm{d}\mathbf{S} \times \boldsymbol{\phi} \tag{4.5}$$

where $d\mathbf{S}$ is an infinitesimal surface area vector associated with the bounding surface and δS indicates the boundary surfaces of the control volume. Polyhedral control volumes are bounded by sets of flat faces, hence the obtained surface integrals can be transformed into sums of integrals over each boundary face.

$$\int_{\delta S} \mathrm{d}\mathbf{S} \cdot \boldsymbol{\phi} = \sum_{f=1}^{n} \left(\int_{f} \mathrm{d}\mathbf{S} \cdot \boldsymbol{\phi} \right) \approx \sum_{f=1}^{n} \mathbf{S}_f \cdot \boldsymbol{\phi}_f \tag{4.6}$$

$$\int_{\delta S} \mathrm{d}\mathbf{S}\phi = \sum_{f=1}^{n} \left(\int_{f} \mathrm{d}\mathbf{S}\phi \right) \approx \sum_{f=1}^{n} S_f \phi_f \tag{4.7}$$

$$\int_{\delta S} \mathrm{d}\mathbf{S} \times \boldsymbol{\phi} = \sum_{f=1}^{n} \left(\int_{f} \mathrm{d}\mathbf{S} \times \boldsymbol{\phi} \right) \approx \sum_{f=1}^{n} \mathbf{S}_f \times \boldsymbol{\phi}_f \tag{4.8}$$

where f represents the center of the cell face, $\mathbf{S}_f$ is the face area vector normal to the face, n is the total number of the boundary faces and ϕ_f are the face values of the variable ϕ.

4.1.2.1 Convection Term

The convection term in the integral transport Equation 4.2 is discretised by integrating the term over a control volume and applying Gauss' theorem from Equation 4.3 and Equation 4.6:

$$\begin{aligned} \int_{V} \nabla \cdot (\rho \mathbf{U} \phi) \, \mathrm{d}V &= \sum_{f} \mathbf{S}_f \cdot (\rho \mathbf{U} \phi)_f \\ &= \sum_{f} \mathbf{S}_f \cdot (\rho \mathbf{U})_f \phi_f \\ &= \sum_{f} F \phi_f \end{aligned} \tag{4.9}$$

where F represents the mass flux passing a face of the control volume:

$$F = \mathbf{S}_f \cdot (\rho \mathbf{U})_f \tag{4.10}$$

The face center value of ϕ_f is calculated by an appropriate interpolation scheme [66].

4.1.2.2 Diffusion Term

Diffusive terms of the transport equation are treated in the same manner by applying Gauss' theorem:

$$\int_V \nabla \cdot (\rho\Gamma_\phi \nabla\phi) dV = \int_S \mathbf{S} \cdot (\rho\Gamma_\phi \nabla\phi) = \sum_f (\rho\Gamma_\phi)_f \mathbf{S}_f \cdot (\nabla\phi)_f \tag{4.11}$$

For orthogonal meshes diffusive flux can be calculated as follows:

$$\mathbf{S}_f \cdot (\nabla\phi)_f = |\mathbf{S}| \frac{\phi_N - \phi_P}{|\mathbf{d}|}. \tag{4.12}$$

Alternatively, linear interpolation can be use to obtain the value of the gradient at the cell-face:

$$(\nabla\phi)_f = f_x (\nabla\phi)_P + (1 - f_x)(\nabla\phi)_N, \tag{4.13}$$

where cell centred gradient is defined as:

$$(\nabla\phi)_P = \frac{1}{V_P} \sum_f \mathbf{S}\, \phi_f. \tag{4.14}$$

On non-orthogonal meshes a correction has to be introduced in order to avoid the error introduced by the conditions of the mesh. Contributions to the diffusive flux can be split into non-orthogonal and orthogonal components:

$$\mathbf{S} \cdot (\nabla\phi)_f = |\mathbf{\Delta}| (\nabla\phi)_f + \mathbf{k} \cdot (\nabla\phi)_f. \tag{4.15}$$

Vectors $\mathbf{\Delta}$ and $\mathbf{k}$ are determined through special treatment of non-orthogonal conditions (for an in-depth description see Jasak [66]).

4.1.2.3 Source Terms

Most of the flow and transport phenomena problems have source terms appearing in the governing equations. Such terms affect the outcome of the solution as well as the numerical stability of the computations. Source/Sink terms S_ϕ as in Equation 4.1 in OpenFOAM are first linearised as a sum of an implicit and explicit terms:

$$S_\phi(\phi) = \phi S_I + S_E. \tag{4.16}$$

The linearised source can now be integrated over a CV in order to obtain a spatially discretised value:

$$\int_V S_\phi(\phi)\, \mathrm{d}V = S_I V_P \phi_P + S_E V_P \tag{4.17}$$

4.1.2.4 Time Derivative

To examine the discretisation of the temporal term we consider the first term in Equation 4.2. Throughout this thesis, unless explicitly stated, the reader may assume that Euler-Implicit differencing scheme is used. This particular scheme is chosen for the unconditional stability and because only static meshes are used such a scheme is acceptable:

$$\frac{\partial}{\partial t}\int_{V_P}\rho\phi\,\mathrm{d}V=\int_{V_P}\left(\frac{\partial\rho\phi}{\partial t}\right)_P\mathrm{d}V\approx\frac{(\rho_P^{t+\Delta t}\phi_P^{t+\Delta t}-\rho_P^t\phi_P^t)}{\Delta t}V_P \tag{4.18}$$

4.1.2.5 Temporal Discretisation

In the previous sections the spatial discretisation of the generic scalar conservation equation has been covered. To describe temporal discretisation first recall the integral conservation form of Equation 4.1:

$$\int_t^{t+\Delta t}\left(\frac{\partial}{\partial t}\int_V\rho\phi\,\mathrm{d}V+\int_V\nabla\cdot(\rho\mathbf{U}\phi)\,\mathrm{d}V\right)\mathrm{d}t$$
$$=\int_t^{t+\Delta t}\left(\int_V\nabla(\Gamma_\phi\nabla\phi)\,\mathrm{d}V+\int_V S_\phi\,\mathrm{d}V\right)\mathrm{d}t$$

Applying the assumption that the control volume is constant in time and making use of the Equations (4.9), (4.11), (4.17), (4.18), Equation 4.2 can be rewritten in a "semi-discretised" formulation [59]:

$$\int_t^{t+\Delta t}\left(\frac{(\rho_P^{t+\Delta t}\phi_P^{t+\Delta t}-\rho_P^t\phi_P^t)}{\Delta t}V_P+\sum_f F\phi_f\right)\mathrm{d}t$$
$$=\int_t^{t+\Delta t}\left(\sum_F(\rho\Gamma)_f\mathbf{S}_f\cdot(\nabla\phi)_f+S_IV_P\phi_P+S_EV_P\right)\mathrm{d}t \tag{4.19}$$

In order to obtain fully discretised formulation, the time integral treatment has to be considered. In this study the Euler-Implicit discretisation practice is used. For extensive reviews of other discretisation practices the reader is referred to Patankar [109], Moukalled et al. [96].

Euler-Implicit is first order accurate in time, bounded and unconditionally stable discretisation scheme. As discussed by Rusche [119], in order to preserve boundedness the non-orthogonal correction part of the diffusion term has to be treated

explicitly, whereas the other spatial terms in Equation 4.19 are treated implicitly:

$$\phi_P = \phi_P^n \tag{4.20}$$

$$\phi_f = \phi_f^n \tag{4.21}$$

$$\mathbf{S}_f \cdot (\nabla\phi)_f = |\Delta|(\nabla\phi^n)_f + \mathbf{k} \cdot (\nabla\phi^o)_f \tag{4.22}$$

where for conciseness the $\phi^n = \phi(t + \Delta t)$ stand for the new values of ϕ at the time step that equations are solved and $\phi^o = \phi(t)$ are the old values from the previous time step.

The fully discretised transport equation can now be written as follows:

$$\frac{\rho_P^n \phi_P^n - \rho_P^o \phi_P^o}{\Delta t} V_P + \sum_f F\phi_P^n = \sum_f \left(|\Delta|(\nabla\phi^n)_f + \mathbf{k} \cdot (\nabla\phi^o)_f \right) + S_I V_P \phi_P^n + S_E V_P \tag{4.23}$$

4.1.2.6 System of Linear Algebraic Equations

The previous sections covered the procedures used to linearise and discretise the equations of motion which produce linear algebraic equations for each CV in the computational domain. The generic form that such equations would take can be written as:

$$a_P \phi_P^n + \sum_N a_N \phi_N^n = S_u, \tag{4.24}$$

where summation is performed over all neighbouring cells, S_u are the explicit sources and sinks, a_P are the central coefficients and a_N are the neighbouring coefficients. The system of discretised equations can be expressed in matrix notation:

$$[A][\phi] = [S] \tag{4.25}$$

The sparse matrix $[A]$ is constructed in a way that coefficients a_P serve as the diagonal components and a_N as the off diagonal coefficients. The column vector $[\phi]$ contains all the dependent variables and $[S]$ all explicit source terms.

Throughout this study appropriate linear solvers and preconditioners have been used, all of which are available in the OpenFOAM framework. Discussion of these

methods is out of the scope of this thesis, therefore the reader is referred to Ferziger and Perić [48], Jasak [66], Moukalled et al. [96] all of whom provide extensive reviews for these methods.

4.2 Solution algorithm

The industry standard PISO algorithm developed by Issa [64] has been used throughout this thesis to solve the equations of motion and state. The algorithm uses a segregated approach where the equations are solved sequentially by iteration procedure. The PISO algorithm has been specifically developed for the unsteady compressible flows and it couples the velocity and pressure in order to obtain the solution. Detailed descriptions can be found in the text by Ferziger and Perić [48]. A concise summary has been provided by Ubbink [132] and it has been reproduced here:

- **Momentum predictor**: Firstly the momentum conservation equation is solved using a guessed pressure field, which is usually the value of the pressure from the last times step. The new velocity field solution calculated does not satisfy the continuity.
- **Pressure solution**: The predicted velocity field is used to solve the pressure equation which gives rise to a new pressure field. If the pre-defined tolerance requirements are not met, then the solution procedure is reiterated until the tolerances reach the required values.
- **Velocity correction**: From the pressure solution conserved volumetric fluxes are used to explicitly correct the velocity field. The new velocity field in now consistent with the new pressure field.

The last two steps of the algorithm are reiterated until the required tolerances are met. The flowchart of the PISO algorithm is presented in Figure 4.2.

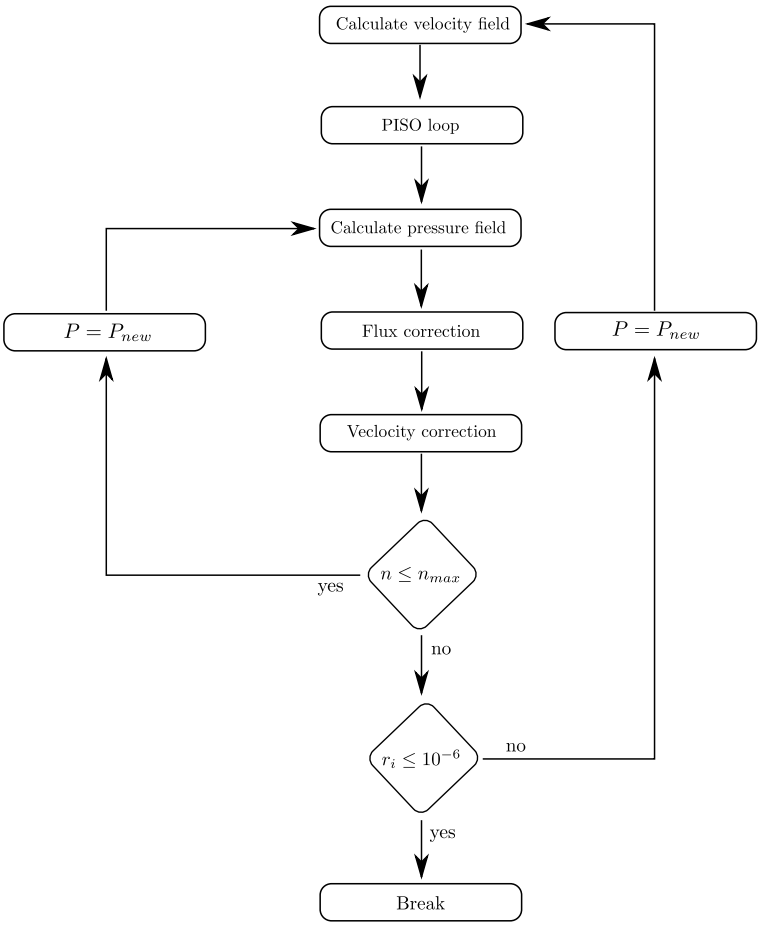

Figure 4.2: Flowchart showing the principles of the PISO algorithm.

4.3 Extended Quadrature Method of Moments

Throughout this section different numerical aspects of the EQMOM methodology are discussed. The present formulation of EQMOM has been initially implemented in the OpenQBMM framework (Passalacqua et al. [106]) and was used throughout this study. The finite volume procedures are used to discretise the moment transport equations, with the addition of the kinetic-based spatial fluxes treatment of the advection term which is required in order to ensure the realizability criteria of the moment set is met [40, 76, 107]. Term by term descriptions are given in order to have a complete description of the discretisation process of the moment conservation equation 3.113.

Further, the algorithm description for the moment realizability and inversion pro-

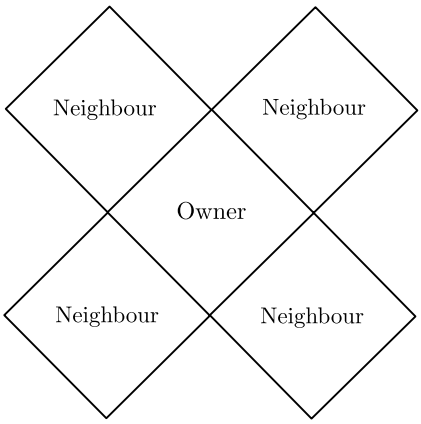

Figure 4.3: Schematic showing a computation cell called owner and its neighbouring cells.

cedure are provided which are crucial parts of the EQMOM approach.

4.3.1 Spatial flux treatment

Moment realisability issues arising during the solution procedure are known and have been discussed in the literature, see Desjardins et al. [40], Wright [139]. There is a consensus that discretisation of the advection term using traditional numerical schemes is not sufficient to have moment realisability maintained. The OpenQBMM framework employs a convection term fluxes calculation procedure proposed by Vikas et al. [133, 134], where fluxes are computed from the quadrature approximation of the moments rather than the interpolation of the moments itself. To let us illustrate the method let's consider an arbitrary set of computational cells on a cartesian grid (Figure 4.3). Using subscripts *own* and *nei* to indicate variable values computed on the owner or neighbour cell side of the face moment contributions to the cell face are written as follows:

$$\mu_{k,\text{own}} = \sum_{\alpha=1}^{N_f} \omega_{\alpha,\text{own}} \xi_{\alpha,\text{own}}^{k} \tag{4.26}$$

$$\mu_{k,\text{nei}} = \sum_{\alpha=1}^{N_f} \omega_{\alpha,\text{own}} \xi_{\alpha,\text{nei}}^{k} \tag{4.27}$$

where ω and ξ are the quadrature weights and abscissae respectively. Assuming that velocity vector $\mathbf{U}$ values are known at the cell centres, then the convective

flux of the moments can be computed as follows:

$$\varphi_{\mu_k} = \mu_{k,\text{nei}} \min(\mathbf{U}_{\text{nei}} \cdot \mathbf{S}_f, 0) + \mu_{k,\text{own}} \max(\mathbf{U}_{\text{own}} \cdot \mathbf{S}_f, 0) \tag{4.28}$$

where $\mathbf{U}_{\text{nei}}$ and $\mathbf{U}_{\text{own}}$ are the velocity vector contributions to the cell face from the neighbour and owner cells respectively; $\mathbf{S}_f$ are the surface normal vectors.

4.3.2 Diffusion term treatment

Vikas et al. [134] investigated diffusion terms and came to the following conclusions:

- Size-independent diffusion cases do not present additional problems when conventional second-order discretisation schemes are used;
- Size-dependent cases require the diffusion term to be treated as an explicit source and computed using quadrature approximation.

Unless otherwise stated throughout this study size-independent diffusion models are used, hence the diffusion term in the moment transport equations are discretised using the second-order scheme.

4.3.3 Source terms treatment

Trivial explicit treatment of the source terms for nucleation, growth, aggregation and breakage processes is known to lead to significant restrictions on the global simulation time-step [107]. The OpenQBMM framework employs a multi-step adaptive scheme by Nguyen et al. [98]. Moment realizability is ensured due to the fact that one can use explicit Euler methods assuming the time-steps are small enough. It is not the main focus of the current work, therefore the reader is directed to the paper by Nguyen et al. [98] for more details.

4.3.4 Moment space and realizability

From the first look the moment equations defined in Section 3.4.4 appear to be uncoupled from one another. To illustrate that this is not the case one just needs

to recall the definition of a moment transport in terms of an NDF as described in equation 3.113:

$$\mu_k(\mathbf{x}, t) = \int_0^{+\infty} n(\xi, \mathbf{x}, t)\xi^k \, \mathrm{d}\xi$$

Even though the moment transport equations are independent from each other the set of moments is derived from the same NDF, therefore they cannot be independent as they first seem to be.

Using the formalism of set theory the space $\mathcal{P}$ of finite positive Borel measures on positive support $[0, +\infty)$ is defined. The vector of moments of orders 0 to N is defined as follows:

$$\mathbf{M}_N(\mu) = \begin{bmatrix} \mu_0(\mu) \\ \mu_1(\mu) \\ \dots \\ \mu_N(\mu) \end{bmatrix}, \qquad \mu_k(\mu) = \int_0^{+\infty} \xi^k \, \mathrm{d}\mu(\xi) \tag{4.29}$$

where the Borel measure $\mu \in \mathcal{P}$ and it is assumed that such moments are finite.

Definition 4.3.1. The Nth-moment space $\mathcal{M}_N(0, \infty)$ is defined by

$$\mathcal{M}_N = \{\mathbf{M}_N(\mu) \quad | \quad \mu \in \mathcal{P}\}$$

As described by Chalons et al. [27] the task of a numerical solution method such as EQMOM is to find a continuous approximation $n^a \geq 0$ for the NDF $n(\xi, \mathbf{s}, t)$:

$$\mu_k \approx \mu_k^a = \int_0^{+\infty} n^a(\xi)\xi^k \, \mathrm{d}\xi \quad \text{for } k \in \{0, ..., 2N\} \tag{4.30}$$

An approximation n^a can only be found if $\mathbf{M}_N$ is in the moment space. The moment vector belonging to the moment space is said to be *realizable* and if the vector belongs to the interior of the moment space then it is said to be *strictly realizable*.

Therefore the requirement for the moment vector to be strictly realizable is needed in order to ensure physicality of the numerical solution. In order to determine whether a moment vector is realizable or not we start by noting that the moment

space is convex and can be characterised by the Hankel determinants [51, 98]. Hankel determinant for the moments μ_r is defined as:

$$\mathcal{H}_{2n+d} = \det \mathbf{H}_{2n+d}, \qquad \mathbf{H}_{2n+d} = \begin{bmatrix} \mu_0 & \cdots & \mu_{n+d} \\ \vdots & \ddots & \vdots \\ \mu_{n+d} & \cdots & \mu_{2n+d} \end{bmatrix}, \qquad n \in \mathbb{N};\ d \in \{0, 1\} \tag{4.31}$$

Laurent and Nguyen [74] provides a theorem:

Theorem 1. The moment vector $\mathbf{M}_N = (\mu_0, \mu_1, ..., \mu_N)^T$ is strictly realizable iff $\mathcal{H}_k > 0, \quad k \in \{0, 1, ..., N\}$ and, if it belongs to the boundary of the moment space, there exists $k \leq N$ such that $\mathcal{H}_0 > 0, ..., \mathcal{H}_{k-1} > 0, \mathcal{H}_k = 0, ..., \mathcal{H}_N = 0$

As one might know computation of determinants is not efficient and even with the most powerful hardware it would still mean that the algorithm is not viable for any real life problems. Fortunately, orthogonal polynomials theory (Gautschi [51]) can be used to derive quantities that can provide necessary information about the moment set realisability.

4.3.5 Realizability criteria using orthogonal polynomials

Let us consider a real polynomials space $\mathbb{P}$ and a pair of polynomials $p, q \in \mathbb{P}$. The inner product is then defined as:

$$(p, q) = \int_{\mathbb{R}} p(x)q(x)\,\mathrm{d}\mu \tag{4.32}$$

where $\mathrm{d}\mu$ is a positive finite Borel measure.

Also consider a sequence of polynomials $\{P_k\}_{i\in\mathbb{N}}$, such that iff:

$$\int_0^\infty P_k(x)P_l(x)\,\mathrm{d}\mu(x) = 0$$

for $k \neq l$, then P_k has an exact degree k and is orthogonal for some positive measure $\mathrm{d}\mu$ on the $[0; \infty)$ support. Such sequence satisfies a recurrence relationship (Gautschi [51]):

$$P_{k+1}(X) = (X - a_{k-1})P_k(X) - b_{k+1}P_{k-1}(X), \qquad k \in \mathbb{N} \tag{4.33}$$

with $b_{k+1} > 0$, $P_{-1}(X) = 0$, $P_0(X) = 1$. Conversely, it can be demonstrated that for a sequence satisfying Equation 4.33 the measure $\mathrm{d}\mu$ has $[0; \infty)$ support if a sequence of positive numbers $\{\zeta_n\}_n \in \mathbb{N}^*$ exists. Such a sequence would satisfy the following:

$$b_k = \zeta_{2k-1}\zeta_{2k}, \quad a_k = \zeta_{2k} + \zeta_{2k+1}, \text{ for } k \geq 1 \tag{4.34}$$

and

$$\zeta_k = \frac{\mathcal{H}_k \mathcal{H}_{k-3}}{\mathcal{H}_{k-1}\mathcal{H}_{k-2}} \tag{4.35}$$

where $\mathcal{H}_k = 0$ for $k \leq 0$.

Using ζ_k an alternative criteria for realizability can be established which is more computationally efficient. Nguyen et al. [98] provides the criteria for realizability that is based on the ζ_k polynomials:

Proposition 1. (Realizability) Let's consider a moment vector $\mathbf{M}_N$, moment space $\mathcal{M}_N = \{\mathbf{M}_n(\mu) | \mu \in \mathcal{P}\}$ and the corresponding set of polynomials $(\zeta_k)_{k=1,...,N}$, then $\mathbf{M}_N \in Int(\mathcal{M}_N) \iff \zeta_k > 0$ for $k = 1, ..., N$.
When the moment vector belongs to the boundary of the space $\mathbf{M}_n \in \partial\mathcal{M}_N$, then there exists $\mathcal{N}(\mathbf{M}_N) = n$, such that $\zeta_k > 0$ for $k = 1, ..., n-1$ and $\zeta_n = 0$.

Recurrence coefficients $a_k\, b_k$ and the polynomials ζ_k can be computed from the moments using a variation of a Chebyshev algorithm that was adapted by Wheeler [138]. There have been alternative algorithms proposed, such as Gordon's Product-Difference algorithm [52, 53], Rutishauser's Quotient-Difference algorithm [88, 120]. Due to slightly better stability the ζ-Chebyshev algorithm (a coupling of the Chebyshev algorithm with calculation of ζ_k) [138] has been chosen for EQMOM procedures [98] and it has been used in OpenQBMM framework [106, 107].

4.3.6 Moment inversion procedure

The aim of the moment inversion procedure is to numerically find appropriate primary quadrature weights ω_α, abscissae ξ_α, and the KDF parameter σ. Recall the NDF approximation provided in Equation 3.123 and the log-normal kernel

density function Equation 3.125:

$$n(\xi) \approx p_N(\xi) = \sum_{\alpha=1}^{N} \omega_\alpha \delta_\sigma(\xi, \xi_\alpha)$$
$$\delta_\sigma(\xi, \xi_\alpha) = \frac{1}{\xi\sigma\sqrt{2\pi}} \mathrm{e}^{-\frac{(\ln \xi - \xi_\alpha)^2}{2\sigma^2}}$$

The original EQMOM algorithm has been proposed by Yuan et al. [149]. Unfortunately the original algorithm had a couple of issues:

- It did not deal with the boundary of the moment space and with the transitions between boundary;
- The computation algorithm for σ was suboptimal.

Both these issues have been addressed by Nguyen et al. [98] and the improved algorithm has been implemented in the OpenQBMM framework which is used in this thesis.

Before explaining the procedure we can summarise the principle steps of the EQMOM reconstruction procedure which can be summarised as follows:

1. Use the ζ-Chebyshev algorithm to numerically compute the number of realizable moments from the transported moments set;
2. Use Ridder's method [111] to compute optimal value of σ for the interval $(0, \sigma^2_{\max})$, if needed Brent's method [111] is used to minimize the target function $J_{2N}(\sigma)^2$ (equation 4.40) and find σ;
3. From Equation 4.37 use quadrature algorithm to compute the weights and abscissas.

Figure 4.4 presents these key steps of the algorithm, for more more detailed descriptions see Nguyen et al. [98], Passalacqua et al. [107].

We first start by first introducing new variable $\mathbf{M}^*_k$ and a linear transformation

between the transported moment vector and the starred moment vector as follows:

$$\mathbf{M}_k^* = \sum_{\alpha=1}^{N} \omega_\alpha \xi_\alpha^k \tag{4.36}$$

$$\mathbf{M}_k = \mathbf{A}_k(\sigma)\mathbf{M}_k^* \tag{4.37}$$

The linear transformation matrix $A_k(\sigma)$ is diagonal, invertible and the purpose of it is to allow one to use the Chebyshev algorithm and determine the number of realizable moments $\mathcal{N}(\mathbf{M}_{2N})$. For log-normal KDF the elements of equation 4.37 are written as:

$$\mu_k = \mu_k^* \mathrm{e}^{-k^2\sigma^2/2} \tag{4.38}$$

To find out an appropriate value of the KDF parameter σ first of all an initial guess region is set as $I_0 = [0, \sigma_{\max,N}]$ and a helper function $\overline{M}_{2N}$ is defined. For a value of σ there are two possibilities:

1. $\mathbf{M}_{2N-1}^* \in Int(\mathcal{M}_{2N-1})$ which corresponds to $\sigma < \sigma_{\max,2N}$;
2. $\mathbf{M}_{2N-1}^* \notin Int(\mathcal{M}_{2N-1})$ which corresponds to $\sigma \geq \sigma_{\max,2N}$.

In the first case the corresponding weights and abscissas $(\omega(\sigma); \xi(\sigma))_{\alpha=1,\ldots,N}$ are computed and the helper function is set to $\overline{M}_{2N}(\sigma) = (0, ..., 0, 1)A_{2N}(\sigma)\mathbf{M}_{2N}^*(\sigma)$. In case two the value for the helper function $\overline{M}_{2N}$ is set to a large number L and in OpenFOAM framework it corresponds to 1.0×10^{16}. The target function can now be written as a piecewise function:

$$\overline{M}_{2N}(\sigma) = \begin{cases} \sum_{\alpha=1}^{N} \omega_\alpha(\sigma)\xi_\alpha(\sigma)^{2N} e^{(2N)^2\sigma^2/2} & \sigma < \sigma_{\max,2N} \\ L & \sigma \geq \sigma_{\max,2N} \end{cases} \tag{4.39}$$

Using the helper function a target function J_{2N} is defined as:

$$J_{2N}(\sigma) = \frac{\mu_{2N} - \overline{M}_{2N}(\sigma)}{\mu_{2N}} \tag{4.40}$$

Roots of this target function correspond to the values of σ. If the roots can be found and they correspond to a solution that preserves the moment set then that value of σ is used, if not then Brent's method is used [111] on $J_{2N}(\sigma)^2$ that finds the value of σ by minimising the distance of $J_{2N}(\sigma)$ from zero.

Finally with the σ value obtained the quadrature algorithm can be used to find the weights and abscissas from:

$$\mathbf{M}^*_{2N-1}(\sigma) = \mathbf{A}_{2N-1}(\sigma)^{-1}\mathbf{M}_{2N-1}. \tag{4.41}$$

A simplified summary of the reconstruction procedure is presented in Figure 4.4.

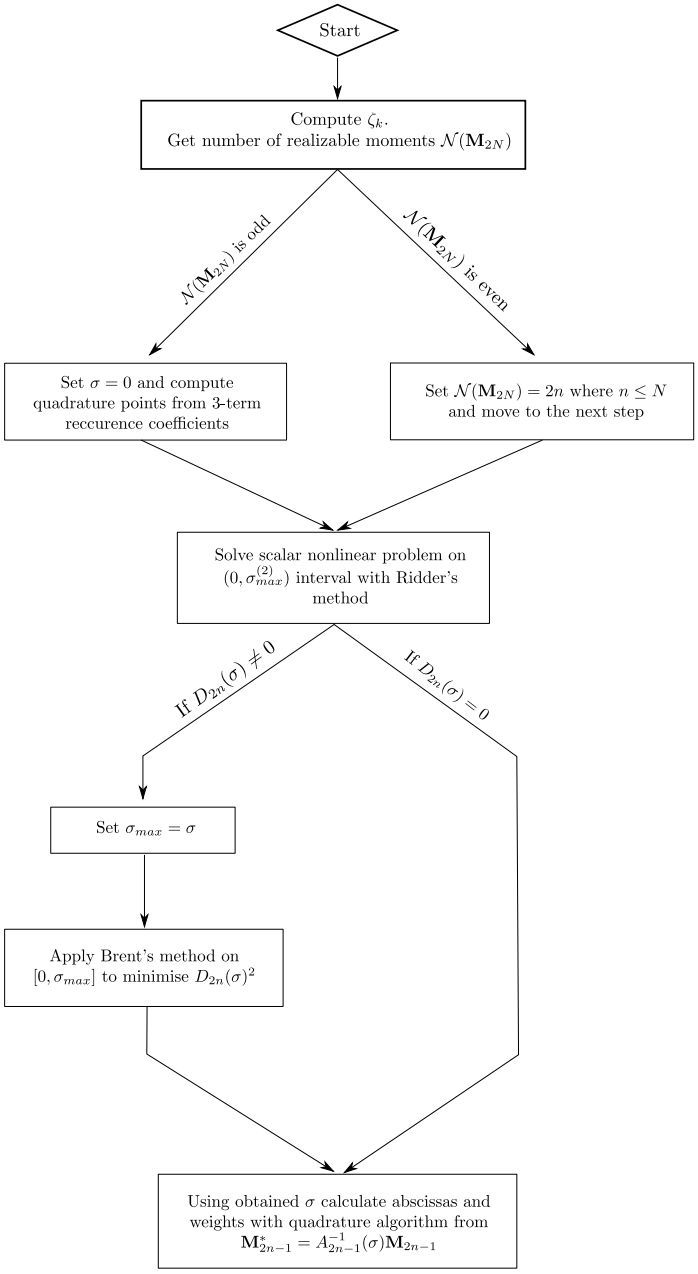

Figure 4.4: Global procedure for moment reconstruction [98]

4.4 Summary of the framework structure and solution algorithm

Framework structure

Recalling the material presented in Chapter 3, a complete model of precipitation requires three key pilars to be incorporated: a) hydrodynamics; b) chemical species transport; c) CSD evolution.

Newly written solver was named *mapFoam* and was adapted from an already existing solver in OpenFOAM framework - *driftFluxFoam* - which models hydrodynamics of the fluid with drift flux mixture model formulation. Chemical species transport were added to the solver package in order to capture the levels of supersaturation in the system. Finally the population balance modelling was achieved using OpenQBMM libraries [105] that handles solution algorithms for transport of the statistical moments of CSDs. Specific kinetic models used throughout this thesis were added to the solver separately.

Figure 4.5 provides a summary of interlinking between each building block of the solver.

Solution algorithm

The solution procedure involving all key components can now be summarised. The solution algorithm starts by first calculating the mixture velocity U_m and pressure P fields using the PISO algorithm described previously in this Chapter. The values for mixture velocity U_m and pressure P are then used to transport the dispersed phase volume fraction field α_d and the reactant species fields Y_i. The procedure is then followed by calculation of the relevant supersaturation indicator and the value is then fed to the population balance model formulation. The moments μ_k are then transported using the mixture velocity and the supersaturation values.

Finally the EQMOM moment reconstruction algorithm is performed to check whether

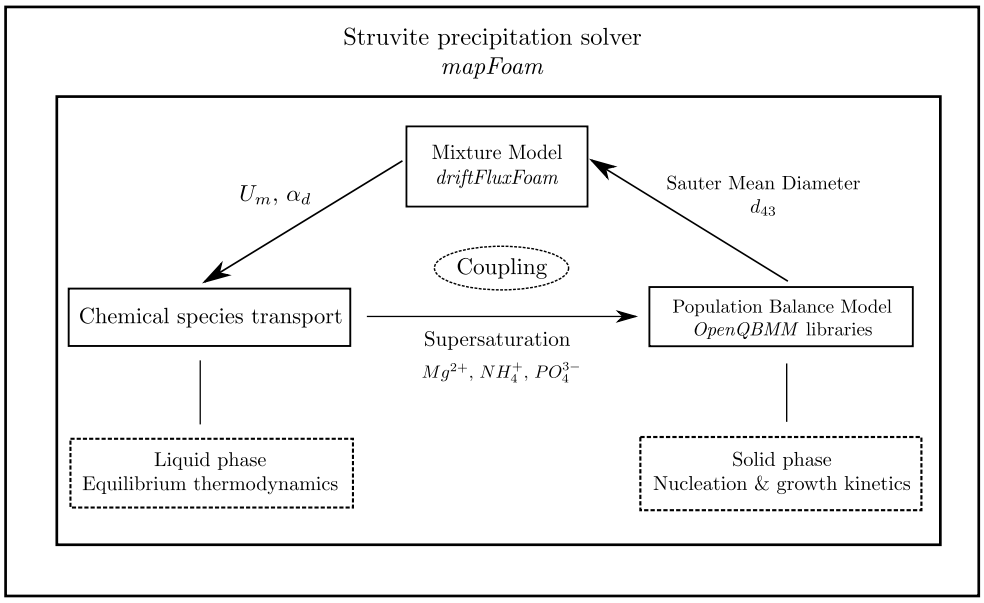

Figure 4.5: *mapFoam* solver structure

the moment set follows the realizability condition. If the condition is met then the Saueter Mean Diameter d_{43} value is calculated and returned to the drift flux model for the following time step. Figure 4.6 summarises these key steps of the procedure.

Code repository

The solver with all of it's components and documentation can be found on and online repository, see Appendix C for more details.

4.5 Closure

Throughout this chapter the key aspects on the numerical procedures of the finite volume discretisation and the population balance solution methods were discusses. Discretisation of the convective, diffusive, temporal and the source terms and the computational domain were presented which all follow the FV methodology. Key points have been made with respect to the spatial flux treatment of the moment transport equation which were done using the kinetic-based flux treatment.

In addition the specifics of the moment realizability and inversion procedures in the EQMOM formulation have been discussed. The importance of these procedures

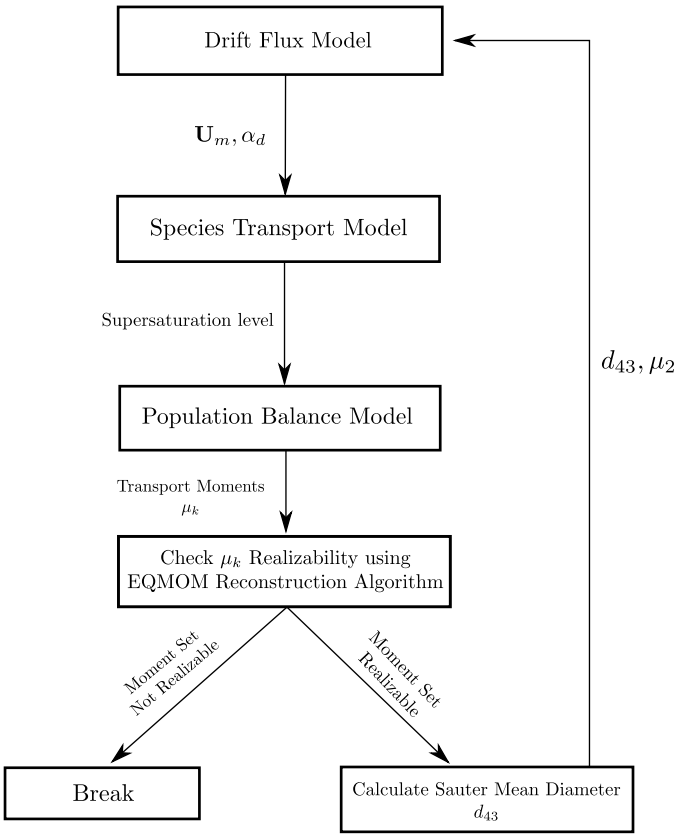

Figure 4.6: Flowchart showing solver solution procedure.

arise due to the fact that the transported moments have to be representative of a physical number density function therefore great care has to be taken in order to ensure that the solution of the moment transport equation is correct.

The validity of the solver performance is discussed in the following chapters, where the one-dimensional cases are used to verify the solutions against semi analytical results obtained from a MATLAB code. In addition, two and three dimensional cases are presented in Chapter 6.

Chapter 5

Precipitation kinetics studies

A verification study of different kinetic mechanisms is presented in this chapter. As discussed in Section 3.3.3 multiple different mechanisms were considered. Precipitation kinetic mechanisms are highly dependent on the experimental setup, therefore different authors provide slightly different formulations. Due to the lack of knowledge on the specific rates of the kinetic mechanisms in HDVS, multiple different proposed empirical models of nucleation and growth found in the literature were implemented. One-dimensional CFD cases were verified against semi-analytical solutions obtained using scripts written in MATLAB.

Additionally a comparison study was performed to investigate the significance and the effect that solution non-ideality and speciation has on the rate of precipitation. Chemical conversion times were calculated to get a quantitative value for the time it takes precipitation processes to occur using the specific kinetic model.

5.1 Solver comparison against MATLAB solutions

It has been explained in Chapter 2 that the availability as well as the applicability of various precipitation kinetic models is lacking or the models available would only be applicable to the systems for which the constants have been fitted. Similarly in Chapter 3 various possible formulations of the kinetic models have been covered, where the difference between mathematical formulations occurs in terms of what parameter is used to track the level of supersaturation in the system. Based on the available literature three models following different formulations have been chosen for this study.

5.1.1 CFD Case setup for comparison

Single computation cell case was used to obtain data for comparison against the semi-analytical solutions. Initial conditions where set appropriately so that no velocity field was present, therefore the solver effectively would solve the following reduced equations for the scalar species and moment transport:

$$\frac{\partial(Y_i)}{\partial t} = \pm\phi_v\rho_d\left(\frac{W_i}{W_d}\right)G\frac{\partial\mu_3}{\partial t} \tag{5.1}$$

$$\frac{\partial\mu_k(\mathbf{x},t)}{\partial t} + G_k(\mathbf{x},t) = 0^k J(\mathbf{x},t) \tag{5.2}$$

The volume fraction field sources term was removed for these cases as these were not needed to obtain relevant information about solver performance.

Those readers willing to replicate the study are directed to an online repository given in Appendix C, where all sets of verification cases have been uploaded.

5.1.2 Investigated kinetic models

Galbraith

Galbraith et al. [50] performed parameter estimation from sets of experimental

data. The authors assumed that nucleation, growth and aggregation kinetic models follow power law rules with respect to the saturation index of the solution. Equations 5.3, 5.4, 5.5 and Table 5.1 present these kinetic laws and their respective rate parameters.

$$J = C_J(S_I)^{N_j} \tag{5.3}$$

$$G = C_G(S_I)^{N_g} \tag{5.4}$$

$$\beta = k_\beta(S_I)^{N_\beta} \tag{5.5}$$

Table 5.1: Kinetic rates estimated by Galbraith et al. [50]

Mechanism	Rate coefficient C_i	Rate order N_i
J $(m^{-3}s^{-1})$	1.417×10^{9}	1.68
G (m/s)	2.0817×10^{-6}	5.062
β (m^3/s)	6.2017×10^{-6}	5.259

Hanhoun

Hanhoun et al. [55] proposed kinetic mechanisms for nucleation and growth. The nucleation kinetic mechanism is based on classical nucleation theory and the growth mechanism is formulated as a size independent power law with respect to the absolute supersaturation of the solution. Rate expressions for nucleation and growth respectively are as follows:

$$J = A \exp\left(-\frac{B}{\ln^2 \Omega}\right) \tag{5.6}$$

$$G = C_g S^{N_g} \tag{5.7}$$

Ye

Ye et al. [144] proposed using a combination of the previously mentioned kinetic models. The authors used the nucleation kinetics model proposed by Galbraith

Table 5.2: Nucleation and growth kinetic rates estimated by Hanhoun et al. [55]

Rate coefficients	Homogeneous	Heterogeneous
A $(m^{-3}s^{-1})$	$10^{9.6}$	$10^{7.47}$
B	449	0.6
C_g (m/s)	$10^{-5.33}$	$10^{-5.33}$
N_g	1.34	1.34

et al. [50] and the growth kinetic model presented by Hanhoun et al. [55]; therefore an additional comparison against a semi-analytical solution has been performed.

$$J = C_J(S_I)^{N_j} \tag{5.8}$$

$$G = C_g S^{N_g} \tag{5.9}$$

Table 5.3: Kinetic rates used by Ye et al. [144]

Mechanism	Rate coefficient C_i	Rate order N_i
J $(m^{-3}s^{-1})$	1.417×10^9	1.68
G (m/s)	$10^{-5.33}$	1.34

5.1.3 Semi-analytical ODEs

Fourth order ODEs are derived for one dimensional cases encapsulating nucleation and growth mechanisms provided above. The derived equations representing the change in time of a concentration for the reactant species are still too complex to be solved analytically, therefore they are solved using MATLAB scripts. Full derivations are provided in Appendix A.

Galbraith kinetics

The ordinary differential equation representing reactant evolution in time compris-

ing nucleation and growth kinetics provided by Galbraith is as follows:

$$\frac{\mathrm{d}^4C}{\mathrm{d}t^4} = \frac{A_1}{C^3}\left(\frac{\mathrm{d}C}{\mathrm{d}t}\right)^4 + \frac{A_2}{C}\left(\frac{\mathrm{d}C}{\mathrm{d}t}\right)\left(\frac{\mathrm{d}^3C}{\mathrm{d}t^3}\right) - \frac{A_3}{C^2}\left(\frac{\mathrm{d}C}{\mathrm{d}t}\right)^2\left(\frac{\mathrm{d}^2C}{\mathrm{d}t^2}\right) + \frac{A_4}{C}\left(\frac{\mathrm{d}^2C}{\mathrm{d}t^2}\right)^2 - A_5 \tag{5.10}$$

where the prefactor constants are defined as follows:

$$A_1 = \left(\frac{6N_g}{\ln 10}\right)\frac{1}{S_I} + \left(\frac{9N_g(7N_g+3)}{\ln^2 10}\right)\frac{1}{S_I^2} + \left(\frac{27N_g(2N_g+1)(3N_g+2}{\ln^3 10}\right)\frac{1}{S_I^3}$$

$$A_2 = \left(\frac{21N_g}{\ln 10}\right)\frac{1}{S_I}$$

$$A_3 = \left(\frac{21N_g}{\ln 10}\right)\frac{1}{S_I} + \left(\frac{9N_g(18N_g+7)}{\ln^2 10}\right)\frac{1}{S_I^2}$$

$$A_4 = \left(\frac{12N_g}{\ln 10}\right)\frac{1}{S_I}$$

$$A_5 = 6k_v\left(\frac{\rho_d}{W_d}\right)C_G^3 C_J S_I^{3N_g+N_j}$$

Hanhoun kinetics

The ordinary differential equation representing reactant evolution in time comprising nucleation and growth kinetics provided by Galbraith et al. [50] is as follows:

$$\frac{\mathrm{d}^4C}{\mathrm{d}t^4} = A_1\left(\frac{\mathrm{d}C}{\mathrm{d}t}\right)^4 + A_2\left(\frac{\mathrm{d}C}{\mathrm{d}t}\right)\left(\frac{\mathrm{d}^3C}{\mathrm{d}t^3}\right) - A_3\left(\frac{\mathrm{d}C}{\mathrm{d}t}\right)^2\left(\frac{\mathrm{d}^2C}{\mathrm{d}t^2}\right) + A_4\left(\frac{\mathrm{d}^2C}{\mathrm{d}t^2}\right)^2 - A5); \tag{5.11}$$

where the prefactor constants are as follows:

$$A_1 = \frac{N_g(2N_g+1)(3N_g+2)}{S^3}$$

$$A_2 = \frac{7N_g}{S}$$

$$A_3 = \frac{N_g(18N_g+8)}{S^2}$$

$$A_4 = \frac{4N_g}{S}$$

$$A_5 = 6k_v C_g^3 A\left(\frac{\rho_d}{W_d}\right)S_I^{3N_g}\exp\left(-\frac{B}{\ln^2(\Omega)}\right)$$

Ye kinetics

The ordinary differential equation representing reactant evolution in time compris-

ing nucleation and growth kinetics provided by Ye et al. [144] is as follows:

$$\frac{\mathrm{d}^4C}{\mathrm{d}t^4} = A_1\left(\frac{\mathrm{d}C}{\mathrm{d}t}\right)^4 + A_2\left(\frac{\mathrm{d}C}{\mathrm{d}t}\right)\left(\frac{\mathrm{d}^3C}{\mathrm{d}t^3}\right) - A_3\left(\frac{\mathrm{d}C}{\mathrm{d}t}\right)^2\left(\frac{\mathrm{d}^2C}{\mathrm{d}t^2}\right) + A_4\left(\frac{\mathrm{d}^2C}{\mathrm{d}t^2}\right)^2 - A_5 \tag{5.12}$$

$$A_1 = \frac{N_g\gamma^3(2N_g+1)(3N_g+2)}{S^3}; \tag{5.13}$$

$$A_2 = \frac{7N_g\gamma}{S}; \tag{5.14}$$

$$A_3 = \frac{N_g\gamma^2(18N_g+7)}{S^2}; \tag{5.15}$$

$$A_4 = \frac{4N_g\gamma}{S}; \tag{5.16}$$

$$A_5 = (k_v C_g^3 C_j)\frac{\rho_d}{W_d}S^{3N_g}S_I^{N_j}. \tag{5.17}$$

5.1.4 Comparison Results

A single-cell case with no flow field was prepared for CFD simulations. The reactant initial concentration in all of the kinetic model cases was set to $C = 0.04M$ and the simulations were run until an equilibrium concentration regimes were reached. Comparisons between MATLAB and OpenFOAM solutions for Galbraith, Hanhoun and Ye kinetics cases are presented in Figure 5.1.

All three cases show acceptable qualitative agreement with the semi-analytical solutions. The observed differences between the solutions are attributed to numerical errors. Error values are small and the qualitative behaviour is retained, therefore it is believed that the precipitation kinetics part of the CFD solver is performing correctly and giving appropriate results.

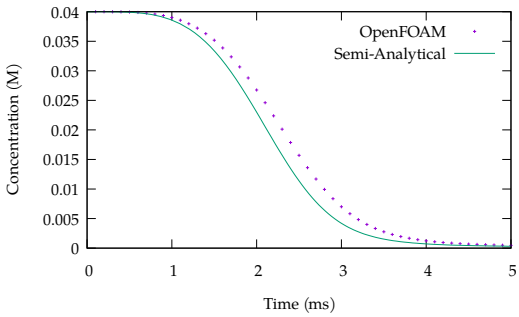

(a) Galbraith kinetics

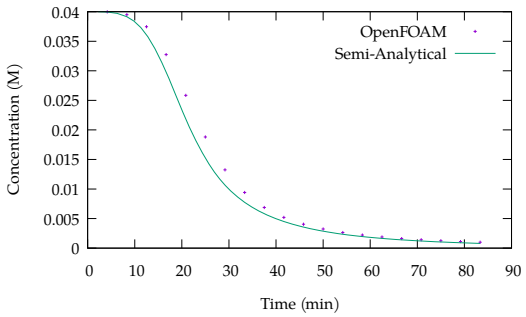

(b) Hanhoun kinetics

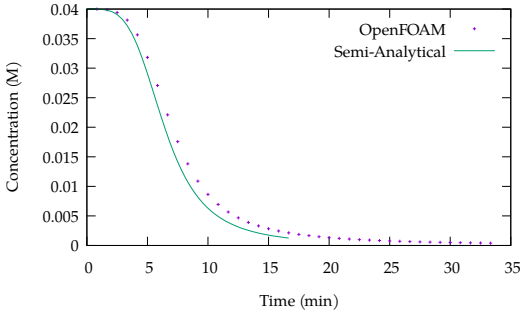

(c) Ye kinetics

Figure 5.1: Comparison of the concentration evolution over time between OpenFOAM solutions and the semi-analytical solutions.

Discussion on reaction time differences

Large differences in reaction times have been observed between different studies of precipitation kinetic models. Galbraith kinetic models (Equations 5.3, 5.4) displayed the fastest reaction process with reactant concentrations depleted within seconds of flow time. Hanhoun models (Equations 5.6, 5.7) showed the slowest precipitation process rates which were up to 16 hours until the reactants were depleted. Ye kinetic models (Equations 5.8, 5.9) were comparatively similar to Hanhoun models. A few orders of magnitude differences in reaction process times observed using different kinetic models have to be addressed before moving forward. Our focus will be directed to Galbraith and Hanhoun kinetic model formulations. Ye kinetic models are a combination of Galbraith nucleation 5.3 and Hanhoun growth 5.7, therefore any insights gained will be applicable to Ye kinetics formulation.

First of all one of the primary differences between Equations 5.3, 5.4 and Equations 5.6, 5.7 is that the former set of equations employs saturation index (Equation 3.90) whereas the latter uses superaturation ratio (Equation 3.87) and absolute saturation (Equation 3.89) as indicators for the level of saturation in the system. In order to compare the mathematical trends between each of the formulations Hanhoun model can be rewritten in terms of saturation index SI as follows:

$$J = A \exp\left(- \frac{9B}{SI^2 \ln^2 10} \right) \tag{5.18}$$

$$G = C_g \left(10^{SI/3} - 1\right) K_{sp}^{1/3} \Big)^{N_g} \tag{5.19}$$

Both Galbraith and Hanhoun kinetic models can now be compared by plotting nucleation and growth kinetic models with respect to saturation index SI parameter. Figure 5.2a displays the variations nucleation kinetic models, whereas Figure 5.2b shows the variations of the growth kinetic models.

From the comparison figures it is visible that both kinetic models given by Galbraith (Equations 5.3, 5.4) are few orders of magnitude faster than Hanhoun kinetic models for nucleation and growth. Nucleation kinetic models dependency with respect

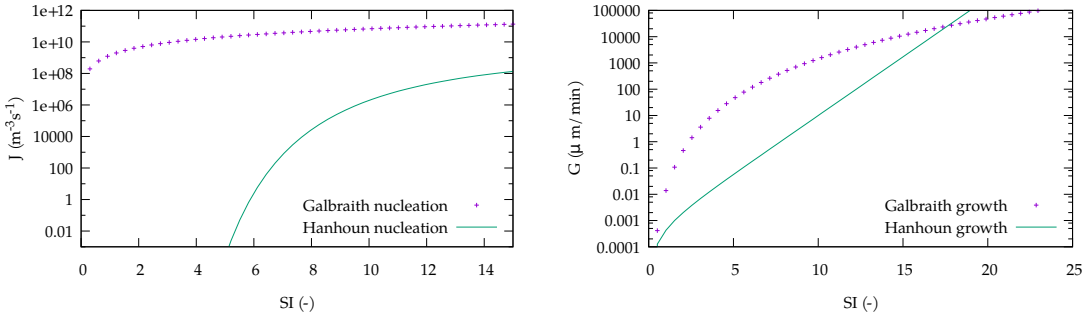

(a) Nucleation kinetics comparison

(b) Growth kinetics comparison

Figure 5.2: Comparison plots between nucleation J and growth G kinetic models with respect to saturation index SI.

to the saturation index SI displayed in Figure 5.2a shows that Galbraith kinetic model acts instantaneously even at low saturation indices, whereas Hanhoun model has a threshold value of $SI \approx 5$ before any levels of nucleation are observed. The expectation is that particle nuclei will start forming when $SI > 0$ as this indicate supersaturation condition in the system. The Galbraith kinetic models predict large numbers of nuclei forming as soon as the supersaturation is reached in the system, whereas the Hanhoun kinetic model requires saturation levels to be ≈ 50 times above the struvite solubility product K_{sp}. Instantaneous nature of Galbraith nucleation model can be interpreted as an overprediction of the physical nature of the process, equally Hanhoun nucleation model poses a requirement of large levels of saturation in the system in order for the particulate matter to start appearing. Due to the fact that the framework is aimed to model spontaneous precipitation of struvite Galbraith nucleation kinetic models is deemed to predict the process better and therefore was used for the test cases presented in Chapter 6. Experimental study of the nucleation rates of struvite was not part of the aims and objectives of this research project therefore this is left as a future work that needs to be done.

The growth kinetic models with respect to the saturation index are preseted in Figure 5.2b. Similarly as it was observed before, the Galbraith kinetic model (Equation 5.4) displays a few orders of magnitude larger particulate growth as opposed to the Hanhoun growth kinetic model (Equation 5.19). This is true for

saturation index values $SI < 17.5$ after which Hanhoun model displays larger growth rate values. It also has to be noted that Galbraith growth model shows an assymptotic behaviour with respect to the saturation level in the system. This assymptotic behaviour is deemed to be more realistic to the process observed in full scale reactor systems and therefore it was decided that the Galbraith growth model will be used for test cases presented in Chapter 6.

5.2 Non-ideality and speciation effects comparison

This section provides a comparison study performed to investigate the significance and the effect that solution non-ideality and speciation has on the rate of precipitation. It is important to understand whether the effects are significant or not because not including appropriate physics can lead to misrepresentative results.

Solution non-ideality and speciation described in Chapter 3 has been implemented into the CFD solver. Ionic activity coefficients γ are calculated using the modified Davies equation.

$$\ln(\gamma_i) = A_{DH} Z_i^2 \left(\frac{\sqrt{I}}{1+\sqrt{I}} - 0.3I \right)$$

where the Debye-Hückel constant is chosen as $A_{DH} = 0.509$ which is a known value at 25°. The pH level in all of the cases has been set as 9.6, however this value has been chosen arbitrarily.

For the cases where ionic speciation was considered the amounts of Mg^{2+}, NH_4^+, PO_4^{3-} were calculated from the total concentrations of C_{Mg}^T, C_N^T and C_P^T using speciation relationships described in Section 3.3.2:

$$\begin{aligned}
C_P^T &= [\mathrm{H_3PO_4}] + [\mathrm{H_2PO_3^-}] + [\mathrm{HPO_4^{2-}}] + [\mathrm{PO_4^{3-}}] \\
&\quad + [\mathrm{MgH_2PO_4^+}] + [\mathrm{MgHPO_4}] + [\mathrm{MgPO_4^-}] \\
C_{Mg}^T &= [\mathrm{Mg^{2+}}] + [\mathrm{MgOH^+}] + [\mathrm{MgH_2PO_4^+}] + [\mathrm{MgHPO_4}] + [\mathrm{MgPO_4^-}] \\
C_N^T &= [\mathrm{NH_3}] + [\mathrm{NH_4^+}]
\end{aligned}$$

Irrespective of the kinetics used the naming chosen for the four case is presented in Table 5.4. Qualitative comparisons between the four cases where the solution is considered to be ideal ($\gamma = 1 = \text{const}$), non-ideal ($\gamma = \text{non-const}$), ideal with speciation and non-ideal with speciation are presented in Figure 5.3.

Table 5.4: Case names for non-ideality and speciation study

Case Name	γ_i	Speciation
1a	$\gamma_i = \text{const} = 1$	No
1b	Varying $\gamma_i = \text{non-const}$	No
2a	$\gamma_i = \text{const} = 1$	Yes
2b	Varying $\gamma_i = \text{non-const}$	Yes

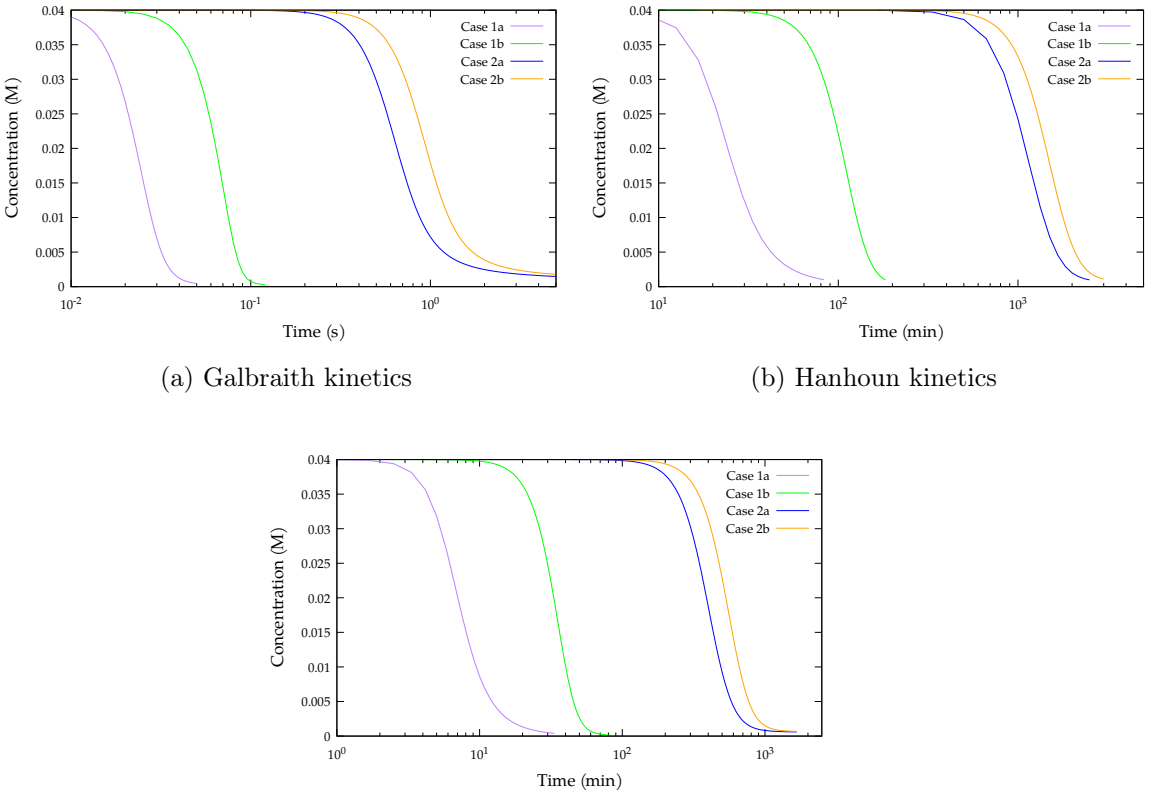

(a) Galbraith kinetics

(b) Hanhoun kinetics

(c) Ye kinetics

Figure 5.3: Comparison ideal and non-ideal cases with of without ionic speciation.

Irrespective of the kinetics used it is clear that the most significant effect on the rate of precipitation is produced by addition of speciation calculation (Cases 2

a/b). This result is expected, as the speed of precipitation is controlled by the appropriate indicator for saturation, which, for Cases 2, would be lower as it would be computed from the concentrations (Case 2a) or the activities (Case 2b) of the reacting ions, rather than the total concentrations of magnesium, phosphorus and nitrogen.

Cases where $\gamma =$ non-const (Case 1b and Case 2b) show slower precipitation rates than the cases where $\gamma =$ const (Case 1a and Case 2a). This is expected, because the variation in γ affects the values of saturation indicators which determine the rate of the precipitation.

Chemical conversion times

The stage of the reaction can be quantified using a chemical conversion indicator [68], which shows the amount of product species with respect to the initial reactant concentration. Generally it can be defined as follows:

$$\mathrm{Con}(MAP) = \frac{C_{MAP}}{\frac{1}{3}\sum_{j}^{3} C_j^0 - K_{SP}^{(1/3)}} \times 100\% \tag{5.20}$$

where C_j^0 correspond to the initial reactant concentrations.

For a one-dimensional stoichiometric case the chemical conversion formula is slightly simplified:

$$\mathrm{Con}(MAP) = \frac{C_{MAP}}{C_j^0 - K_{SP}^{(1/3)}} \times 100\% \tag{5.21}$$

Chemical conversion times for Galbraith, Hanhoun and Ye precipitation kinetics are presented in Tables 5.5, 5.6, 5.7 respectively. Chemical conversion comparison plots are displayed in Figure 5.4 for Galbraith, Hanhoun and Ye kinetics respectively. All of the graphs have points marked on the conversion curves that correspond to the 50%, 90% and 99% conversion values.

Results indicate that addition of ionic speciation decreases the maximum amount that can be converted in the system. Irrespective of the kinetics used and the precipitation kinetics used, Cases 2a and 2b produce maximum conversion rates

$Con \approx 98\%$, where as Cases 1a and 1b show maximum conversion rates of $Con \approx 99.7\%$.

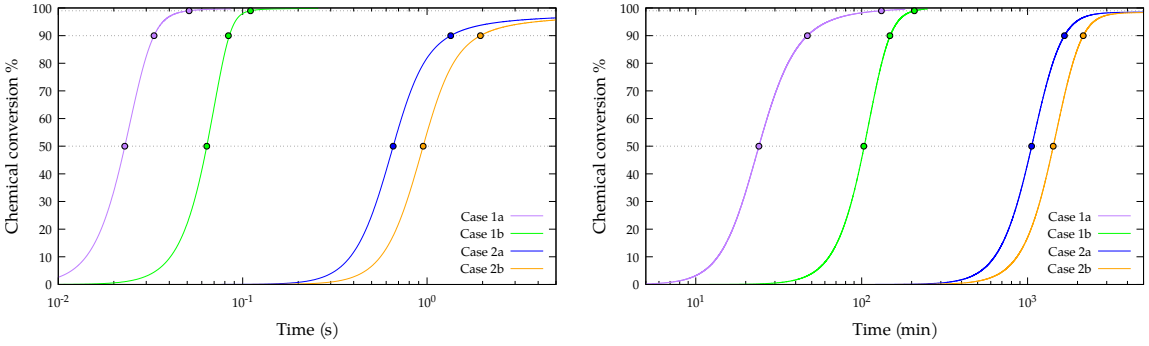

(a) Galbraith kinetics

(b) Hanhoun kinetics

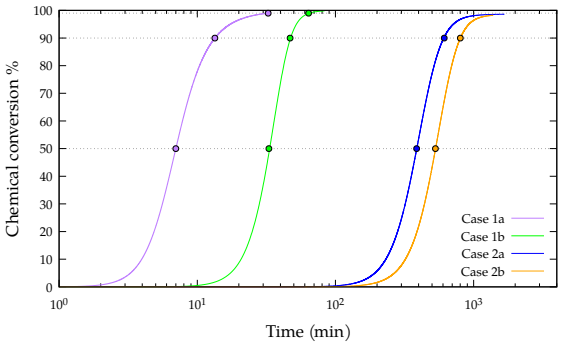

(c) Ye kinetics

Figure 5.4: Comparison of the chemical conversion over time.

Table 5.5: Chemical conversion times for Galbraith precipitation kinetics

Case Name	50% conversion	90% conversion	99% conversion
1a	0.023 s	0.033 s	0.0513 s
1b	0.0635 s	0.085 s	0.11 s
2a	0.65 s	1.34 s	N/A
2b	0.95 s	1.95 s	N/A

Table 5.6: Chemical conversion times for Hanhoun precipitation kinetics

Case Name	50% conversion	90% conversion	99% conversion
1a	24 min	47 min	131 min
1b	103 min	148 min	208 min
2a	1058 min	1668 min	N/A
2b	1428 min	2166 min	N/A

Table 5.7: Chemical conversion times for Ye precipitation kinetics

Case Name	50% conversion	90% conversion	99% conversion
1a	7 min	13 min	32 min
1b	33 min	47 min	65 min
2a	388 min	613 min	N/A
2b	530 min	802 min	N/A

5.3 Closure

Verification and kinetic studies have been presented in this chapter. Different kinetic models found in the literature have been tested against the semi analytical solutions obtained using the MATLAB code. The CFD solver showed well matching results for each of the kinetic models and the discrepancies seen in the figures presented can be attributed to the numerical errors that are to be expected. Therefore it has been concluded that the code is performing well numerically and the results can be considered valid.

The effects of the inclusion of the ionic speciation mechanism have been presented as well. Physically ionic speciation is an important thermodynamic condition of the solution which limits the reaction rates as well as the supersaturation levels in the system, therefore investigation of the effects gives an important indicator as to whether the specific kinetic model would be viable or not for the cases of interest. It has been observed that the kinetic models by Hanhoun and Ye show incredibly long reaction times, whereas the kinetic model given by Galbraith is much quicker and would seem to represent the spontaneous precipitation systems better. Even though Galbraith and Hanhoun models were both fitted against the data from similar experimental setups it is clear that the kinetic parameters are incredibly sensitive to the conditions of the experiment and the assumption being made. It is therefore an indicator that in order to apply the CFD model a system of choice it is crucial to perform the experimental study as well in order to establish the reaction kinetic mechanisms.

Chemical conversion times were also calculated for all of the cases using each of the kinetic models. It has been observed that inclusion of non-ideality together with ionic speciation reduces the total amount of precipitated struvite, which means that the level of the equilibrium saturation and therefore concentration is increased when such conditions are being used. It is also important to note that even though the pH levels were kept constant in the system throughout this study it is not an experimentally observed condition as the alkalinity of the solution is being reduced

during struvite precipitation reactions due to release of H^+ ions into the system. The variation of the alkalinity would be slowing down the reaction the closer it would be to the equilibrium state, therefore it is a suggestion for the future work to implement such a mechanism into the solver in order to capture the additional thermodynamics appropriately.

Chapter 6

Model Scale Simulations

This Chapter is dedicated to the application of the CFD and PBE coupled solver to two test cases with the Galbraith kinetic model described in Chapter 3. Due to the lack of experimental data available a decision has been made to use two test cases: the model scale settling tank by Dahl [35] and a model scale Hydrodynamic Vortex Separator. The simulations were used to predict the potential performance of such separator and settling tanks to act as reaction vessels. Conclusions regarding the potential of phosphorus removal, the mean diameter and the settling velocity of the dispersed phase are also presented in this Chapter.

6.1 Dahl case

In this section the present methodology for precipitation modelling is applied to investigate precipitation potential of a large experimental settling tank. Originally the settling tank was constructed at the Aalbourg wastewater treatment plant in Denmark by Dahl [35]. The hypothetical case was set up to reproduce similar flow conditions and reactant concentrations were chosen to be representative of the levels observed in wastewater.

Such model scale tanks are used experimentally due to a few key advantages. The dispersed phase concentration profiles as well as the influent volumetric flow rate

can be controlled at a much higher accuracy as opposed to the full scale tank. Measurements of the concentration and velocity profiles can be measured with much higher accuracy. Therefore even though as of the current date there is no data available for the precipitation processes in such tanks it would be possible to carry out experiments in the future in order to obtain validation data for the model.

6.1.1 Case setup

Experimental setup

The experimental setup provided by Dahl [35] has a test section 7.5m to 7.9m in length, 1m in width and 1m in depth. The diagram showing the experimental setup is presented in Figure 6.1. In the experiment Dahl [35] used an activated sludge solution that was fed to the system using a syphon conduit system. The flow rate into the system was controlled using feed valves. In order to control the concentration of the suspended solids the clean water was used to mix it with the influent sludge. This has been achieved by using the multi-hole baffles placed downstream of the inlet pipes.

Dahl [35] performed the experiments using two inlet design setups. The first experimental setup allowed the mixture to enter the test section freely after passing the mixing baffles. The second design had an inlet board placed 0.4m downstream from the last mixing baffle and the board had a 0.15m deep slit opening that ran across the full width of the tank and the bottom edge of the slit was situated at the 0.5m depth of the tank.

The end of the tank section consists of an outlet board placed such that there is a slit opening that ran across the full width of the tank and span 0.1m from the bottom of the tank to the outlet board. After the outlet board the effluent was pumped out back to the aeration tank. The water levels were kept constant throughout the experiment by adjusting the effluent flow rates accordingly.

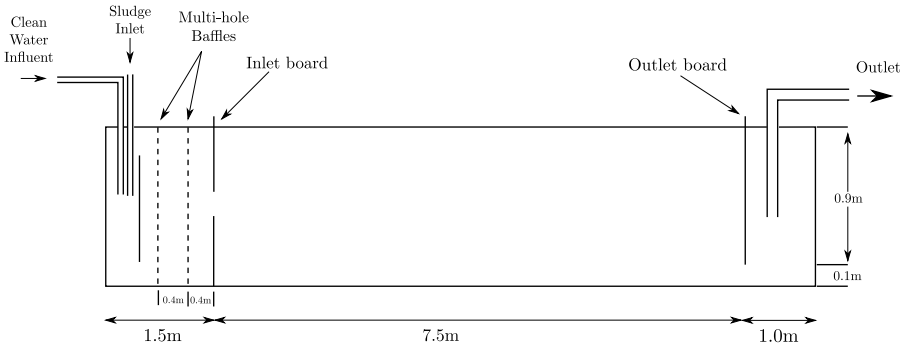

Figure 6.1: Diagram of the Aalbourg settling tank experiment (adapted from Brennan [21]).

Numerical Simulation setup

In this part of the study a two-dimensional representation of the full-depth inlet settling tank was modelled. The computational domain was initialised with no solids volume fraction present and the velocity field throughout the domain was set to the mean flow through the tank, which corresponded to $U_m = 0.0191 m/s$ and $U_m = 0.0054 m/s$ for cases labeled 1 and 2 respectively.

Turbulence modelling was achieved using Reynolds Averaged Navier-Stokes (RANS) equations with $\kappa - \varepsilon$ model. Brennan [21] has stated that for this particular settling tank the flow field inside the tank is independent of the inlet turbulent intensity, therefore for both cases a standard 10% value was used to determine initial conditions of the turbulent statistics.

At the start of the simulation it was assumed that the tank was purely filled with water and therefore the mass fractions of the chemical species were set to 0 throughout the domain. Inlet conditions were based on total molar concentration values which were chosen to be 0.001M for all of the chemical species.

The simulation were carried out using a second order accurate discretisation schemes on all of the convective terms in this model.

A brief summaries of the most relevant initial and boundary conditions are given in Figure 6.2 Table 6.1. For those interested in replicating the case study a full list

is provided in Appendix D.

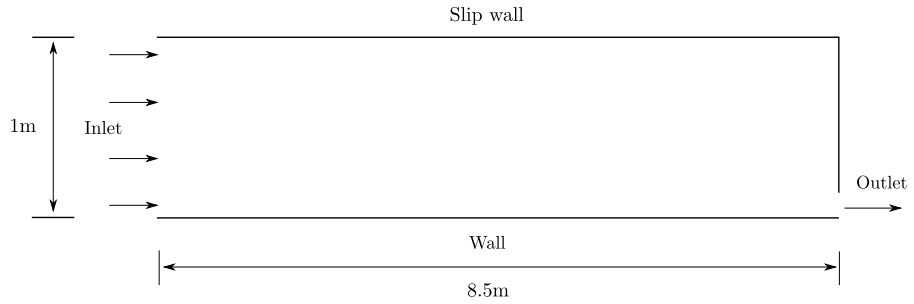

Figure 6.2: Boundary conditions of the case setup with a full depth inlet.

Table 6.1: Initial conditions of the Dahl case simulations.

Parameter	Case 1	Case 2
U_m	$(0.0191;\ 0;\ 0)\, m\, s^{-1}$	$(0.0054;\ 0;\ 0)\, m\, s^{-1}$
T_I	10%	
C^T_{P}	0.001 M	
C^T_{Mg}	0.001 M	
C^T_{N}	0.001 M	

Mesh independence

A succesive grid refinement analysis was performed to find the most appropriate mesh size for the study. Four different mesh sizes have been tested: $N_1 = 20,000$, $N_2 = 42,000$, $N_3 = 84,000$ and $N_4 = 120,000$ computational cells. Given that Sauter Mean Diameter is one the major properties of interes it was deemed an appropriate indicator of results mesh independence. The values of Sauter mean diameter were measured accross three vertical sampling lines positioned at $x = 3$m, $x = 5$m and $x = 7$m. The results variation was found to be insignificant between refinement levels N_3 and N_4 therefore the former mesh size was used for the final analysis of the case. Measurement plots are provided in Appendix E.

Precipitation kinetics

The precipitation kinetic models used for these simulations were introduced in Equations 5.3, 5.4. As observed from the verification studies presented in Chapter 5 the Hanhoun and the Ye precipitation kinetic models showed very long reaction times. The residence times of the model scale settling tank are shorter than the induction times as shown by Brennan [21], therefore it has been decided that in order to learn about the quality of struvite that could be precipitated using the settling tank, the Galbraith kinetic model would be the only suitable. In the future however, it is highly important to experimentally test the kinetic mechanisms that are dominant in the system in order to determine the specific precipitation kinetics that would occur in the tank. Kinetic models used for the simulation are shown below. The kinetic parameters for nucleation and growth, Debye-Hückel constant value and the solubility product value are presented in Table 6.2.

$$J = C_J(S_I)^{N_j}$$

$$G = C_G(S_I)^{N_g}$$

Table 6.2: Precipitation kinetics used in the Dahl simulation.

Parameter	Value
C_J	1.417×10^{9}
C_G	2.0817×10^{-6}
N_J	1.68
N_G	5.062
A_{DH}	0.509
K_{sp}	$10^{-13.26}$
pH	9.0

6.1.2 Case results

In this section the results from the Dahl case simulations are presented. Both settling models were tested in each of the two inlet velocities mentioned previously. The relevant parameters were extracted in order to understand the precipitation process and the potential inside the settling tank.

The four test cases presented have been classified and named based on the inflow conditions and the settling model used. The following Table 6.3 summarises the case names used.

Table 6.3: Summary of case names used.

Case name	Inflow velocity	Setling model
Case (1.a)	0.0191m/s	Simple-Varying
Case (1.b)	0.0191m/s	General-Varying
Case (2.a)	0.0054m/s	Simple-Varying
Case (2.b)	0.0054m/s	General-Varying

Hydrodynamics

Hydrodynamic performance of the settling tank was tested using a single-phase incompressible solver *simpleFoam*. Velocity streamline plots for both high and low inflow conditions are presented in Figures 6.3a, 6.3b respectively. Flow field in the settling tank is observed to be uniformly distributed in both cases. Non-uniformity in velocity field can be seen at the end part of the geometry, which is due to the fact that an outlet is placed at the bottom of the tank, therefore the velocity field values increase in that region.

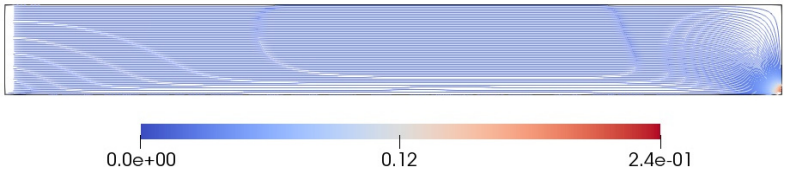

(a) Case (1) hydrodynamics

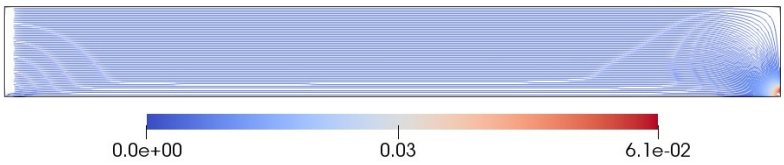

(b) Case (2) hydrodynamics

Figure 6.3: Settling tank hydrodynamics at different inflow velocities.

Cases (1.a) and (1.b)

Cases in this section were setup with the inlet inflow condition of $U_m = 0.0191m/s$. It was observed that both of the test cases exhibitted steady state flow regime at $t = 700$s after which no significant changes in the flow field were present. Figure 6.4 displays this behaviour in terms of the volume averaged Sauter mean diameter, which reached a steady state at around $t = 650$ seconds of flow time. After the steady state flow regime has been reached the flow parameter were time-averaged and the results are presented in this section. Some but not all of the instantaneous flow parameter values are used in this section, whereas a complete set of transient the outputs is provided in the Appendix F.

Table 6.4: Dahl Case 1 results summary.

Parameter	*Simple-Varying* model	*General-Varying* model
$U_{dr,d}$	8.89×10^{-5}	0.30×10^{-5}
d_{43}	22.46μm	22.39μm

Both Cases (1.a) and (1.b) showed identical hydrodynamic performance. The flow field distributions shown in Figures 6.5a and 6.5b are identical to the values predicted by the steady state simulations discussed earlier in this chapter.

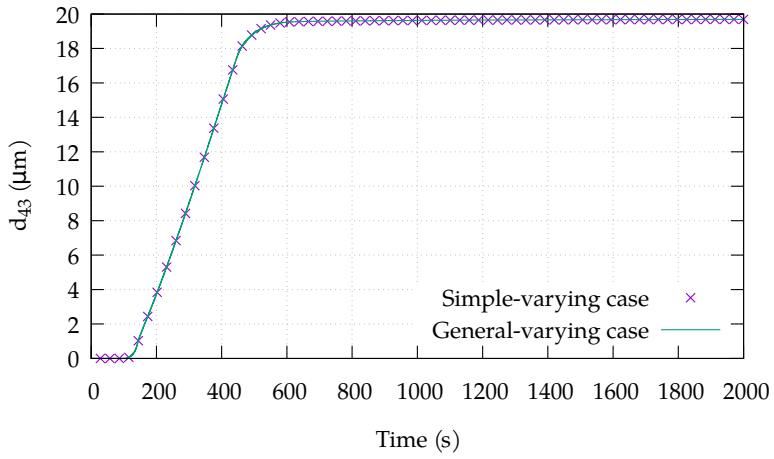

Figure 6.4: Volume averaged diameter evolution for both of the settling velocity cases.

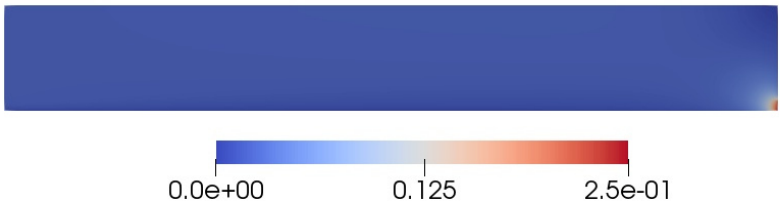

(a) Case (1.a) average U_m

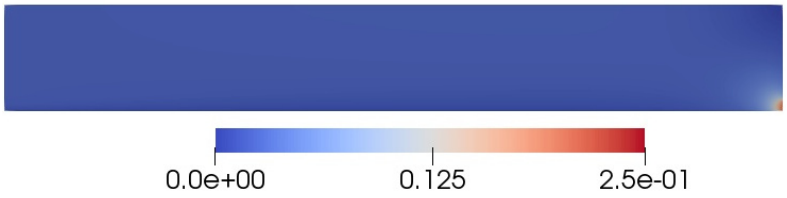

(b) Case (1.b) average U_m

Figure 6.5: Time-averaged values of the mixture velocity U_m fields for $0.0191 m/s$ inflow cases.

Predictions of the Sauter mean diameter were almost identical with maximum values observed as $d_{43} = 22.46 \mu m$ and $d_{43} = 22.39 \mu m$ for Cases (1.a) and (1.b) respectively. These results are not unexpected due to the fact that precipitation kinetics and population balance models used in both cases were identical. The values themselves show the same order of magnitude of $10^{-6} m$, however some differences exist due to the hydrodynamics introduced at this stage of the study

(one-dimensional test case described in Chapter 5 predicted Sauter mean diameter to reach maximum values of $d_{43} = 9.6\mu m$). The resulting values observed are summarised in Table 6.4.

The key difference between Case (1.a) and Case (1.b) was the use of different settling models. Case (1.a) incorporated *Simple-Varying* settling model 3.45 whereas Case (1.b) modelled settling velocity using *General-Varying* model 3.46. A single exponent *Simple-Varying* model predicts the settling velocity to reach maximum values of $U_{dr,d} = 8.89 \times 10^{-5} m/s$. On the other hand the double exponent *General-Varying* model results in maximum settling velocity values of $U_{dr,d} = 0.3 \times 10^{-5} m/s$. Figure 6.6 provides visual comparison between the mean distributions of the magnitudes of the settling velocity fields. The values are also summarised in Table 6.4. This result is reasonable, because *General-Varying* model formulation uses a double exponents in order to account for low concentration non-settlable particulates. During precipitation process low concentration non-settlable particulates are being formed which then are grown in size through growth kinetics of precipitation therefore *General-Varying* is believed to capture the settling physics better than the *Simple-Varying* settling model.

The time-averaged distributions of the volume fraction presented in Figures 6.7a and 6.7b supports the difference between different settling models. The volume fractions are observed to have maximum values of $\alpha_d = 4.3 \times 10^{-5}$ and $\alpha_d = 3.6 \times 10^{-5}$ for *Simple-Varying* and *General-Varying* settling models respectively. The results show that in both cases volume fraction is starting to form a denser region at the bottom of the tank. Similar behaviour has been reported in studies by Brennan [21] and Dahl [35]. To better illustrate that Figure 6.8 displays data values along three vertical sampling lines positioned at $x = 4m$, $x = 5m$ and $x = 7m$ locations named St1, St2, St3 respectively. The sample plots clearly show the existence of higher volume fraction regions at the bottom part of the tank. The plots also show the differences between the results in both of the cases discussed in this Section.

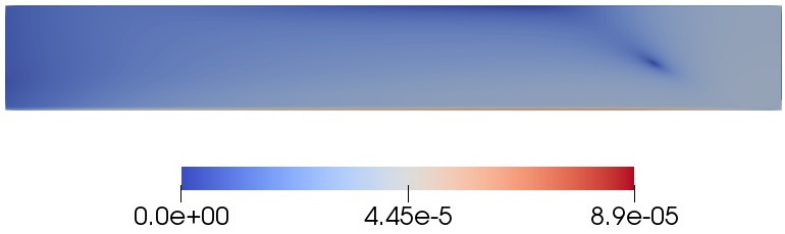

(a) Case (1.a) average $U_{dr,d}$

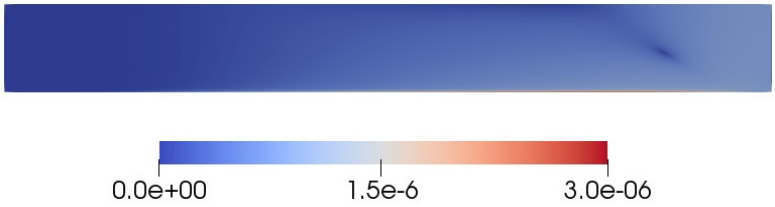

(b) Case (1.b) average $U_{dr,d}$

Figure 6.6: Time-averaged values of the *Simple-Varying* and *General-Varying* settling velocity $U_{dr,d}$ fields for the $0.0191 m/s$ inflow cases.

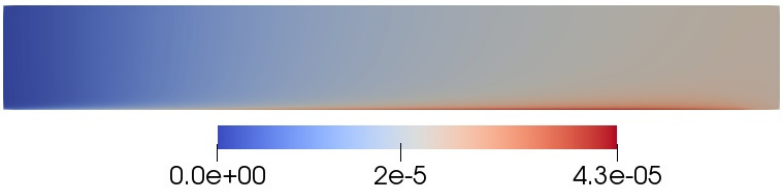

(a) Case (1.a) average α_d

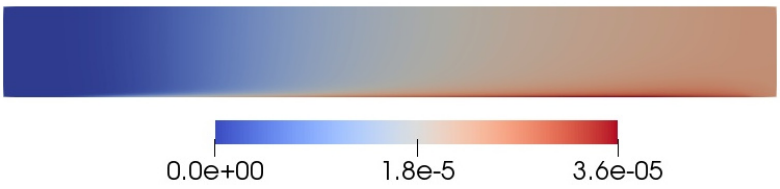

(b) Case (1.b) average α_d

Figure 6.7: Time-averaged struvite volume fraction α_d fields for the $0.0191 m/s$ inflow cases.

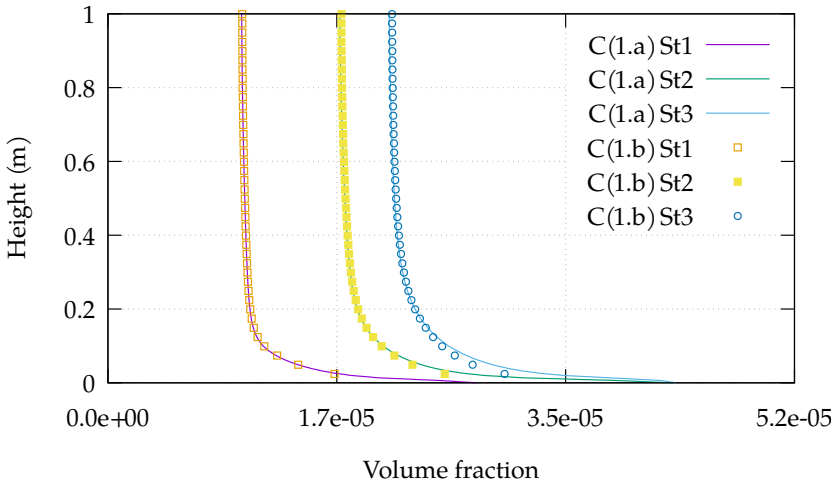

Figure 6.8: Sampled measurements of the averaged volume fraction α_d field at different parts of the settling tank.

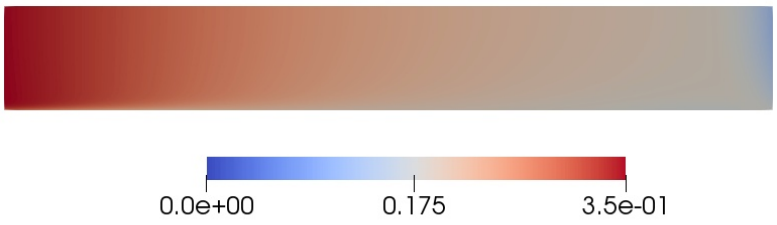

Figure 6.9: Mean distribution of the saturation index SI throughout the settling tank.

In order to evaluate the state of the precipitation reaction distribution of the saturation index is presented in Figure 6.9. Relatively small variations of the saturation index observed are an indication that the operational flow condition of $0.0191 m/s$ is too large and the reactants reach the end of the tank before substantial reaction process occurs. The values of the reacting ions sampled at three vertical locations used in previous paragraph display small variations across most of the height of the settling tank. The lowest reactant concentrations are observed at the bottom of the tank where largest values of the solids volume fraction α_d are observed. The sampled values of the reactant ion concentrations are displayed in Figure 6.10.

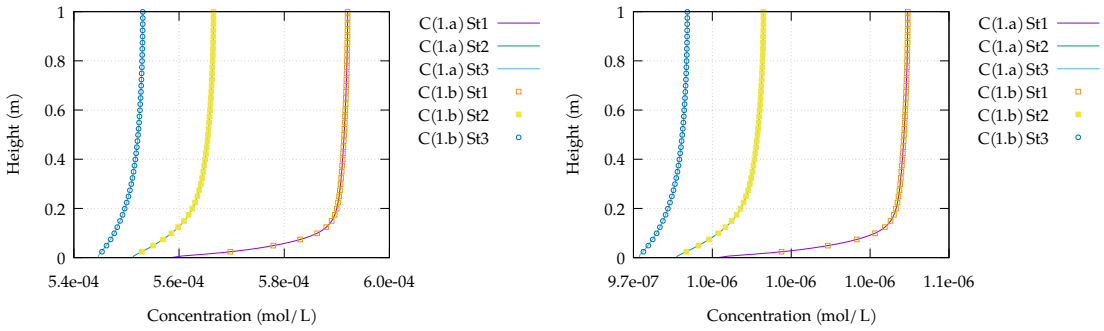

(a) C_{Mg} (b) C_{PO4}

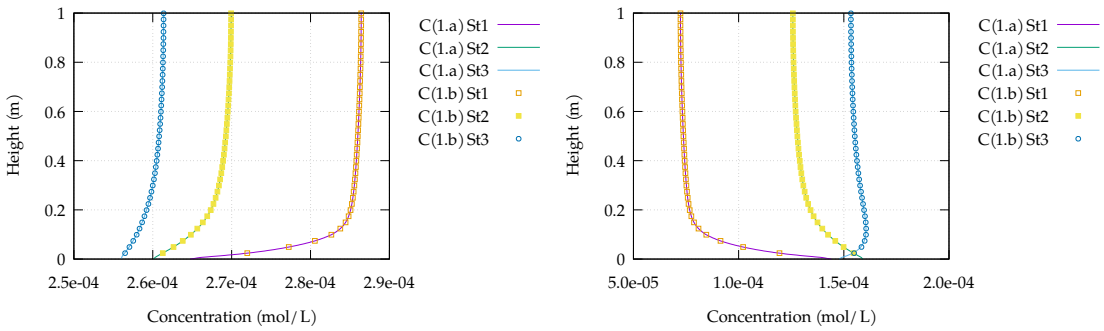

(c) C_{NH4} (d) C_{MAP}

Figure 6.10: Time-averaged values of the reactant and product concentrations measure at different sections of the settling tank.

Cases (2.a) and (2.b)

Cases in this section were prepared with the inlet inflow condition of $U_m = 0.0054m/s$. It was observed that both of the test cases exhibitted steady state flow regime at $t = 4000$s after which no significant changes in the flow field were present. Figure 6.11 displays this behaviour in terms of the volume averaged Sauter mean diameter, which reached a steady state at around $t = 4000$ seconds of flow time. After the steady state flow regime has been reached different parameters were time-averaged and the results are presented in this section.

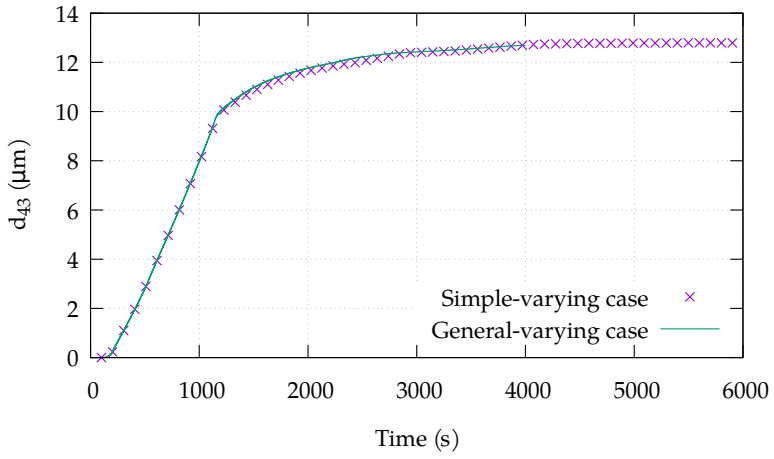

Figure 6.11: Volume averaged diameter evolution for both of the settling velocity cases.

Table 6.5: Dahl Case 2 results summary.

Parameter	Simple-varying mode	General-varying model
$U_{dr,d}$	4.54×10^{-5}	1.5×10^{-5}
d_{43}	14.97μm	14.95μm

Both Cases (2.a) and (2.b) showed identical hydrodynamic performance. The mixture velocity U_m distributions presented in Figures 6.12a and 6.12b are identical irrespective to what settling velocity model has been used. The main differences are observed when compared to the results presented at the start of this chapter.

Streamline visualisation presented in Figure 6.13 show that a recirculation zone is formed at the first half of the settling tank. Such recirculation zone is a distinctive feature observed in both Cases (2.a) and (2.b) and appears to occur due to the increased amount of the dispersed phase in that region.

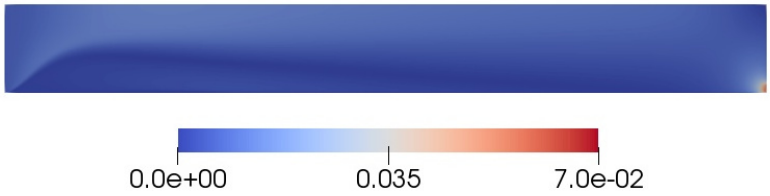

(a) Case (2.a) average U_m

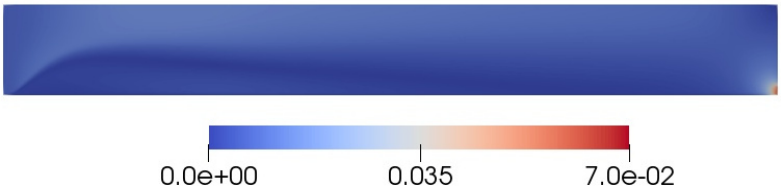

(b) Case (2.b) average U_m

Figure 6.12: Time-averaged values of the mixture velocity U_m fields for $0.0054m/s$ inflow cases.

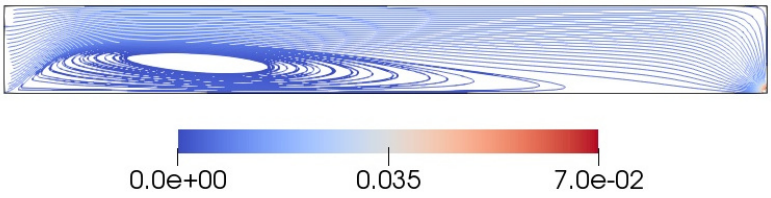

Figure 6.13: Velocity streamline plots for Cases (2.a) and (2.b).

The volume fraction time-averaged distributions are shown in Figures 6.14a and 6.14b. The comparative figures have been scaled to show the similarities between the mean volume fraction distributions in the settling tank. However the maximum values observed in Case (2.a) are $\alpha_d = 1.79 \times 10^{-4}$ whereas the maximum values observed in Case (2.b) are $\alpha_d = 0.37 \times t0^{-4}$. As discussed previously this can be attributed to the mathematical formulation of the *Simple-Varying* settling model that predicts the settling even when the volume fraction is low, whereas *General-*

Varying settling model used in Case (2.b) requires sufficient volume fractions to be present before any reasonable settling can be achieved.

Predictions of the Sauter mean diameter were almost identical with maximum values observed as $d_{43} = 14.97\mu m$ and $d_{43} = 14.95\mu m$ for Cases (2.a) and (2.b) respectively. These results are not unexpected due to the fact that precipitation kinetics and population balance models used in both cases were identical. The values themselves show the same order of magnitude of $10^{-}6m$, however some differences exist due to the hydrodynamics introduced at this stage of the study (one-dimensional test case described in Chapter 5 predicted Sauter mean diameter to reach maximum values of $d_{43} = 9.6\mu m$). The resulting values observed are summarised in Table 6.5. Figures 6.15a and 6.15b display d_{43} distributions observed in both test cases. Predicted distributions do not exhibit any substantial differenced, however this is to be expected due to the fact that the nucleation and growth models used in both Case (2.a) and Case (2.b) are the same.

Same as in previous section the primary difference between Cases (2.a) and (2.b) was the use of a single exponent and double exponent settling models respectively. Settling velocities presented in Figures 6.16a and 6.16b show the variations across the settling tank. It can be observed that the *General-Varying* settling model used in Case (2.b) predicts that the dispersed phase settling is three times lower than the predictions observed in Case (2.a). The distributions of the fields are very similar, but it has to be noted that the reason for the non-uniformity of the field at the areas with high volume fraction is currently unclear and requires additional investigation.

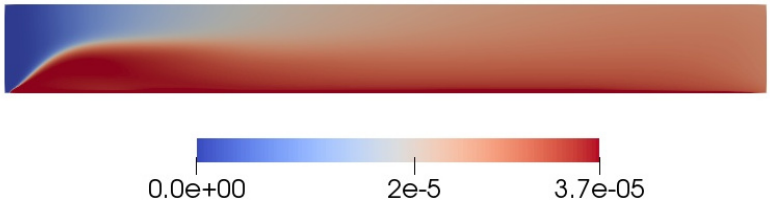

(a) Case (2.a) average α_d

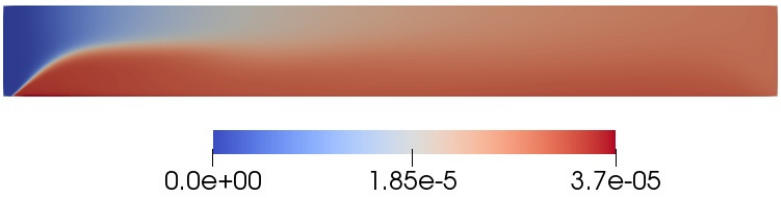

(b) Case (2.b) average α_d

Figure 6.14: Time-averaged struvite volume fraction α_d fields for the $0.0054 m/s$ inflow cases.

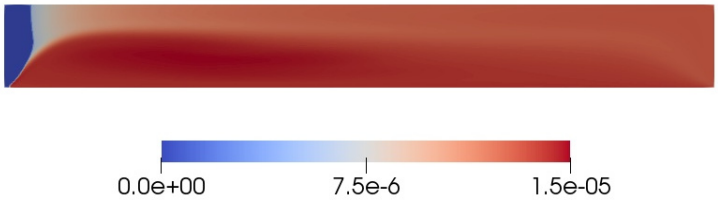

(a) Case (2.a) average d_{43}

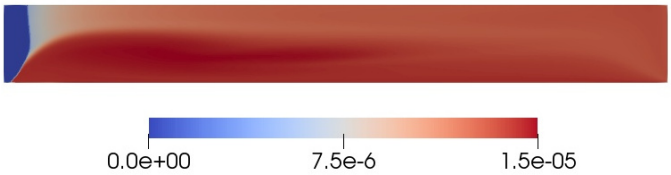

(b) Case (2.b) average d_{43}

Figure 6.15: Time-averaged values of the Sauter mean diameter d_{43} values for the $0.0054 m/s$ inflow cases.

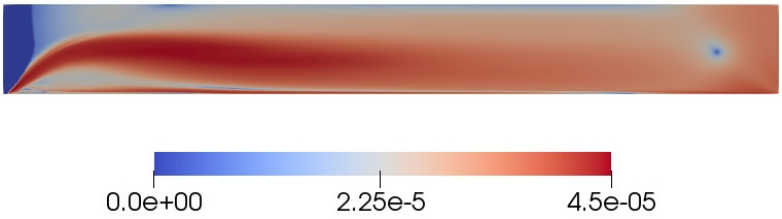

(a) Case (2.a) average $U_{dr,d}$

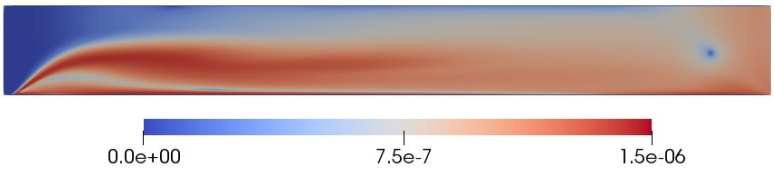

(b) Case (2.b) average $U_{dr,d}$

Figure 6.16: Time-averaged values of the *Simple-Varying* and *General-Varying* settling velocity $U_{dr,d}$ fields for the $0.0054m/s$ inflow cases.

Similarly as it has been observed in Cases (1.a) and (1.b) ractant ions variation is not substantial and therefore the saturation index was used as an indicator of the reactive state of the system. Figure 6.17 shows the mean distributions of the saturation index throughout the settling tank. It can be seen that at the start of the tank there is a low reaction zone is formed at the region where there is a an increased amount of volume fraction. Further towards the end of the tank uniformity of the saturation field is achieved, which is also supported by the distributions of the volume fraction field as well as Sauter mean diameter distribution. Sampling plots presented in Figure 6.18 show the reactant ion values observed along three vertical sampling lines positioned at $x = 3m$, $x = 5m$ and $x = 7m$ locations. The sampling line plots

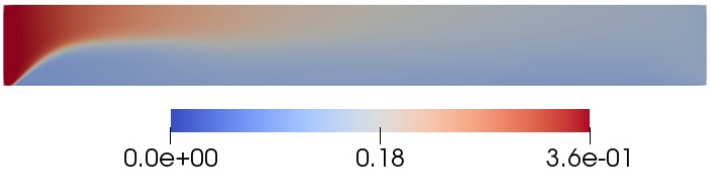

Figure 6.17: Mean distribution of the saturation index SI throughout the settling tank.

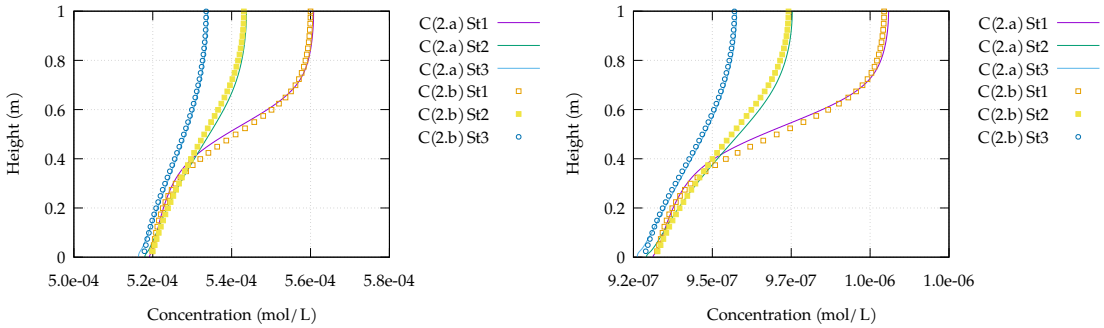

(a) C_{Mg} (b) C_{PO4}

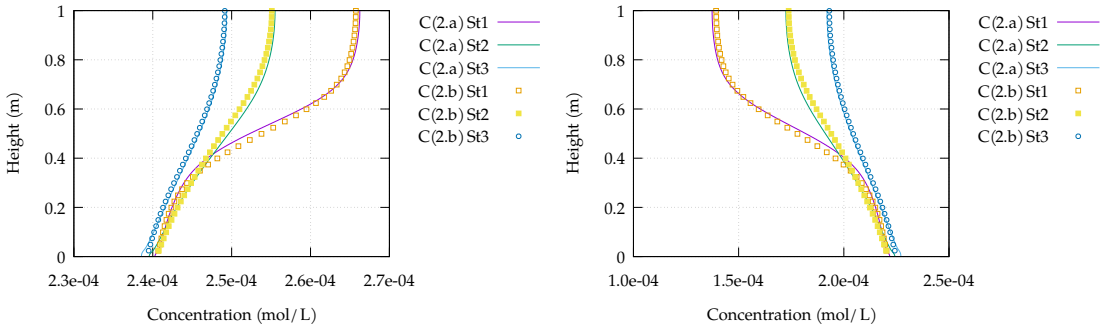

(c) C_{NH4} (d) C_{MAP}

Figure 6.18: Time-averaged values of the reactant and product concentrations measure at different sections of the settling tank.

Discussion

The two sets of simulations performed in this section show that under appropriate conditions the settling tank could potentially be used as a reaction vessel for precipitation. However, it is noted that the process is observed to be very sensitive to the flow rate values. Both cases that employ an inflow velocity flow rate of 0.0191m/s indicated that these operational conditions are suboptimal for precipitation to occur efficiently. The flow does not allow the properties of the dispersed phase to develop sufficiently and the settling process to be established.

On the other hand both cases with the inflow boundary condition of 0.0054m/s started to develop a significant dispersed phase layer on the bottom wall of the settling tank. This significantly affects the hydrodynamic state of flow when compared to the single-phase simulation presented at the start of this chapter. A recirculation is formed which is believed to increase the level of precipitation in the system due to increased mixing state of the chemical reactants.

The mean diameter of the dispersed phase however was observed to have values that are comparable to the 1D verification study performed in Chapter 5. Even though an experimental validation study is required in order to understand more about the validity of the predicted values, these results show potential and with further investigation optimal operating conditions could be established to increase the yield of the precipitant in the system.

Settling velocities observed in both sets of cases showed that a double exponent *General-Varying* accounts for non-settlable particulates whereas *Single-Varying* does not and therefore is expected to overpredict the level of settling in some regions. The distribution of settling velocity observed in Cases (2.a) and (2.b) display non-uniformity at the regions of higher volume fractions which is not expected and therefore requires further investigation to understand the reason for that.

6.2 Hydrodynamic vortex separator case

In this section the present precipitation modelling methodology is applied to a Hydrodynamic Vortex Separator (HDVS) in order to investigate the potential for this to act as a reaction vessel in precipitation processes. As mentioned in the previous Chapters the HDVS has been developed by Hydro International®and is used as a passive device in solid-liquid separation of the primary wastewater stream. However, due to constantly growing scarcity of phosphates in the world it is highly important to find alternatives to recover these essential materials.

Currently there is no available experimental data of the reaction chemistry therefore the numerical simulation was performed to investigate the potential yield of struvite of the HDVS. The simulation performed was used to extract information on the diameter of the dispersed phase, the maximum settling velocity that the struvite crystals can obtain during the operation of the product, and to identify the critical reaction zones of the vortex separator.

6.2.1 Case setup

Model scale HDVS geometry setup

A model scale Hydrodynamic Vortex Separator chosen for the simulation can be subdivided into three main sections: the inlet pipe, the main cylinder and the underflow cylinder. The 0.028m diameter inlet pipe is tangentially connected to the main cylinder and was extended to $L = 1.7$m in order to obtain a developed flow. The main and the underflow cylinders have diameters 0.6m and 0.24m respectively. The underflow outlet pipe which is tangentially connected to the underflow cylinder has a 0.045m diameter.

The diagram presented in Figure 6.19 shows the relevant dimensions of the vortex separator.

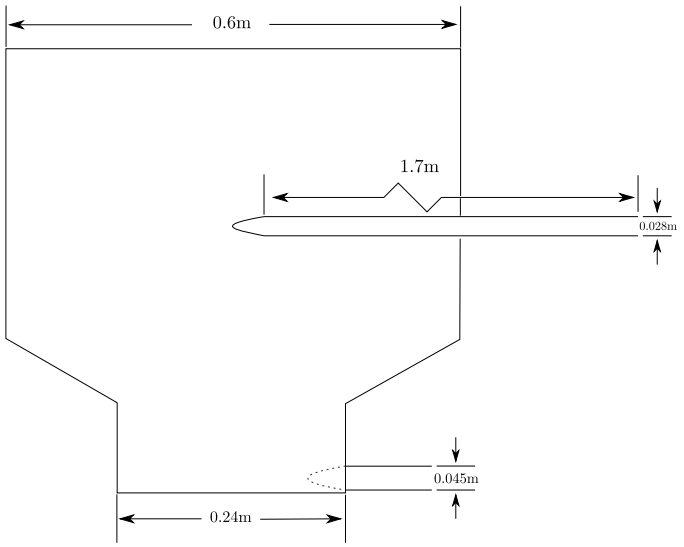

Figure 6.19: Side view of the vortex separator geometry presenting the relevant dimensions.

Boundary and initial conditions

The boundary conditions for the case are presented in Figure 6.20. The inlet mixture velocity was set to have a uniform value of $U_m = 0.918m/s$ which is the standard operational inflow condition for HDVS and corresponds to the loading rate of $L = 2Ls^{-1}m^{-2}$. The overflow outlet boundary conditions were set as zeroGradient and the underflow was set to a uniform outflow rate of 0.05m/s. The top lid of the tank was set as symmetry which effectively is a slip boundary condition. The inlet, the underflow and the main cylinder walls were all set to a wall boundary condition. The case was first initialised with the tank filled with water. At the start of the simulation the reacting solution containing equal concentrations of the reactant species was fed through the inlet into the system. Initial total concentrations of phosphate, magnesium and nitrogen were set to 0.01 molar. As the exact turbulent intensity value was not known a 5% was used as it is a usual value chosen for turbulent simulations. The turbulent kinetic energy therefore was set to have a value of $0.00316ms^{-2}$ and the turbulent energy dissipation was set to $0.00057m^2s^{-3}$. The relevant initial conditions are summarised in Table 6.6.

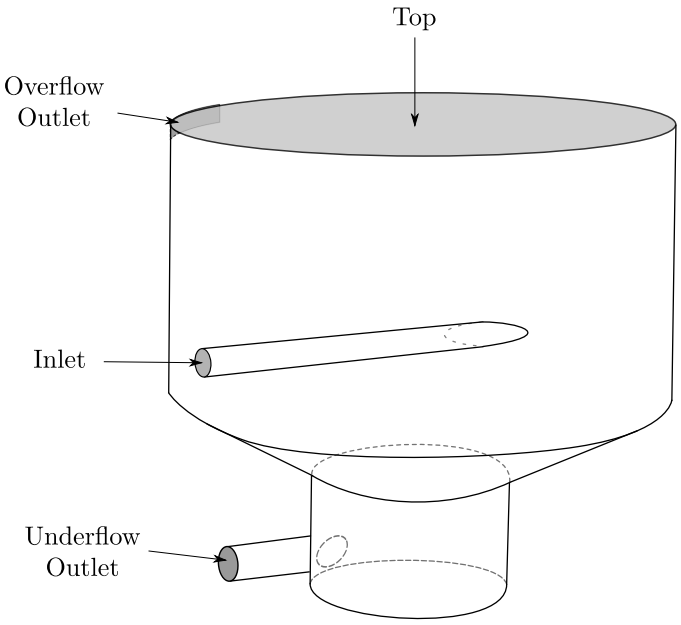

Figure 6.20: Boundary conditions of the vortex separator case.

Table 6.6: Initial conditions of the HDVS simulation.

Parameter	Value
U_m	$(0.918;\ 0;\ 0)\, m\, s^{-1}$
ε	$0.00057\, m^2\, s^{-3}$
κ	$0.00316\, m^2\, s^{-2}$
C^T_{P}	0.01 M
C^T_{Mg}	0.01 M
C^T_{N}	0.01 M

Numerical setup

a) Computational mesh

A three dimensional representation of the reactor vessel was created and used in all cases used in Sections followed. A tetrahedrally dominant unstructured mesh was generated and consisted of $270,000$ computational cells.

Due to the fact that cases were computationally very challenging mesh independence analysis was not performed for this part of the study, therefore the following sections should be treated as a case study and this has been left as future work for

researchers who decide to use the framework.

b) Single-phase test case setup

A single-phase steady state simulation was performed to obtain a base hydrodynamic performance of the vessel. The results were computed using a steady state *simpleFoam* solver which is based on *SIMPLE* algorithm (see Patankar [109] for details). The solution was calculated from incompressible Navier-Stokes equations. Turbulence was modelled using RANS equations with $\kappa - \varepsilon$ turbulence model.

c) DFM test case setup

A second part of the cases study consisted of a multi-phase simulation performed purely using drift-flux model solver *driftFluxFoam*, which is part of OpenFOAM. The aim was to obtain a base dispersed phase settling performance of the vessel. The solution was achieved using *PIMPLE* algorithm (see Patankar [109] for details.). Drift-flux mixture model equations presented in Section 3.2.2.3 were solved together with RANS equations using $\kappa - \varepsilon$ turbulence model [109].

d) Precipitation case setup

The last test case incorporated all modelling aspects the framework is capable of covering. Hydrodynamics were handled using DFM model (as presented in Section 3.2.2.3) with turbulence modelled using RANS equations with $\kappa - \varepsilon$ model.

Disolved species transport was modelled using scalar transport convection-diffusion equations as discussed in Section 3.3.1. Ionic concentrations of reactants were calculated using non-ideal equilibrium thermodynamics formulation as shown in Section 3.3.2 as well as Appendix B. Precipitation kinetics were handled using Galbraith kinetic models presented in Equations 5.3, 5.4. As observed from the verification studies presented in Chapter 5 the Hanhoun and the Ye precipitation kinetic models showed very long induction times. The residence times of the model scale vortex separator are known to be less than 10 minutes, therefore it has been decided that in order to learn about the quality of struvite that could be precipitated inside the separator tank the Galbraith kinetic model would be the only suitable choice. In

the future however it is highly important to test the separator experimentally and determine the specific precipitation kinetics that would occur in the tank. Kinetic models used for the simulation are shown below. The kinetic parameters for nucleation and growth, Debye-Hückel constant value and the solubility product value are presented in Table 6.7.

$$J = C_J(S_I)^{N_j}$$
$$G = C_G(S_I)^{N_g}$$

Table 6.7: Precipitation kinetics used in the HDVS simulation.

Parameter	Value
C_J	1.417×10^{9}
C_G	2.0817×10^{-6}
N_J	1.68
N_G	5.062
A_{DH}	0.509
K_{sp}	$10^{-13.26}$
pH	9.0

Lastly the evolution of the crystal size distribution was handled using Equations 3.133. The solution of algorithm used was briefly presented in Section 4.3, however because development of these algorithms were not part of this research project reader is directed to the original authors of OpenQBMM framework Passalacqua et al. [107] for more details.

6.2.2 Single phase steady state simulations

Hydrodynamic Vortex Separator single phase simulation has been performed in order to develop an understanding about the hydrodynamic conditions that should be expected in the tank.

Simulations were performed using *simpleFoam* solver which is a steady state solver. The convergence criteria for the solution was set to as 10^{-3} for pressure, 10^{-7} for velocity U and turbulent statistics κ, ε. The solution did not converge to the specified values, however it reached a stable regime were residuals did not decrease further and at that point a decision has been made to stop the simulation.

Visualisation presented in Figure 6.21 shows flow patterns accross multiple horizontal slices of the geometry. It is clear that the fluid flow loses a lot of kinetic energy after entering the main tank and carries on in a swirling motion throughout.

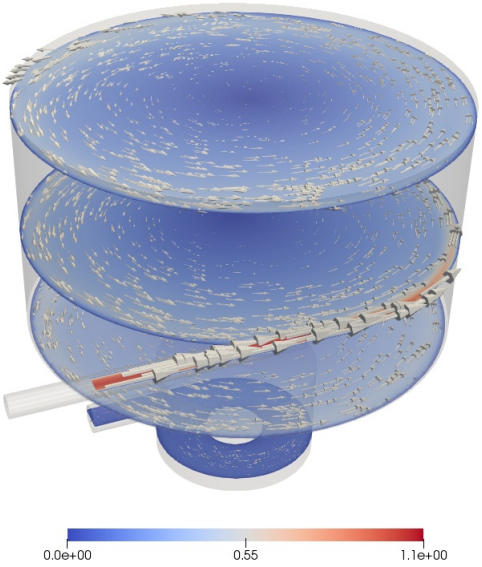

Figure 6.21: Visualisation of the flow vectors and the flow field values across multiple horizontal slices throughout the geometry.

Crucial parts of the geometry are the overflow and the underflow sections. Figures 6.22a, 6.22b show the flow patterns in the overflow and the underflow cross-sections

respectively. It can be seen that the maximum velocity in the overflow section is predicted to be $U = 0.44\text{m/s}$ and in the underflow section it is predicted to be $U = 0.11\text{m/s}$. This is to be expected as the underflow outlet velocity is prescribed, however in the future different boundary condition configurations should be carried out to find the most optimum setup that achieves the best performance in solid removal from the tank.

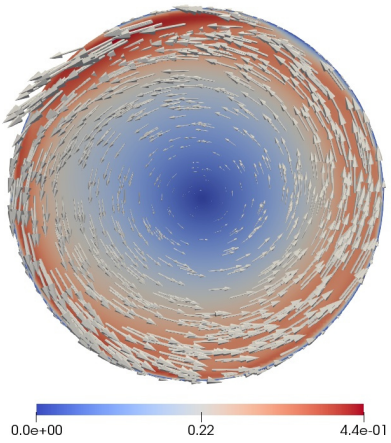

(a) The overflow velocity distribution

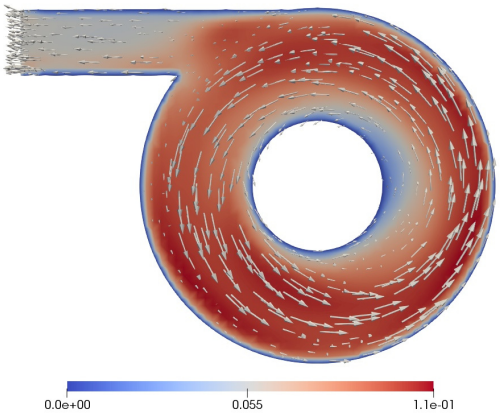

(b) The underflow velocity distribution

Figure 6.22: The single phase velocity distributions in the overflow and the underflow sections of the HDVS tank.

6.2.3 Multiphase DFM simulations

Test case simulation presented in this Section has been performed in order to obtain a reference solution for the mixture model solution in the reaction vessel. As discussed in Section 6.2.1 only drift flux mixture model equations presented in Section 3.2.2.3 and turbulence modelling was achieved using RANS equations with $\kappa - \varepsilon$ model.

At this stage reaction kinetics and population balance modelling was not considered, therefore volume fraction α_d values were prescribed at the inlet. The values were set to 0.0001. Inlet boundary condition value was chosen based on the previous test cases presented earlier in this chapter, all of which have indicated that such values can be expected when reaction kinetics and population balance modelling is taken into account.

The transient simulation was performed until a pseudo steady state flow regime was reached which corresponded to 90s of flow time; after that the time averaging of the parameters was performed for another 30s and these values were used to investigate the conditions of the multiphase flow in the separator tank.

The mixture velocity values observed in the overflow and the underflow sections of the tank have reached the values of $U_m = 1.1$ m/s and $U_m = 9.4 \times 10^{-2}$ m/s respectively. The volume fraction of the dispersed phase showed its maximum value in the underflow part of the tank with the largest values of $\alpha_d = 7.1 \times 10^{-4}$. Figure 6.24a shows solids volume fraction distribution as well as iso-contour lines at different parts of the reactor tank. Largest values of volume fraction are observed around the conical part of the underflow section at the bottom of the tank.

The drift velocity was modelled using the *Simple* settling velocity model provided in Equation 3.38. The mean distribution of the values show that the largest values are observed in the middle parts of the tank. The largest values of the settling velocity are observed to be at $U_{dr,d} = 2.2 \times 10^{-3}$ m/s, which corresponds to the terminal velocity values of $U_0 = -2.2 \times 10^{-3}$ m/s that were fixed for this numerical

simulation.

Figure 6.24b shows time-averaged distribution of the settling velocity. It can be observed that the model predicts settling velocity to be mostly uniform throughout the majority of the tank with lower values predicted at the high volume fraction regions. The results are as expected from a *Simple* settling velocity model as it does not capture the physics of non-settleble low volume fraction solids (which are usually taken as $\alpha_{min} = 2 \times 10^{-5}$ see Brennan [21]).

It has to be noted that uneven values observed at the walls of the tank are due to the nature of the unstructured mesh, that was used for this study and it would be resolved with a fully tetrahedral mesh, however it does not affect the results and has been left as future work.

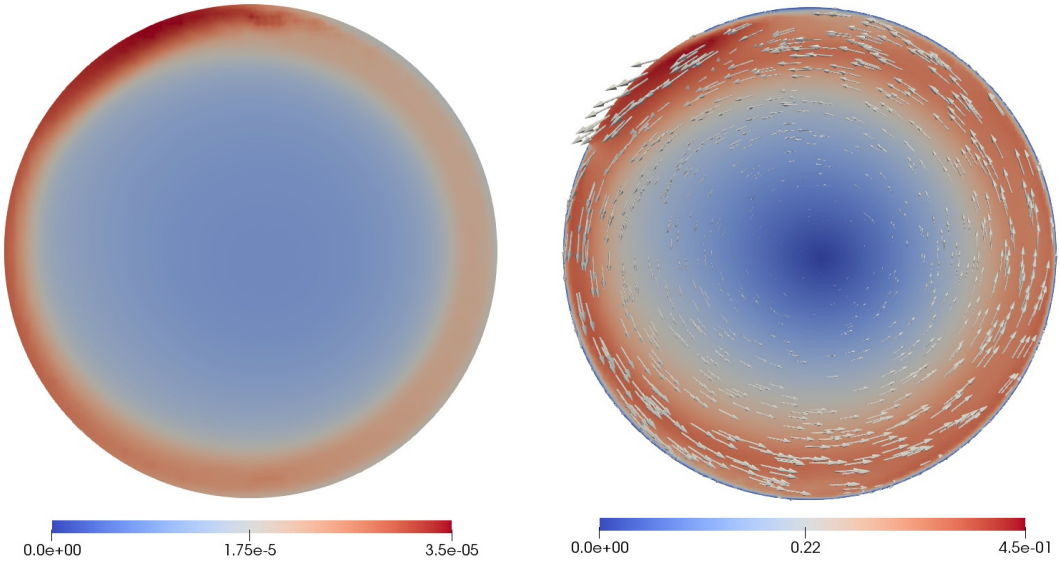

(a) α_d mean distribution

(b) U_m mean distribution

Figure 6.23: The mean volume fraction and the mean mixture velocity distributions at the overflow section of the tank.

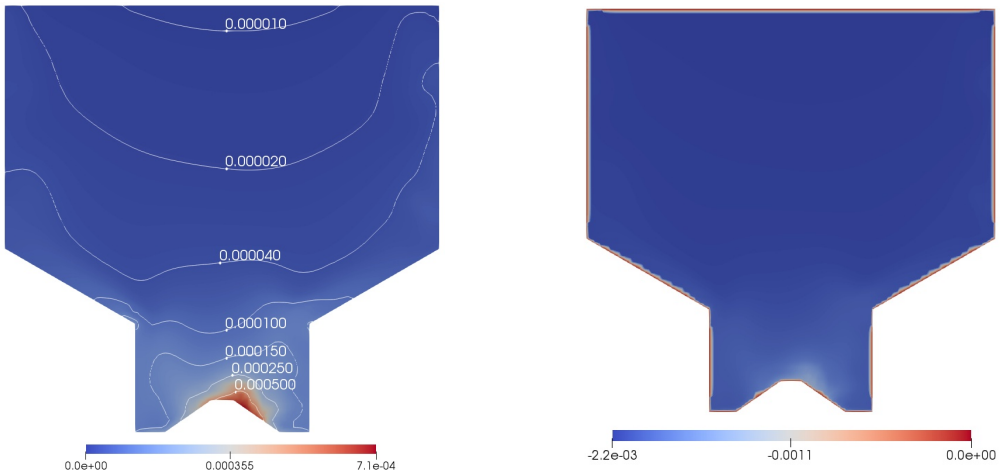

(a) α_d mean distribution

(b) $U_{dr,d}$ mean distribution

Figure 6.24: The mean distributions of the volume fraction α_d of the dispersed phase and the mixture velocity $U_{dr,d}$ at the vertical cross section of the tank.

6.2.4 Simulations of struvite precipitation process in HDVS

The following sections present results obtained from multiphase transient simulation incorporating drift flux mixture model, chemical species transport, ionic species equilibrium thermodynamics and population balance modelling framework.

The solution results are presented in four subsections each of which are used to discuss information obtained from the simulations. These subsections represent different parts of the separator tank: the inlet pipe, the underflow section, the overflow section and the cross-section of the main cylinder.

Inlet pipe

Precipitates inside the inlet pipe at the beginning of the simulation are observed to start forming at the time of $t = 1$s at an approximate 0.85m length away from the inlet patch. In this geometrical setup this corresponds to around 10.7 of the pipe diameter lengths. The Galbraith kinetic models used in this case have very quick reaction rates, therefore the induction times are short, which has been observed during the one dimensional studies discussed in the previous Chapter. The time averaged solids volume fraction at the final time step of the simulation in the inlet pipe had reached a maximum value of $\alpha_d = 2.7 \times 10^{-5}$ with the mean diameter values of $d_{43} = 24\mu$m and the minimum value of $\alpha_d = 2.4 \times 10^{-10}$. This value is observed to be at the point where the inlet pipe meets the main cylinder.

The volume fraction of the solid phase is presented in Figure 6.25.

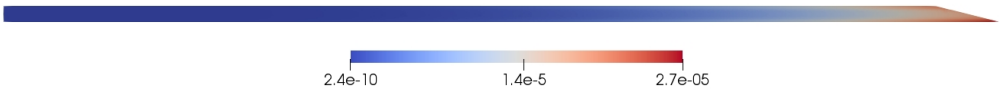

Figure 6.25: The time averaged dispersed phase volume fraction inside the inlet pipe at $t = 210$s.

Main cylinder section

This section is dedicated to presenting results observed in the main cylinder part of the reactor. Due to computational intensity that three dimensional case poses only a limited number of simulation runs have been performed, therefore as mentioned earlier in this chapter the results should be treated as a case study rather than a validated representation of physics in a reactor tank. The relevant parameters were extracted from the simulations allowed an evaluation of the potential for the HDVS product to be used as a reactor vessel for struvite precipitation process. The transient simulations of the HDVS were allowed to run until a steady state flow regime has been reached. After that the parameters were time-averaged for 30 seconds of flow time and these were used for this analysis.

Line graphs presented in Figures 6.26a, 6.26b, 6.26c show ion concentration values of phosphorus, ammonia and magnesium respectively taken along a sampling line through the horizontal mid section of the tank at the vertical height of $0.4m$. Values were sampled at few different times and indicate that no significant changes can be observed in the concentrations of the reacting ions, which indicate that a steady state flow regime is reached in the system.

The distribution of the volume fraction of solid phase are presented in Figure 6.27a. The averaged values were recorded at $t = 210$s of flow time and show that struvite crystals form concentrated regions around the conical parts of the tank connecting the larger cylindrical part of the tank with the underflow section of the tank. These values correlate with the distribution of the Sauter mean diameter presented in Figure 6.27b as the largest sized particulates are predicted in the same regions of the tank. The contour lines specified in Figure 6.27a show the specific values of observed around these crucial regions of the vessel.

The Sauter mean diameter values predicted also show the variation of the particulate size distribution across the vessel. The minimum values in the main cylinder part of the tank discussed in this section are found to be $d_{43} = 20.1\mu m$ whereas the maximum values observed are $d_{43} = 28.7\mu m$. These values correlate with the

Sauter mean diameter predictions shown in Chapter 5, however as stated earlier in this Chapter these results should only be taken as an indicative example of what can be expected in such reaction vessel.

The mean settling velocity of the dispersed phase values are presented in Figure 6.27c. From the visualisation it can be seen that the *Simple-Varying* correlates with the field distributions observed in Figures 6.27a, 6.27b. This is a crucial difference between the original *Simple* model 3.38 where the variation of the parameter did not take into account the changes of size distribution of the dispersed phase as it was shown in Figure 6.24b. The settling velocity field reaches a largest value of $U_{dr,d} = 11\mu m$. Similar values have been observe in Chapter 5 and also have been reported in the literature.

The chemical state of the precipitation process can be evaluated by analysing the saturation state of the system. As it is shown in graphs 6.26 the rectant concentrations remain steady and show no significant variation. Same was observed for the saturation index which was used as an indicator in this part of study. The mean distribution of the saturation index is shown in Figure 6.27d. The largest values are observed at the left side of the visualisation where $SI = 1.66$, whereas the lowest values are observed in the central part of the tank with $SI = 0.14$. Although it is intuitive that the major reactive zones would be found on the outer wall of the vessel due to geometrical shape of the vessel and the flow patterns observed (as it was shown in Figure 6.21), it is now possible to better predict the state of the precipitation process due to the modelling framework used.

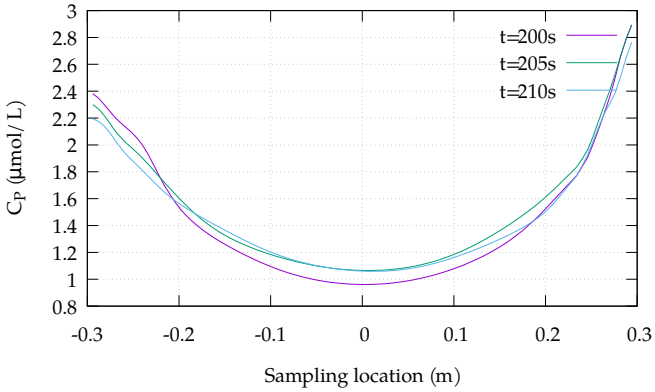

(a) C_P instantaneous samples

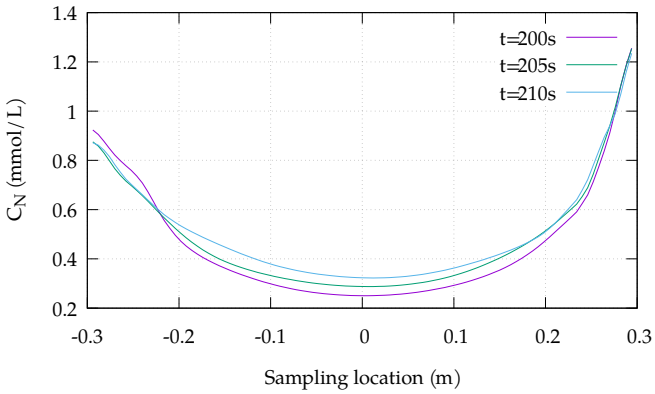

(b) C_N instantaneous samples

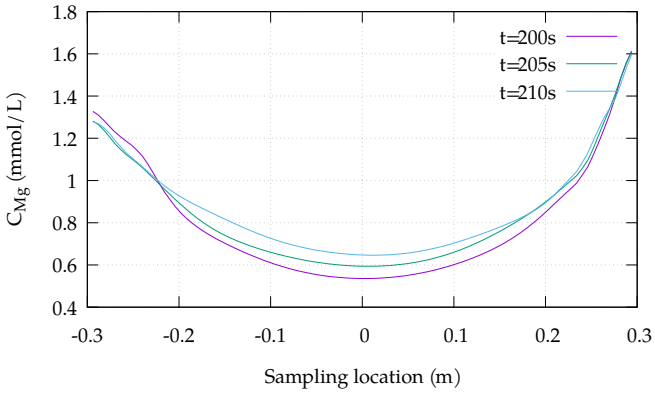

(c) C_{Mg} instantaneous samples

Figure 6.26: Line graphs of the concentrations of phosphorus, ammonia and magnesium ions along a horizontal sample line at $z = 0.4m$

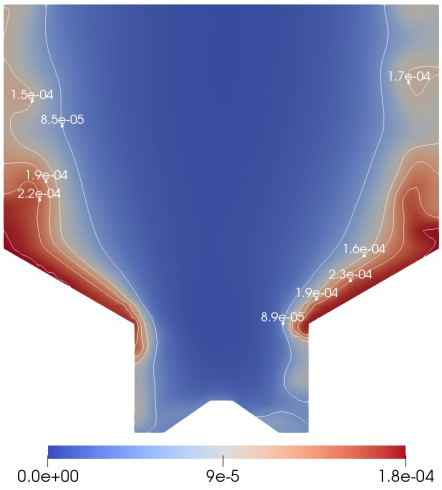

(a) α_d mean distribution

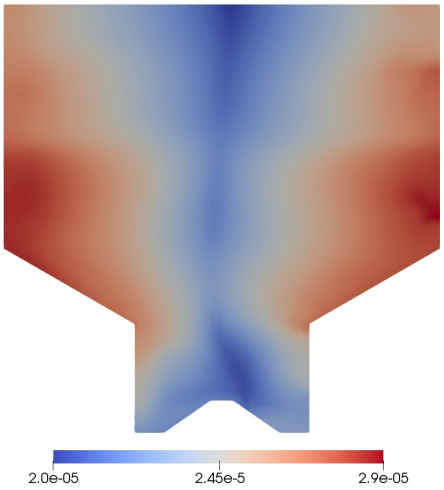

(b) d_{43} mean distribution

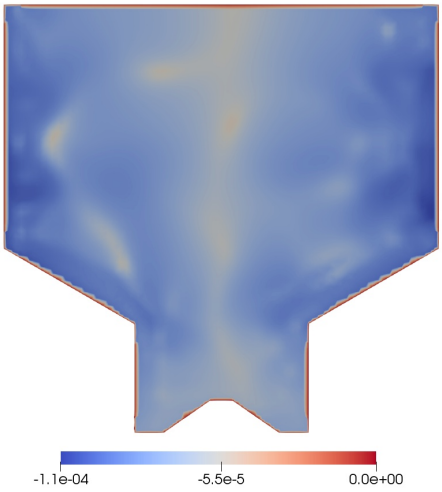

(c) $U_{dr,d}$ mean distribution

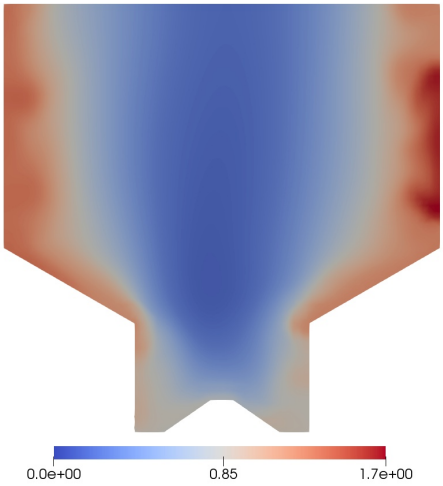

(d) SI mean distribution

Figure 6.27: Mean distributions of the dispersed phase volume fraction α, the Sauter mean diameter d_{43}, the settling velocity U_{dm} and the saturation index SI on a vertical slice at the middle of the vessel.

Underflow outlet section

The underflow outlet section is the solids recovery area of the separator tank. The solids forming in the main cylinder section of the separator are expected to eventually reach large enough terminal velocity values and therefore settle towards the underflow outlet part of the tank. The mean distribution of the flow field displayed in Figure 6.28 shows that the maximum values of the flow reach $U_m = 0.13m/s$. Hydrodynamically it corresponds to the values predicted in Section 6.2.2 and although the values differ it is only by a small margin therefore the hydrodynamic performance of the framework is deemed acceptable.

Figure 6.29 displays mean distributions of α_d and d_{43} at the underflow pipe section of the tank. The dispersed phase volume fraction at the underflow pipe reaches a maximum values of $\alpha_d = 8.8 \times 10^{-5}$ and the Sauter mean diameter values vary between $d_{43} = 22\mu m$ and $d_{43} = 24\mu m$. The volume fraction is seen to congretate along the right hand side wall of the underflow cylinder rather than being forced towards the outlet and this would require further investigation in the future in order to understand the reason for that. The mean diameter as previously mentioned in the section accurately predicts locations of the largest sized particles as it correlates with the largest volume fraction areas observed.

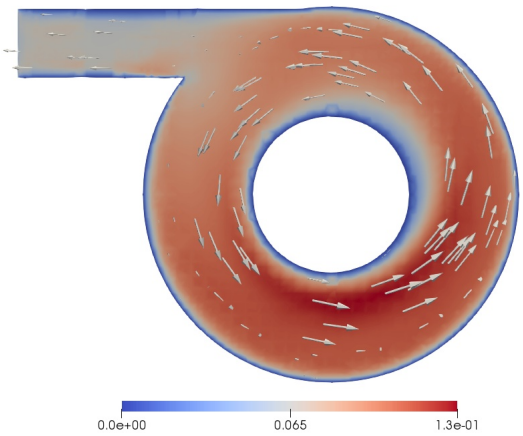

Figure 6.28: The distrubutions of the mean mixture velocity U_m at the mid-cross section of the underflow pipe area.

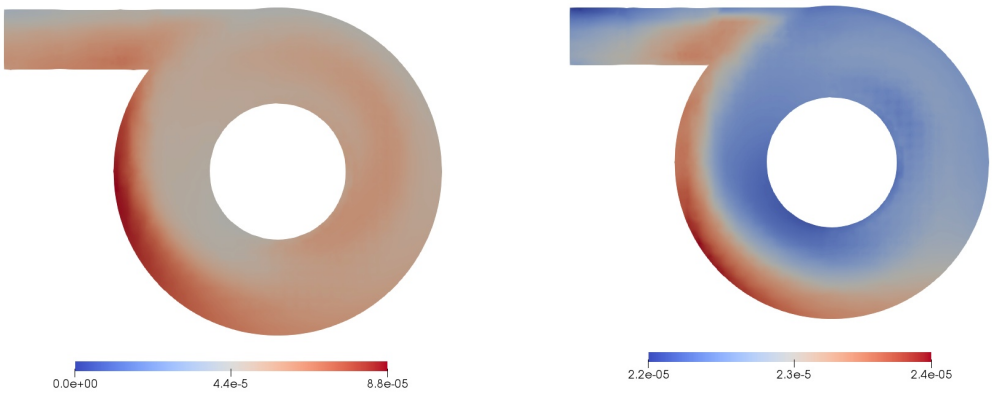

(a) α_d mean distribution

(b) d_{43} mean distribution

Figure 6.29: The dispersed phase volume fraction α_d and the Sauter mean diameter d_{43} distributions at the mid-cross section of the underflow pipe area.

Overflow section

Predictions from the overflow section of the tank presented in this section. The flow field predicted by the framework corresponds to the values shown in Section 6.1.2. The mean distribution of the mixture velocity U_m is shown in Figure 6.30.

The maximum value of the mean dispersed phase volume fraction is observed to be $\alpha_d = 1.7 \times 10^{-4}$ with the largest particle size of $d_{43} = 29\mu$m.

The mean struvite and phosphate concentrations have reached the values of $C^T_{MAP} =$ 1.1mM and $C^T_P = 3.2$mM respectively.

The time-averaged distributions of the dispersed phase volume fraction α_d, the Sauter mean diameter d_{43} and total concentrations of struvite and phosphorus respectively are shown Figures 6.31a, 6.31b, 6.31c and 6.31d.

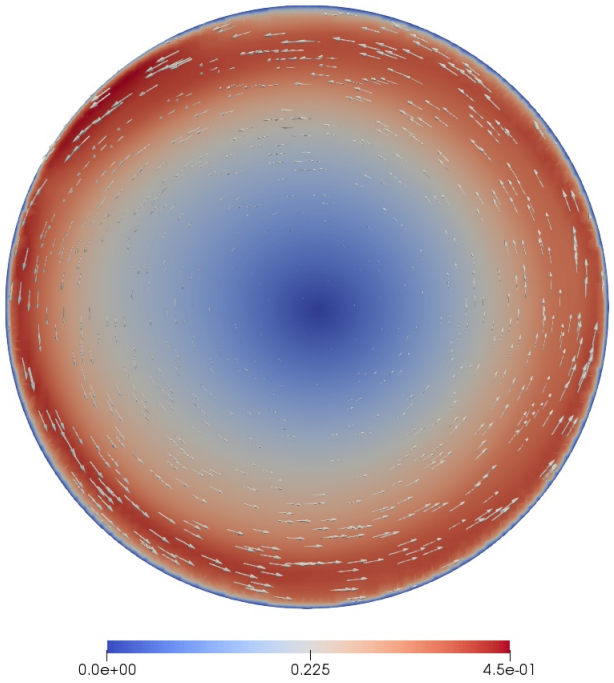

Figure 6.30: The mean distribution of the mixture velocity field U_m in the overflow section.

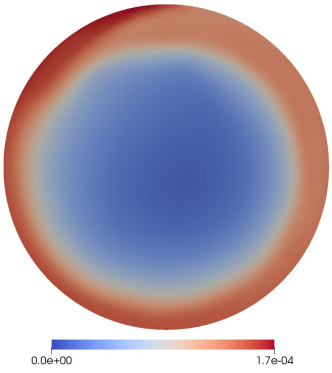

(a) α_d mean distribution

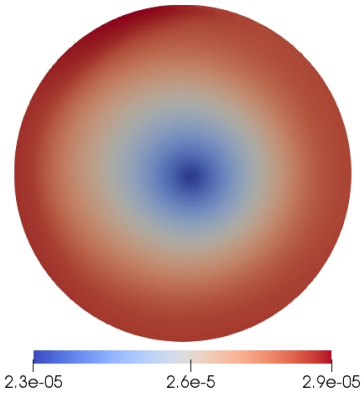

(b) d_{43} mean distribution

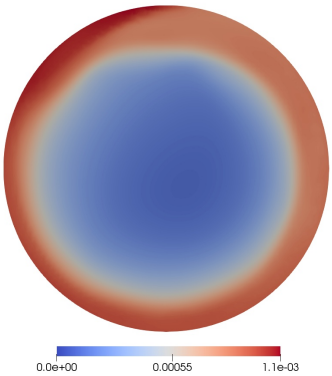

(c) C^T_{MAP} mean distribution

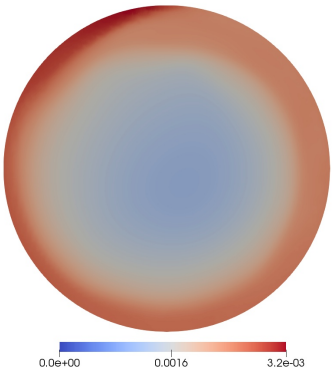

(d) C^T_P mean distribution

Figure 6.31: Distributions of the dispersed phase volume fraction α, the Sauter mean diameter d_{43}, the total concentration of struvite and the total concentration of phosphorus on a vertical slice near the underflow outlet pipe.

Discussion

The simulations presented throughout this section produced qualitatively and quantitavely reasonable results. The precipitation model simulation in Section 6.2.4 showed a large difference in distribution of the dispersed phase in the tank when compared to the multiphase simulations presented in Section 6.2.3 which did not consider precipitation kinetics. The variation of the dispersed phase mean diameters introduced in the precipitation model affects the settling velocity significantly and the distributions of the settling velocity shown in Figures 6.24b, 6.27c show these differences. In the multiphase simulations the dispersed phase settles down to the bottom of the tank where as the precipitation model predicts that most of the dispersed phase would congregate around the conical part of the tank. The settling velocity values in both of the simulations are different and therefore this is an indicator that the precipitation model requires further testing in order to establish the appropriate operational conditions of the tank which would optimise the precipitation process.

The conical part of the main cylinder can be identified as a crucial part of the separator tank. It is visible in Figure 6.27a that there is a significant accumulation of the dispersed phase in this region. The Sauter mean diameter also indicates that the largest particulate size is found in these parts of the main cylinder. Even though only a single set of operational conditions were tested in this study it is clear that further investigation has to be done in order to find the optimum loading rate of the system that would maximise the particulate size and settling.

Based on the level of saturation, other regions of the tank can be identified as important areas for struvite formation. The largest saturation areas in the tank are found on the outer wall, as shown by Figure 6.27d. This indicates that in this particular geometry the newly created particulates would then swirl around the tank starting from the outer wall. When the size of the particle reaches a settling limit it would then stop being neutrally buoyant and start settling down towards the conical part of the tank and further to the underflow. The saturation index is

observed to have reached a steady state value in the system.

Analysis of the underflow and overflow sections of the tank show that at this case setup dispersed phase exiting the system in the from the outlet at the underflow region is lower than the volume fractions of the dispersed phase exiting the system at the overflow outlet. This can be recitified through optimising the operational conditions of the tank, which would increase the levels of settling of the dispersed phase. It also has to be noted that for this case study due to intelectual property restrictions internal components often found in Hydrodynamic Vortex Separators have been removed. These internal components are designed to optimise solids removal from the tank, therefore without them it should be expected that the result would be suboptimal and therefore as stated at the start of this section these results should be viewed as a case study rather than a comprehensive analysis of the HDVS performance as a reaction vessel.

6.3 Assumptions and current limitations of the modelling framework

Modelling framework used in this study follows a set of fundamental assumptions on the physics of the systems being investigated. These allow the framework to be formulated however it creates a certain amount of limitations that have to be stated and made clear.

The drift flux mixture model presented in Section 3.2.2.3 formulates multiphase system in terms of conditionally averaged mixture parameters. As stated initially this allows the hydrodynamic state of the system to be calculated using a reduced set of equation as opposed to two fluid model presented in Section 3.2.2.2. The drawback however is that DFM does not explicitly model different physical aspects of the system,such as particle-fluid and particle-particle interactions. This limitation of the model is known, however the alternative would be much more computationally intensive and therefore would not be a feasible tool for research.

Chemical species transport modelling formulated in Section 3.3 follows an assumption that the reaction processes time-scales are of the same order as the fluid flow time-scales. This allows the saturation state of the system and subsequently the kinetic rates to be formulated in terms of equilibrium thermodynamics relationships described in Section 3.3.2. Even though the evidence in the literature exists, this might not be applicable to every precipitation process present in the world.

As discussed in Section 3.3.3 a complete description of the reaction kinetic mechanisms involved in struvite precipitation is something to be desired. Underlying strong first principles theories for each of the kinetic mechanisms (i.e. nucleation, growth, aggregation and breakup) are not available at the moment and therefore empirically fitted models are often used, as it has been done in this present study.

In order to formulate the kinetics used in this framework first it has been assumed that saturation levels in the systems that will be investigated will be high enough for the homogeneous primary nucleation process (i.e. nuclei apparition directly in the supersaturated solution) to be the most dominant. This excludes other nucleation regimes: heterogeneous primary nucleation and surface secondary nucleation. Both of the ommitted regimes would affect the rates of nucleation in the system and subsequently the amount and quality of the precipitant. At present date however, the literature suggests that homogeneous is the most dominant nucleation mechanism in struvite precipitation processes, nonetheless it is a known limitation of the model and should be revised if additional evidence becomes available.

Growth mechanisms of struvite preciptiation are not well understood and only limited amount of empirically fitted models are available. Different formulations have been tested in Chapter 5. The Galbraith kinetic model 5.4 was chosen under an assumption that the levels of the system that this modelling framework is aimed for would be high and therefore the growth rates are expected to be fast.

Available literature did not indicate that aggregation and breakup kinetic mechanisms are dominant in struvite precipitation, therefore it was assumed in this study that these mechanisms will not be modelled. However, if and When struvite precip-

itation process is better understood in the future these mechanisms might become important part of the process and therefore would require to be implemented in the framework in order to capture the physics appropriately.

6.4 Closure

The first part of the chapter was dedicated to the two-dimensional representation of the settling tank by Dahl [35]. The simulations were performed in accordance with the operational conditions used in the empirical tests. It has been demonstrated that the low velocity inflow operational conditions are better suited for precipitation processes in such settling tanks. Although empirical data is not available the results show some qualitative similarities between the results presented by Brennan [21]. The predicted Sauter mean diameter values were also deemed to be appropriate ($d_{43} = 22.46\mu$m for high velocity cases and $d_{43} = 14.95\mu$m for low velocity cases).

The model however, seemed to predict seemingly large dispersed phase volume fraction values. Over the course of the simulations α_d had reached values of up to 1.79×10^{-4}.

In the second part the hydrodynamic vortex separator was modelled under different numerical setups. The simulations predicted that the precipitated particles are able to reach particle sizes of $d_{43} = 29\mu$m. The simulations allowed the identification of crucial regions of the separator tank, however further investigation and empirical data is required to understand what precipitation kinetics are dominant in such geometries.

Chapter 7

Conclusions

The overall objective of this study was to develop an appropriate methodology together with the computational framework capable of modelling precipitation processes. This methodology was then applied to a set of test cases that aimed to test different aspects of the framework. A range of verification cases performed displayed that all parts of the framework work as it is expected, however no validation data was available and therefore the precipitation modelling framework requires more testing to evaluate it's capabilities and limitations.

This concluding chapter is divided into two sections. The first section provides a summary of the study, whereas the second section is dedicated to further research suggestions that would enhance the model performance.

7.1 Summary

In Chapter 2 the global phosphorus outlook was covered and the issues arising with the ever increasing scarcity of phosphorus in the world were reviewed. Further, the research behind phosphorus recovery from wastewater was reviewed. Different attempts at phosphorus recovery technologies were discussed and an overview of various methodologies that can be employed to recover phosphorus from wastewater was provided. Lastly a review of the modelling methodologies was provided. It

was concluded that the extended quadrature method of moments coupled with the mixture model to model the hydrodynamics was the best methodology for the current problem at hand. One of the major conclusions that have been made from the literature review was that there is no complete framework/computational toolset capable of handling three key physical aspects involved in precipitation processes: hydrodynamics, equilibrium thermodynamics of reactive crystallisation and evolution of the crystal size distributions due to precipitation kinetics involved.

The mathematical modelling aspects were presented in Chapter 3. An Eulerian approach was adopted in which the two phases are treated as interpenetrating continua. The two-fluids model described in the Chapter is shown to introduce unknown correlation terms that require closure models to be specified in order to obtain a solution. The two-fluid formulation requires momentum and continuity conservation equations to be solved for each phase independently which is not computationally efficient. A simplification of the model can be introduced, where the transport equations for the momentum and continuity are reformulated in terms of combined mixture variables which are based on the mixture center of mass. In the mixture model formulation the interphase terms that previously required closure do not need modelling any more and therefore the solution procedure is much less computationally intensive. In this study the drift flux mixture model formulation has been deemed as an appropriate formulation to model the hydrodynamic aspects of the flow.

Further in Chapter 3 the modelling procedures of the struvite precipitation processes were presented. The thermodynamic equilibrium modelling aspects of the struvite precipitation were presented in order to have a complete description of the process. The main challenge of struvite precipitation arises due to the fact that the properties of the dispersed phase are changing over time therefore, in order to account for these changes, population balance modelling methodologies were reviewed. Population balance modelling is a standard approach used in chemical engineering to model the evolution of the crystal size distribution, however in order to obtain the solution to the population balance equation simplifications are

required. Various different approaches have been developed over the years, however the quadrature method of moments was deemed to be the most appropriate methodology to use in this study due to its relative computational efficiency. The recently developed extended quadrature method of moments was therefore used throughout this study.

The numerical solution procedure is presented in Chapter 4. An overview of finite volume discretisation and the PISO solution algorithm was provided. These methodologies are industry standard approaches and therefore only a brief overview was provided of them. Further, the numerical aspects behind the extended quadrature method of moments were reviewed. The importance and the algorithms behind moment realizability were discussed in order to provide a complete description of the EQMOM procedure.

In order to verify the precipitation kinetics modelling part of the solver a one dimensional analysis was performed and presented in Chapter 5. First the results of idealised equilibrium thermodynamics cases were verified against the semi-analytical solutions. Even though the solver results showed small discrepancies it was deemed to have been acceptable and therefore that the precipitation kinetics modelling is working correctly. Further the effects of the appropriate thermodynamic equilibrium modelling were presented and it was shown how certain empirical kinetic models require extremely long times in order for the precipitation to occur.

The numerical simulation cases of the Dahl settling tank (Dahl [35]) and the hydrodynamic vortex separator were presented in Chapter 6. Predictions of the two dimensional numerical simulations of the horizontal settling tank showed how the precipitation processes are dependent on the operational conditions. The simulations with the higher operational flow rates that were named Case (1.a) and (1.b) prevented the development of any significant amount of precipitant at the bottom of the tank. Time-averaged results showed that volume fraction of the dispersed phase forms a thin layer of about $10cm$ in height. This layer corresponds to the largest values of particle sizes $d_{43} = 22.46\mu m$ and $d_{43} = 22.39\mu m$ for Cases (1.a)

and (1.b) respectively. On the other hand the low inflow velocity Cases (2.a) and (2.b) displayed much larger variations in the dispersed phase volume fractions. Even though the dispersed phase volume fraction values for both sets of cases are of the same order of magnitude the low inflow velocity Cases (2.a) and (2.b) predict that the dispersed phase starts affecting the hydrodynamics of the system and a recirculation zone is formed. It was initially expected that lower velocity test cases would predict larger sized particulates than it has been observed in Cases (1.a) and (1.b). This has not been the case as Sauter mean diameters d_{43} were observed to be $14.97\mu m$ and $14.95\mu m$ for Cases (2.a) and (2.b) respectively. Because only two operational setups were tested at this stage it is believed that under different inflow conditions the particulate size and concentrations can be maximised.

Over the course of this study particulate size dependent settling models have been proposed. Both models allowed the capture of the affects of changes in particle sizes in the system. The main observation that has been made in Chapter 6 was that in all cases it was evident that a double exponent settling model named *General-Varying* allows low volume fraction of non-settleable particulates to be modelled, wehereas the *Simple-Varying* settling velocity model did not exhibit any variation in low volume fraction regions.

The final set of simulations performed were aimed to model the precipitation process in the hydrodynamic vortex separator. The numerical simulation allowed to identify that one of the important regions in the tank is the conical section connecting the main cylindrical tank with the underflow part of the geometry. This region displayed congregation of dispersed phase volume fraction with the highest values of $\alpha_d = 1.7 \times 10^{-4}$. The dispersed phase mean diameter values were also predicted to be the highest at the same regions. Although these results show promise it has been observed that for this particular geometrical configuration the volume fraction values at the overflow section are larger than the values at the underflow section. As it has been discussed in Section 6.2.4 HDVS tanks contain a set of important internal components that maximise settling performance of the vessel. Without these internal components the vessel operates at sub-optimal conditions which is

the reason why the values of the volume fractions and mean particulate diameters are observed to be larger at the overflow region than at the underflow region. Due to intelectual property restrictions it was not possible to perform simulations and present results for a complete configuration of the HDVS.

At the start of this research project it has been established that there is a lack of a comprehensive CFD toolset tailored for precipitation processes. The majority of tools available were focussed towards one of the key physical aspects that govern the outcome of precipitation reactions (i.e. the hydrodynamics of the system, the equilibrium thermodynamics of ionic species and the population balance modelling). The framework built and presented throughout this thesis set out to combine these key physical aspects in order to model precipitation processes more accurately. The test cases presented in Chapters 5, 6 have shown that qualitatively good results. Even though additional work is required to further develop and test the framework it is deemed that this study successfully achieved the primary goal set out at the start of the project.

7.2 Suggestions for Further Research

Throughout this study a set of precipitation kinetic mechanisms were investigated, however due to the lack of empirical data available it is not currently known whether these mechanisms would appropriately represent the precipitation processes in the hydrodynamic vortex separator. In the future it is highly recommended to perform experimental studies that would help to identify the kinetic parameters and the mechanisms that would be involved.

The drift flux mixture model that was initially deemed to be a viable choice for modelling the hydrodynamics of the system does suffer from certain limitations. The resolution of the relative motion between phases is lost, due to the removal of the interphase drag terms in the equation set. Even though the drift flux model is less computationally expensive the assumptions made should be investigated further and therefore tailored for the systems where the dispersed phase properties,

such as the mean diameter of the particulates, are changing over time. The two-fluid formulation even though more computationally expensive would provide additional and crucial information about the interphase behaviour of the system and would allow the system to be modelled more completely.

In this study the variation of the pH in the system was kept constant, however during the struvite precipitation it is known that there is a release of the H^+ ions into the system, which in turn affects the level of the pH. In order to capture the reaction process more appropriately it would be necessary to add the variation of the acidity of the system, which would allow the model to be validated against the experimental data more appropriately.

One of the major limitations of the current formulation was observed to have been the time required to obtain the solution. On a 28 core workstation with 251GB of RAM, the 250000 cells mesh resolution case required two weeks of execution time in order to reach 107 seconds of simulation time. For cases of higher resolution the execution time would mean that the model use is not viable for any realistic cases. The observation has been also made that the solution procedure of the moments transport equations required significant amount of run-time and was observed to be very sensitive to the Courant-Friedrichs-Lewy condition values. All of the transport equations in the formulation were solved in a segregated manner which requires the equations to be solved sequentially. An alternative, namely the block-coupled solution procedure, is known to produce significantly quicker convergence rates and therefore the simulation run-times are reduced significantly (Darwish et al. [36], Deng et al. [39], Moukalled and Darwish [95], Webster [135]). The main idea behind the coupled procedure relies on the notion that the transport equations can combined into a single matrix and therefore the solution obtained is more accurate and requires very little under-relaxation in order to obtain a converged result. In the future it is a recommendation to formulate the CFD solver with an implementation of the block-coupled solution procedure.

Appendix A

Derivation of the semi-analytical equations

This appendix provides derivations of the 4th order ODE equations representing the change of reactant concentration in the system. Analytical solutions are still too difficult to obtain, therefore MATLAB is used to numerically solve the ODEs.

A.1 Galbraith

Assuming that the concentrations of reactants in the solution have the same initial concentrations (i.e. $C_i = C$ the rate of change of concentration is defined in Equation A.1, the rates of change for the first three moments are defined in Equations A.4, A.3, A.2.

$$\frac{\mathrm{d}C}{\mathrm{d}t} = -k_v \frac{\rho_d}{W_d} \frac{\mathrm{d}\mu_3(\mathbf{x},t)}{\mathrm{d}t} = -3k_v C_g \frac{\rho_d}{W_d} S_I^{N_g} \mu_2 \equiv -K S_I^{N_g} \mu_2 \tag{A.1}$$

$$\frac{\mathrm{d}\mu_2}{\mathrm{d}t} = 2C_g S_I^{N_g} \mu_1 \tag{A.2}$$

$$\frac{\mathrm{d}\mu_1}{\mathrm{d}t} = C_g S_I^{N_g} \mu_0 \tag{A.3}$$

$$\frac{\mathrm{d}\mu_0}{\mathrm{d}t} = C_j S_I^{N_j} \tag{A.4}$$

where k_v is volume based shape factor; ρ_d and W_d are the density and molar weight of the solid phase; C_g and C_j are the growth and nucleation rate constants respec-

tively; N_g and N_j are the the growth and nucleation rate exponents respectively.

For simplicity it is assumed that the species solution is ideal (i.e. the ionic activity coefficients $\gamma_i = \gamma = 1$). Together with the aforementioned assumption that $C_i = C$, the saturation index is as follows:

$$S_I = \log_{10}\left(\frac{\prod_i \gamma_i C_i}{K_{SP}}\right) = \log_{10}\left(\frac{\gamma^3 C^3}{K_{SP}}\right) \equiv \log_{10}\left(\alpha C^3\right) \tag{A.5}$$

For simplicity dot notation will be used to denote derivatives w.r.t. time throughout the rest of the derivation.

From Equation A.1 the second moment is:

$$\mu_2 = -\frac{1}{K}\frac{\dot{C}}{S_I^{N_g}} \tag{A.6}$$

Taking the derivative w.r.t. time and using equation A.2 the following expression for μ_1 is obtained:

$$\mu_1 = -\left(\frac{1}{2KC_g}\right)\left[\frac{1}{S_I^{2N_g}}\ddot{C} - \frac{3N_g}{\ln(10)}\frac{1}{C(S_I)^{2N_g+1}\dot{C}}\right] \tag{A.7}$$

Taking derivative w.r.t. time and using Equation A.3 the following expression for μ_0 is obtained:

$$\mu_0 = -\left(\frac{1}{2KC_g^2}\right)\left[\frac{\dddot{C}}{S_I^{3N_g}} - \frac{12N_g}{\ln(10)}\frac{\dot{C}\ddot{C}}{C(S_I)^{3N_g+1}} + \frac{3N_g}{\ln(10)}\frac{\dot{C}^3}{C(S_I)^{3N_g+1}} + \frac{9N_g(2N_g+1)}{\ln^2(10)}\frac{\dot{C}^3}{C^2(S_I)^{3N_g+2}}\right]$$

After the final differentiation w.r.t. time the final 4th order equation is obtained:

$$\frac{\mathrm{d}^4C}{\mathrm{d}t^4} = A_1\left(\frac{\mathrm{d}C}{\mathrm{d}t}\right)^4 + A_2\left(\frac{\mathrm{d}C}{\mathrm{d}t}\right)\left(\frac{\mathrm{d}^3C}{\mathrm{d}t^3}\right) - A_3\left(\frac{\mathrm{d}C}{\mathrm{d}t}\right)^2\left(\frac{\mathrm{d}^2C}{\mathrm{d}t^2}\right) + A_4\left(\frac{\mathrm{d}^2C}{\mathrm{d}t^2}\right)^2 - A5; \tag{A.8}$$

$$A1 = (\frac{6N_g}{\log(10)S_I}) + \frac{9N_g(7N_g+3)}{\log^2(10)S_I^2} + \frac{27N_g(2N_g+1)(3N_g+2)}{\log^3(10)S_I^3}$$
$$A2 = \frac{21N_g}{\log(10)S_I}$$
$$A3 = \frac{21N_g}{\log(10)S_I} + \frac{9N_g(18N_g+7)}{\log^2(10))S_I^2}$$
$$A4 = \frac{12N_g}{\log(10)S_I}$$
$$A5 = 6k_v C_g^3 C_j \left(\frac{\rho_d}{W_d}\right) S_I^{(3N_g+N_j)}$$

A.2 Hanhoun

Assuming that the concentrations of reactants in the solution have the same initial concentrations (i.e. $C_i = C$ the rate of change of concentration is defined in Equation A.9, the rates of change for the first three moments are defined in Equations A.12, A.11, A.10.

$$\frac{\mathrm{d}C}{\mathrm{d}t} = -k_v \frac{\rho_d}{W_d} \frac{\mathrm{d}\mu_3(\mathbf{x},t)}{\mathrm{d}t} = -3k_v C_g \frac{\rho_d}{W_d} S^{N_g}\mu_2 \equiv -K^{-1}S_g^N \mu_2 \tag{A.9}$$
$$\frac{\mathrm{d}\mu_2}{\mathrm{d}t} = 2C_g S^{N_g}\mu_1 \tag{A.10}$$
$$\frac{\mathrm{d}\mu_1}{\mathrm{d}t} = C_g S^{N_g}\mu_0 \tag{A.11}$$
$$\frac{\mathrm{d}\mu_0}{\mathrm{d}t} = A\exp\left(-\frac{B}{\ln^2\Omega}\right) \tag{A.12}$$

where k_v is volume based shape factor; ρ_d and W_d are the density and molar weight of the solid phase; C_g and A are the growth and nucleation rate constants respectively N_g and N_j are the the growth and nucleation rate exponents respectively; B is nucleation activation constant; S and Ω absolute saturation and supersaturation respectively.

For simplicity it is assumed that the species solution is ideal (i.e. the ionic activity coefficients $\gamma_i = \gamma = 1$). Together with the aforementioned assumption that $C_i =$

C, the absolute saturation and the supersaturation ratio are as follows:

$$S = \left(\prod_i \gamma_i C_i\right)^{1/3} - K_{sp}^{1/3} = \gamma C - K_{sp}^{1/3} \tag{A.13}$$

$$\Omega = \frac{\prod_i \gamma_i C}{K_{sp}} = \frac{\gamma^3 C^3}{K_{sp}} \equiv \alpha C^3 \tag{A.14}$$

Using equation A.9 μ_2 is defined as:

$$\mu_2 = -K \frac{\dot{C}}{S^{N_g}} \tag{A.15}$$

Taking the derivative w.r.t. time, using A.10 and rearranging expression for μ_1 is:

$$\mu_1 = -\left(\frac{K}{2C_g}\right)\left[\frac{\ddot{C}}{S^{2N_g}} - \gamma N_g \frac{\dot{C}^2}{S^{2N_g+1}}\right] \tag{A.16}$$

Following the procedure the μ_0 is expressed as:

$$\mu_0 = -\left(\frac{K}{2C_g^2}\right)\left[\frac{\dddot{C}}{S^{3N_g}} - 4\gamma N_g \frac{\ddot{C}\dot{C}}{S^{3N_g+1}} + \gamma^2 N_g(2N_g+1)\frac{\dot{C}^3}{S^{3N_g+2}}\right]$$

After the final repeat of time derivation and substitution of Equation A.12 - 4th order ODE is obtained:

$$\frac{\mathrm{d}^4 C}{\mathrm{d}t^4} = A_1\left(\frac{\mathrm{d}C}{\mathrm{d}t}\right)^4 + A_2\left(\frac{\mathrm{d}C}{\mathrm{d}t}\right)\left(\frac{\mathrm{d}^3 C}{\mathrm{d}t^3}\right) - A_3\left(\frac{\mathrm{d}C}{\mathrm{d}t}\right)^2\left(\frac{\mathrm{d}^2 C}{\mathrm{d}t^2}\right) + A_4\left(\frac{\mathrm{d}^2 C}{\mathrm{d}t^2}\right)^2 - A_5 \tag{A.17}$$

$$A_1 = \frac{N_g \gamma^3 (2N_g+1)(3N_g+2)}{S^3}; \tag{A.18}$$

$$A_2 = \frac{7N_g\gamma}{S}; \tag{A.19}$$

$$A_3 = \frac{N_g \gamma^2 (18N_g+7)}{S^2}; \tag{A.20}$$

$$A_4 = \frac{4N_g\gamma}{S}; \tag{A.21}$$

$$A_5 = 6k_v C_g^3 A \frac{\rho_d}{Ws} S^{3N_g} \exp\left(-\frac{B}{\log_{10}^2(\Omega)}\right). \tag{A.22}$$

A.3 Ye

Using the same assumptions mentioned in the earlier sections of this appendix, the following equations are declared:

$$\frac{\mathrm{d}C}{\mathrm{d}t} = -k_v \frac{\rho_d}{W_d} \frac{\mathrm{d}\mu_3(\mathbf{x},t)}{\mathrm{d}t} = -0.5 k_v C_g \frac{\rho_d}{W_d} S^{N_g} \mu_2 \equiv -K^{-1} S_g^N \mu_2 \tag{A.23}$$

$$\frac{\mathrm{d}\mu_2}{\mathrm{d}t} = 2 C_g S^{N_g} \mu_1 \tag{A.24}$$

$$\frac{\mathrm{d}\mu_1}{\mathrm{d}t} = C_g S^{N_g} \mu_0 \tag{A.25}$$

$$\frac{\mathrm{d}\mu_0}{\mathrm{d}t} = C_j S_I^{N_j} \tag{A.26}$$

$$S = \left(\prod_i \gamma_i C_i\right)^{1/3} - K_{sp}^{1/3} = \gamma C - K_{sp}^{1/3} \tag{A.27}$$

$$S_I = \log_{10}\left(\frac{\prod_i \gamma_i C_i}{K_{sp}}\right) = \log_{10}\left(\frac{\gamma^3 C^3}{K_{sp}}\right) \equiv \log_{10}\left(\alpha C^3\right) \tag{A.28}$$

where k_v is volume based shape factor; ρ_d and W_d are the density and molar weight of the solid phase; C_g and C_J are the growth and nucleation rate constants respectively N_g and N_j are the the growth and nucleation rate exponents respectively; S and S_I absolute saturation and saturation index respectively. Using Equation A.23 μ_2 is defined as:

$$\mu_2 = -K \frac{\dot{C}}{S^{N_g}} \tag{A.29}$$

Taking the derivative w.r.t. time, using A.24 and rearranging expression for μ_1 is:

$$\mu_1 = -\left(\frac{K}{2C_g}\right)\left[\frac{\ddot{C}}{S^{2N_g}} - \gamma N_g \frac{\dot{C}^2}{S^{2N_g+1}}\right] \tag{A.30}$$

Following the procedure the μ_0 is expressed as:

$$\mu_0 = -\left(\frac{K}{2C_g^2}\right)\left[\frac{\dddot{C}}{S^{3N_g}} - 4\gamma N_g \frac{\ddot{C}\dot{C}}{S^{3N_g+1}} + \gamma^2 N_g(2N_g+1)\frac{\dot{C}^3}{S^{3N_g+2}}\right]$$

The final expression of the ODE is:

$$\frac{\mathrm{d}^4 C}{\mathrm{d}t^4} = A_1\left(\frac{\mathrm{d}C}{\mathrm{d}t}\right)^4 + A_2\left(\frac{\mathrm{d}C}{\mathrm{d}t}\right)\left(\frac{\mathrm{d}^3 C}{\mathrm{d}t^3}\right) - A_3\left(\frac{\mathrm{d}C}{\mathrm{d}t}\right)^2\left(\frac{\mathrm{d}^2 C}{\mathrm{d}t^2}\right) + A_4\left(\frac{\mathrm{d}^2 C}{\mathrm{d}t^2}\right)^2 - A_5 \tag{A.31}$$

$$A_1 = \frac{N_g\gamma^3(2N_g+1)(3N_g+2)}{S^3}; \tag{A.32}$$

$$A_2 = \frac{7N_g\gamma}{S}; \tag{A.33}$$

$$A_3 = \frac{N_g\gamma^2(18N_g+7)}{S^2}; \tag{A.34}$$

$$A_4 = \frac{4N_g\gamma}{S}; \tag{A.35}$$

$$A_5 = (k_v C_g^3 C_j)\frac{\rho_d}{W_d} S^{3N_g} S_I^{N_j}. \tag{A.36}$$

Appendix B

Derivation of ion concentration formulas

Different compounds form in a solution of water, therefore it is important to take that into account when calculating the molar concentrations of the ions that participate in struvite precipitation and the level of the supersaturation of the ionic solution. The derivation procedure for this takes into account all of the possible compounds in the water solution of magnesium, phosphorus and nitrogen as reported by the literature. The starting point of the procedure is to recall the mole balance equations 3.72, 3.73, 3.74 as defined in Section 3.3.2:

$$\begin{aligned} C_P^T &= [H_3PO_4] + [H_2PO_3^-] + [HPO_4^{2-}] + [PO_4^{3-}] + [MgH_2PO_4^+] \\ &\quad + [MgHPO_4] + [MgPO_4^-] \end{aligned} \tag{B.1}$$

$$C_{Mg}^T = [Mg^{2+}] + [MgOH^+] + [MgH_2PO_4^+] + [MgHPO_4] + [MgPO_4^-] \tag{B.2}$$

$$C_N^T = [NH_3] + [NH_4^+] \tag{B.3}$$

Also recall the corresponding equilibrium constants for all of the compounds formed that have been defined in Equations 3.54 - 3.63:

$$MgOH^+ \xleftrightarrow{K_{MgOH^+}} Mg^{2+} + OH^-; \quad K_{MgOH^+} = \frac{\{Mg^{2+}\}\{OH^-\}}{\{MgOH^+\}}$$

$$MgHPO_{4(aq)} \xleftrightarrow{K_{MgHPO_4}} Mg^{2+} + {HPO_4}^{2-}; \quad K_{MgHPO_4} = \frac{\{Mg^{2+}\}\{{HPO_4}^{2-}\}}{[MgHPO_{4(aq)}]}$$

$$
\begin{aligned}
\mathrm{MgH_2PO_4^+} &\xleftrightarrow{\mathrm{K_{MgH_2PO_4^-}}} \mathrm{Mg^{2+} + H_2PO_4^-}; & \mathrm{K_{MgH_2PO_4^+}} &= \frac{\{\mathrm{Mg^{2+}}\}\{\mathrm{H_2PO_4^-}\}}{\{\mathrm{MgH_2PO_4^+}\}} \\
\mathrm{MgPO_4^-} &\xleftrightarrow{\mathrm{K_{MgPO_4^-}}} \mathrm{Mg^{2+} + PO_4^{3-}}; & \mathrm{K_{MgPO_4^-}} &= \frac{\{\mathrm{Mg^{2+}}\}\{\mathrm{PO_4^{3-}}\}}{\{\mathrm{MgPO_4^-}\}} \\
\mathrm{H_3PO_{4(aq)}} &\xleftrightarrow{\mathrm{K_{H_3PO_4}}} \mathrm{H^+ + H_2PO_4^-}; & \mathrm{K_{HPO_4^{2-}}} &= \frac{\{\mathrm{H^+}\}\{\mathrm{PO_4^{3-}}\}}{[\mathrm{HPO_4^{2-}}]} \\
\mathrm{NH_4^+} &\xleftrightarrow{\mathrm{K_{NH_4^+}}} \mathrm{H^+ + NH_3}; & \mathrm{K_{H_2PO_4}} &= \frac{\{\mathrm{H^+}\}\{\mathrm{HPO_4^{2-}}\}}{[\mathrm{H_2PO_4^-}]} \\
\mathrm{HPO_4^{2-}} &\xleftrightarrow{\mathrm{K_{HPO_4^{2-}}}} \mathrm{H^+ + PO_4^{3-}}; & \mathrm{K_{H_3PO_4}} &= \frac{\{\mathrm{H^+}\}\{\mathrm{H_2PO_4^-}\}}{[\mathrm{H_3PO_{4(aq)}}]} \\
\mathrm{H_2PO_4^-} &\xleftrightarrow{\mathrm{K_{H_2PO_4^-}}} \mathrm{H^+ + HPO_4^{2-}}; & \mathrm{K_{NH_4^+}} &= \frac{\{\mathrm{H^+}\}[\mathrm{NH_3}]}{\{\mathrm{NH_4{}^+}\}} \\
\mathrm{H_2O} &\xleftrightarrow{\mathrm{K_{H_2O}}} \mathrm{H^+ + OH^-}; & \mathrm{K_{H_2O}} &= \frac{\{\mathrm{H^+}\}\{\mathrm{OH^-}\}}{[\mathrm{H_2O}]} \\
\gamma_{H^+}[\mathrm{H^+}] &= 10^{-\mathrm{pH}}
\end{aligned}
$$

Equilibrium equations can be rearranged as follows:

$$
\begin{aligned}
[\mathrm{MgOH^+}] &= \frac{\gamma_{\mathrm{Mg^{2+}}}\{\mathrm{OH^-}\}}{\gamma_{\mathrm{MgOH^+}} K_{\mathrm{MgOH^+}}}[\mathrm{Mg^{2+}}] \\
[\mathrm{MgPO_4^-}] &= \frac{\gamma_{\mathrm{PO_4^{3-}}}\gamma_{\mathrm{Mg^{2+}}}}{\gamma_{\mathrm{MgPO_4^-}} K_{\mathrm{MgPO_4^-}}}[\mathrm{Mg^{2+}}][\mathrm{PO_4^{3-}}] \\
[\mathrm{MgHPO_4}] &= \frac{\gamma_{\mathrm{Mg^{2+}}}\gamma_{\mathrm{PO_4^{3-}}}\{\mathrm{H}\}}{\gamma_{\mathrm{MgHPO_4}} K_{\mathrm{MgHPO_4}} K_{\mathrm{HPO_4^{2-}}}}[\mathrm{Mg^{2+}}][\mathrm{PO_4^{3-}}] \\
[\mathrm{MgH_2PO_4^+}] &= \frac{\gamma_{\mathrm{Mg^{2+}}}\gamma_{\mathrm{PO_4^{3-}}}\{\mathrm{H}\}^2}{\gamma_{\mathrm{MgH_2PO_4^+}} K_{\mathrm{MgH_2PO_4^+}} K_{\mathrm{H_2PO_4^-}} K_{\mathrm{HPO_4^{2-}}}}[\mathrm{Mg^{2+}}][\mathrm{PO_4^{3-}}] \\
[\mathrm{HPO_4^{2-}}] &= \frac{\gamma_{\mathrm{PO_4^{3-}}}\{\mathrm{H}\}}{\gamma_{\mathrm{HPO_4^{2-}}} K_{\mathrm{HPO_4^{2-}}}}[\mathrm{PO_4^{3-}}] \\
[\mathrm{H_2PO_4^-}] &= \frac{\gamma_{\mathrm{PO_4^{3-}}}\{\mathrm{H}\}^2}{K_{\mathrm{H_2PO_4^-}} K_{\mathrm{HPO_4^{2-}}}}[\mathrm{PO_4^{3-}}] \\
[\mathrm{H_3PO_4}] &= \frac{\gamma_{\mathrm{PO_4^{3-}}}\{\mathrm{H}\}^3}{K_{\mathrm{H_3PO_4}} K_{\mathrm{H_2PO_4^-}} K_{\mathrm{HPO_4^{2-}}}}[\mathrm{PO_4^{3-}}] \\
[\mathrm{NH_4^+}] &= \frac{\{\mathrm{H}\}}{\gamma_{\mathrm{NH_4^+}}}[\mathrm{NH_3}]
\end{aligned}
$$

Rearranging the mole balance equations in terms of the $[PO_4^{3-}]$, $[Mg^{2+}]$, $[NH_4^+]$ and substituting equilibrium relationships, the following expressions can be obtained:

$$C_P^T = K_0[PO_4^{3-}] + K_1[Mg^{2+}][PO_4^{3-}] \quad (B.4)$$

$$C_{Mg}^T = K_2[Mg^{2+}] + K_1[Mg^{2+}][PO_4^{3-}] \quad (B.5)$$

$$C_N^T = K_3[NH_4^+] \quad (B.6)$$

where the constants K_0, K_1, K_2, K_3 are as follows:

$$K_0 = \left(\left(\frac{\{H\}^3}{K_{H_3PO_4}K_{H_2PO_4^-}K_{HPO_4^{2-}}} + \frac{\{H\}^2}{K_{H_2PO_4^-}K_{HPO_4^{2-}}} + \frac{\{H\}}{K_{HPO_4^{2-}}}\right)\gamma_{PO_4^{3-}} + 1\right)$$

$$K_1 = \left(\frac{G_1\{H\}^2}{K_{MgH_2PO_4^+}K_{H_2PO_4^-}K_{HPO_4^{2-}}} + \frac{G_2\{H\}}{K_{MgHPO_4}K_{HPO_4^{2-}}} + \frac{G_3}{K_{MgPO_4^-}}\right)\gamma_{PO_4^{3-}}\gamma_{Mg^{2+}}$$

$$K_2 = \frac{\gamma_{Mg^{2+}}\{OH^-\}}{K_{MgOH^+}} + 1$$

$$K_3 = \frac{\gamma_{NH_4^+}K_{NH_4^+}}{\{H\}} + 1$$

with constants G_i being defined below.

$$G_1 = \frac{1}{\gamma_{MgH_2PO_4^+}}$$

$$G_2 = \frac{1}{\gamma_{MgHPO_4}}$$

$$G_3 = \frac{1}{\gamma_{MgPO_4^-}}$$

Rearranging equations B.4, B.5, B.6 and solving for ion concentrations the following final relationships are derived:

$$[Mg^{2+}] = \frac{(K_1C_{Mg}^T - K_A - K_1C_P^T) + \sqrt{(K_1C_{Mg}^T - K_A - K_1C_P^T)^2 + 4K_BC_{Mg}^T}}{2K_1K_2}$$

$$[PO_4^{3-}] = \frac{C_P^T}{K_0 + K_1[Mg^{2+}]}$$

$$[NH_4^+] = \frac{C^T}{K_3}$$

with K_A and K_B defined as follows:

$$K_A = K_0K_2$$

$$K_B = K_0K_1K_2$$

Equilibrium ionic concentration formulas are now derived and can be used to calculate the amounts of reactants that participate in struvite reaction.

Appendix C

Online repository for mapFoam solver and test cases

Struvite precipitation modelling framework has been uploaded to an online repository and is open for public access. Currently the release is marked as being in beta version and some additional development will be done as the time goes in order to make the code as clear as possible and to add necessary documentation for those who are interested in using it.

The repository also contains the semi analytical verification cases used in Chapter 5 and 2-dimensional Dahl settling tank cases used in Section 6.1. Due to intelectual property restrictions three dimensional cases used in Section 6.2 were not uploaded.

Please find the repository in the following repository: `https://doi.org/10.5281/zenodo.2927168`. Please use the DOI provided when citing the project.

Appendix D

2D Dahl case numerical setup

Details on the numerical setup of the two dimensional Dahl case are presented in this appendix. The information provided should be sufficient for someone willing to replicate the work. In addition to that a working set of cases have been uploaded to an online repository together with the solver and can be found under the following address: `https://doi.org/10.5281/zenodo.2927168`.

Summary of Boundary Conditions

In this study, different types of boundary conditions were which are presented in Tables D.1, D.2.

Inlet

The velocity fields are supplied at the inlet and the values were set to $(0.0191; 0; 0)$ for Cases 1 and $(0.0054; 0; 0)$ for Cases 2 as discussed in Section 6.1. The modified pressure $\overline{p}$ is set to fixed flux pressure boundary condition for consistency. Additionally the turbulent statistics parameters were set based on a nominal 10% turbulent intensity value.

It was assumed that no solids fraction were present in the system or will be entering the system, therefore the volume fraction was set to a fixed value 0. Simlarly this assumption implies that the statistical moments will be set to zero at the inlet.

The mass fractions of the chemical species were based on the required total concentration for each species which was 0.001M. This corresponds to the following values: phosphate mass fraction $Y_{PO4} = 9.53528 \times 10^{-5}$; magnesium mass fraction $Y_{Mg} = 2.44026 \times 10^{-5}$; ammonia mass fraction $Y_{NH4} = 1.81109 \times 10^{-5}$.

Outlet

The modified pressure field value at the outlet was supplied and a pressure inlet-outlet boundary condition is used for the velocity field. Inlet-outlet boundary conditions are commonly used in multiphase flows in order to truncate unrealisting backwash values that would obscure the results, therefore for the rest of the field either inlet-outlet boundary condition was used or zero gradient.

Bottom and end walls

The value of the mixture velocity at the walls was specified as no-slip (i.e. fixed value of (0 0 0)). The modified pressure was set to fixed flux pressure of specified value 0.

The rest of the parameters were set to a zero gradient boundary condition.

Slip top wall

Velocity field at the top wall of the geometry was specified as a slip boundary condition (i.e. normal component is set to fixed value of 0 and the tangential component of the field is set to a zero gradient condition). The modified pressure as previously was set to fixed flux pressure boundary condition with a value set to 0.

The rest of the parameters were set to a slip boundary condition.

Table D.1: Boundary conditionsl of the flow variables.

Parameter	Inlet	Outlet	Top	Walls
U_m	Fixed Value	Pressure Inlet-Outlet	Slip	No Slip
ε	Fixed Value	Inlet-Outlet	Slip	ε Wall Function
κ	Fixed Value	Inlet-Outlet	Slip	κ Wall Function
ν_t	Calculated	Calculated	Slip	ν_t Wall Function
$\overline{p}$	Fixed Flux Pressure	Fixed Value	Fixed Flux Pressure	Fixed Flux Pressure
α	Fixed Value	Inlet-Outlet	Slip	Zero Gradient

Table D.2: Boundary conditions of the chemical species Y_i and statistical moments μ_i.

Parameter	Inlet	Outlet	Top	Walls
Y_{PO4}	Fixed Value	Inlet-Outlet	Slip	Zero Gradient
Y_{Mg}	Fixed Value	Inlet-Outlet	Slip	Zero Gradient
Y_{NH4}	Fixed Value	Inlet-Outlet	Slip	Zero Gradient
μ_i	Fixed Value	Inlet-Outlet	Slip	Zero Gradient

Numerical schemes

Discretisation schemes used in 2D Dahl case are summarised in Figure D.1. Where solver allowed second order discretisation schemes were used. Due to the complexity of the problem the terms involving statistical moments were discretised using first order upwind schemes in order to achieve solver stability. This has been noted and will be investigated further in the future, therefore the sensitivity of the solver should be decreased in future code releases.

Model parameters

The following Figures D.2 D.3, D.4, D.5, D.6 provide all model parameters required to replicate the test study. Population balance modelling parameters are specified in Figure D.2. Quadrature solution algorithm specification is provided in Figure D.3. Parameters related to transport of fluid and dispersed phase as well as details on chemical species equilibrium thermodynamics are stated in Figure D.4. Lastly Figures D.5, D.6 provides parameters used in modelling precipitation process in this test case.

Details provided should be sufficient for someone trying to replicate the study, nonetheless as mentioned at the start of this appendix the test cases have been uploaded and made public on an online repository, which should provide any additional details that could have been missed out.

```
ddtSchemes
{
    default Euler;
}

gradSchemes
{
    default         Gauss linear;
    grad(p)         Gauss linear;
}

divSchemes
{
    default                                     none;

    div(rhoPhi,U)                               Gauss linearUpwind grad(U);
    div(tauDm)                                  Gauss linear;
    "div\(phi,alpha.*\)"                        Gauss vanLeer;
    "div\(phirb,alpha.*\)"                      Gauss linear;
    div(rhoPhi,k)                               Gauss limitedLinear 1;
    div(rhoPhi,epsilon)                         Gauss limitedLinear 1;
    div(phi,Yi)                                 Gauss limitedLinear 1;
    div(((rho*nuEff)*dev2(T(grad(U)))))         Gauss linear;
    div(phi,moment)                             Gauss upwind;
}

laplacianSchemes
{
    default                                     Gauss linear corrected;
    laplacian(muEff,U)                          Gauss linear corrected;
    laplacian(muEff,ft)                         Gauss linear corrected;
    laplacian(muEff,fu)                         Gauss linear corrected;
    laplacian(((alphah*mut)+alpha),h)           Gauss linear corrected;
    laplacian((rho|A(U)),p)                     Gauss linear corrected;
    laplacian(rhoD,k)                           Gauss linear corrected;
    laplacian(rhoD,epsilon)                     Gauss linear corrected;
}

interpolationSchemes
{
    default                                     linear;
    interpolate(HbyA)                           linear;
    "interpolate\(moment.*\)"                   upwind phi;
    reconstruct(U)                              upwind;
    reconstruct(weight)                         upwind;
    reconstruct(abscissa)                       upwind;
    reconstruct(sigma)                          upwind;
}

snGradSchemes
{
    default                 corrected;
}

fluxRequired
{
    p;
}
```

Figure D.1: Summary of numerical schemes used for 2D Dahl cases

```
populationBalanceModel univariate;

univariateCoeffs
{
    aggregation off;
    aggregationKernel
    {
        aggregationKernel constant;
    }

    breakup off;
    breakupKernel
    {
        breakupKernel constant;

        Cb        Cb        [ 0 0 0 0 0 0 0 ] 6.0e-4;
        epsilonExp          0.75;
        nuExp              -1.25;
        sizeExp             1.0;
    }
    daughterDistribution
    {
        daughterDistribution symmetricFragmentation;
    }
    diffusionModel
    {
        diffusionModel  none;
        gammaLam        gammaLam    [ 0 2 -1 0 0 0 0 ] 0.0001;
        Sc              0.7;
    }
    growth on;
    growthModel
    {
        growthModel     GalbraithGrowth;
        minAbscissa     minAbscissa [0 1 0 0 0 0 0] 0.0;
        maxAbscissa     maxAbscissa [0 1 0 0 0 0 0] 1.0;
        Cg        Cg        [0 0 -1 0 0 0 0 ] 2.0812e-5; // Galbraith
        exponent    5.062;
    }
    nucleationModel
    {
        nucleationModel  powerLawNucleation;
        powerLawNucleationCoeffs
        {
            nucleationRate nucleationRate [0 0 0 0 0 0 0] 1.417e9;
            exponent    1.68; //Galbraith
        }
    }
}
```

Figure D.2: Specification file stating all model parameters used by the PBE part of the framework.

```
moments
(
    (0)
    (1)
    (2)
    (3)
    (4)
);

nodes
(
    node0
    {
        nSecondaryNodes 10;
    }
    node1
    {
        nSecondaryNodes 10;
    }
);

extendedMomentInversionCoeff
{
    extendedMomentInversion     lognormal;

    maxSigmaIter        1000;
    momentsTol          1.0e-6;
    sigmaTol            1.0e-8;
    targetFunctionTol   1.0e-8;
}
```

Figure D.3: Specification file stating all model parameters related to the qudrature algorithm part of the framework.

```
phases (struvite water);

struvite
{
    transportModel  BinghamPlastic;

    "(plastic|BinghamPlastic)Coeffs"
    {
        coeff       0.00023143;
        exponent    179.26;

        BinghamCoeff    5.5469e-5;
        BinghamExponent 951.25;
        BinghamOffset   0;

        muMax       10;
    }

    rho         1710;
}

water
{
    transportModel  Newtonian;

    nu              1.7871e-06;
    rho             996;
}

relativeVelocityModel simpleVarying;

"(simple|general)Coeffs"
{
    V0              (0 -0.002198 0);
    a               285.84;
    al              0.1;
    residualAlpha   0;
}

"(simpleVarying|generalVarying)Coeffs"
{
    V0              (0 0 0);
    a               285.84;
    al              0.1;
    residualAlpha   0;

    g               (0 -9.81 0);
}
```

Figure D.4: Specification file stating all model parameters related to each different fluid phase as well as the speciation thermodynamics.

```
simulationType Galbraith;
speciesThermoModel MAPST;

speciesMixture
{
    species
    (
        NH4
        PO4
        MG
        MAP
        H2O
    );
    NH4
    {
        molWeight       molWeight [1 0 0 0 -1 0 0] 18.03846;
        rExponent       1;
        requiredC       0.004;
        ionCharge       1;
    }
    PO4
    {
        molWeight       molWeight [1 0 0 0 -1 0 0] 94.9714;
        rExponent       1;
        requiredC       0.004;
        ionCharge       -3;
    }
    MG
    {
        molWeight       molWeight [1 0 0 0 -1 0 0] 24.3050;
        rExponent       1;
        requiredC       0.004;
        ionCharge       2;
    }
    MAP
    {
        molWeight       molWeight [1 0 0 0 -1 0 0] 243.15;
        rExponent       0;
    }
    H2O
    {
        molWeight       molWeight [1 0 0 0 -1 0 0] 18.015;
        rExponent       0;
    }_++___+

    inertSpecie         H2O;
    precipitant         MAP;

    ka  0.523; // Pi/6
    kv  0.01;
```

Figure D.5: First part of the specification file stating all model parameters related to precipitation part of the framework.

```
    MAPSTCoeffs
    {
        nReactants      3;

        gammaVariation  true;
        gamma           1;

        ADH             0.509;

        //pH              7.46;
        pH              9.6;

        equilibriumConstants
        {
            pKHPO4      -12.35;
            pKH2PO4     -7.20;
            pKH3PO4     -2.15;
            pKMgPO4     -4.80;
            pKMgHPO4    -2.91;
            pKMgH2PO4   -0.45;
            pKMgOH      -2.56;
            pKNH4       -9.25;
            pKH2O       -14;

            Ksp         6.76e-14;
            pKsp        -13.26;
        }
    }

    "(idealSTCoeffs|nonIdealSTCoeffs)"
    {
        nReactants      3;
        gamma           1;

        pH              9.6;

        equilibriumConstants
        {
            Ksp         6.76e-14;
            pKsp        -13.26;
        }
    }
}
```

Figure D.6: Second part of the specification file stating all model parameters related to precipitation part of the framework.

Appendix E

2D Dahl case mesh sensitivity analysis

Plots presented in this section show the variation of Sauter mean diameter with respect to the computational mesh size. As discussed in Section 6.1 data sampling was performed at three separate locations each of which are shown in Figures below.

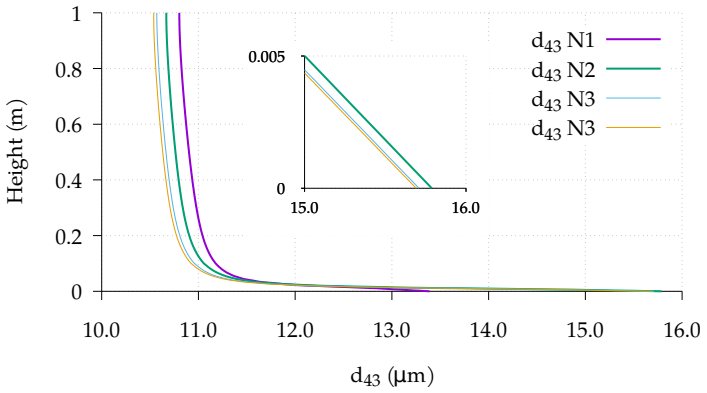

Figure E.1: Mesh sensitivity analysis of two dimensional test case of Dahl settling tank [35]; measurements at $x = 3$m location

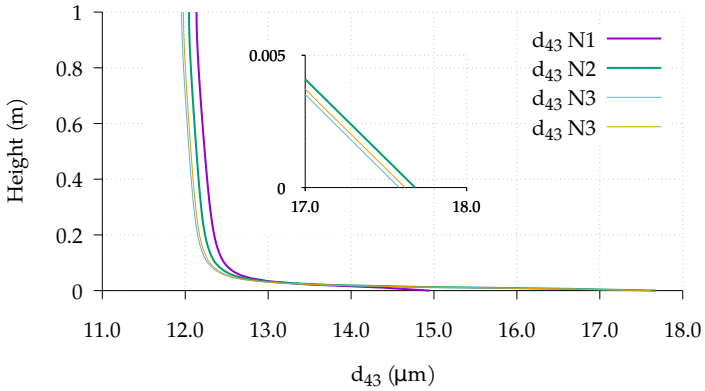

Figure E.2: Mesh sensitivity analysis of two dimensional test case of Dahl settling tank [35]; measurements at $x = 5$m location

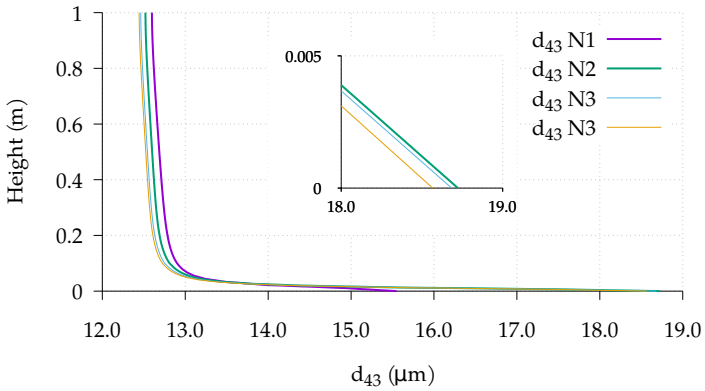

Figure E.3: Mesh sensitivity analysis of two dimensional test case of Dahl settling tank [35]; measurements at $x = 7$m location

Appendix F

2D Dahl case instantaneous visualisations

This appendix is dedicated to provided supplementary outputs from the 2 dimensional test case presented in Section 6.1. As discussed in results section of these test cases, the majority analysis was performed using the time averaged values of the parameters. However, the instantaneous field values can also provide valuable information and therefore these are presented in this Appendix.

Outputs from Cases (1.a) and (1-b) are presented between Figures F.1-F.12, whereas the outputs form Cases (2.a) and (2.b) are presented between Figures F.13-F.24.

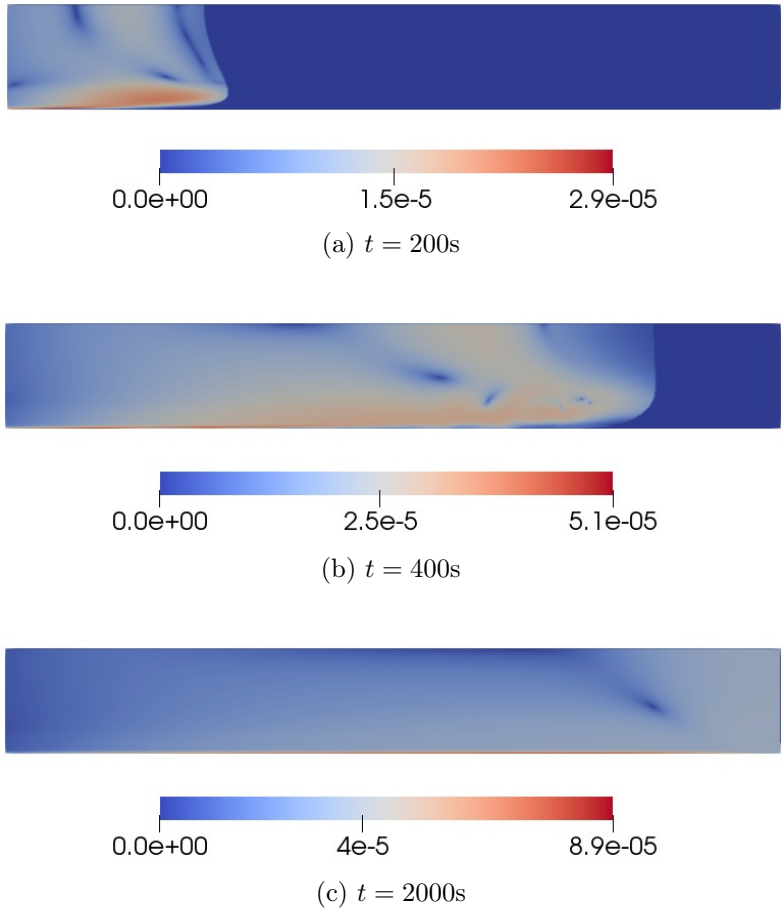

(a) $t = 200$s

(b) $t = 400$s

(c) $t = 2000$s

Figure F.1: Magnitudes of the dispersed phase settling velocities using *Simple-varying* model from Case (1.a).

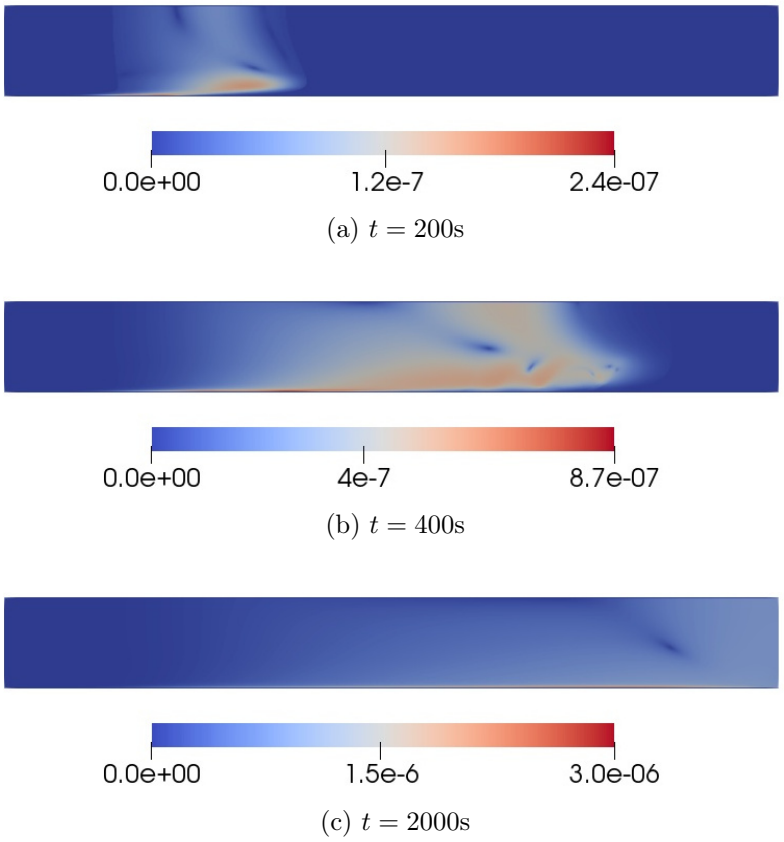

(a) $t = 200$s

(b) $t = 400$s

(c) $t = 2000$s

Figure F.2: Magnitude of the dispersed phase settling velocities using *General-varying model* from Case (1.b).

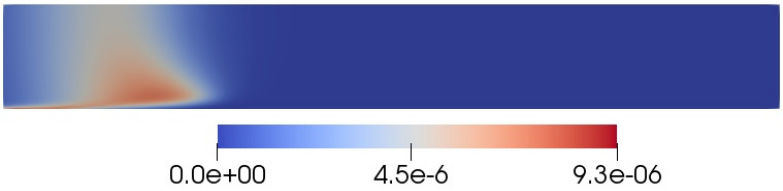

(a) α_d at $t = 200$s

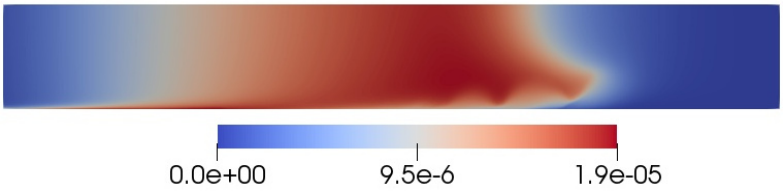

(b) α_d at $t = 400$s

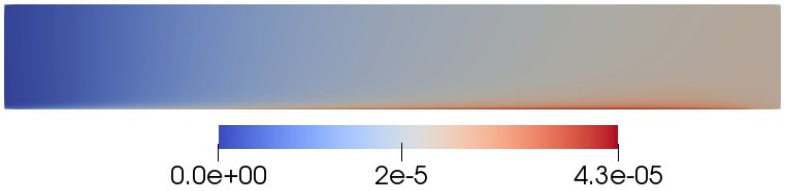

(c) α_d at $t = 2000$s

Figure F.3: The dispersed phase volume fractions from Case (1.a).

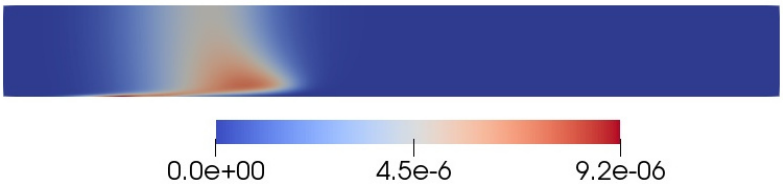

(a) α_d at $t = 200$s

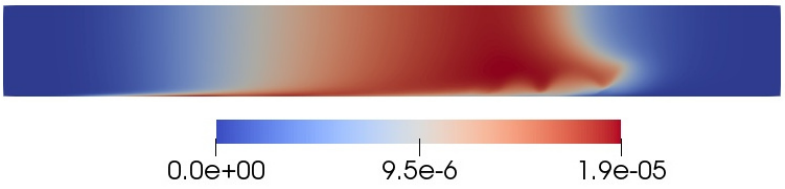

(b) α_d at $t = 400$s

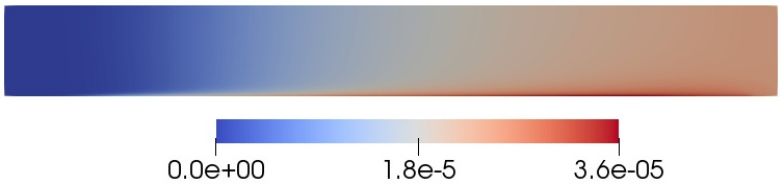

(c) α_d at $t = 2000$s

Figure F.4: The dispersed phase volume fractions from Case (1.b).

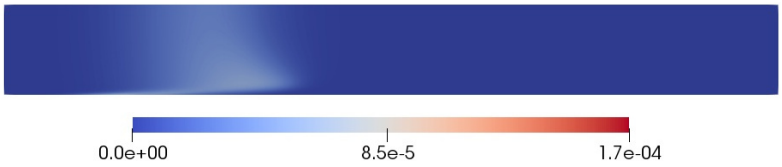

(a) C_{MAP} at $t = 200$s

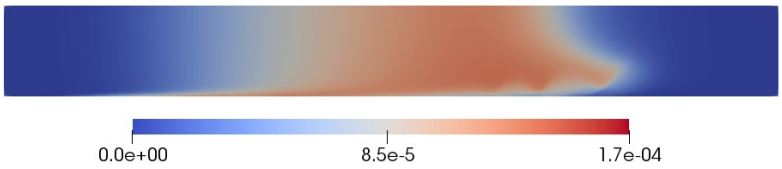

(b) C_{MAP} at $t = 400$s

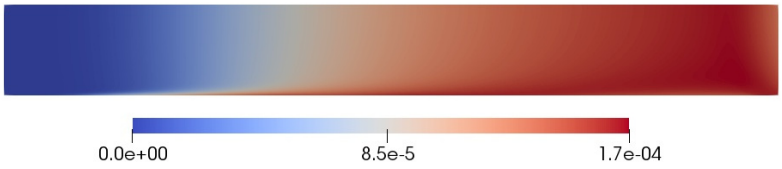

(c) C_{MAP} at $t = 2000$s

Figure F.5: Instantaneous concentrations of struvite from Case (1.a).

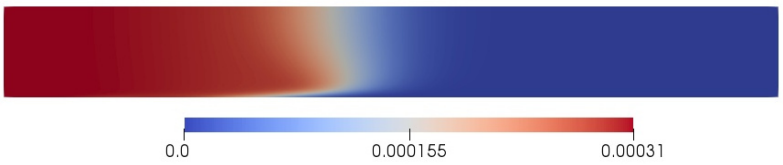

(a) C_{NH4} at $t = 200$s

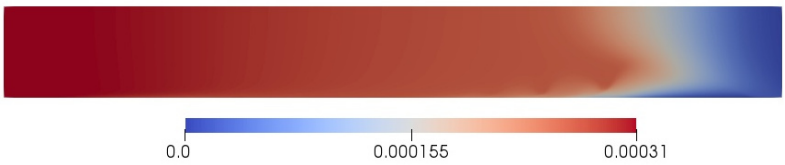

(b) C_{NH4} at $t = 400$s

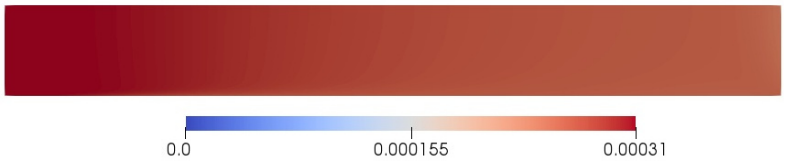

(c) C_{NH4} at $t = 2000$s

Figure F.6: Instantaneous concentrations of NH_4 from Case (1.a).

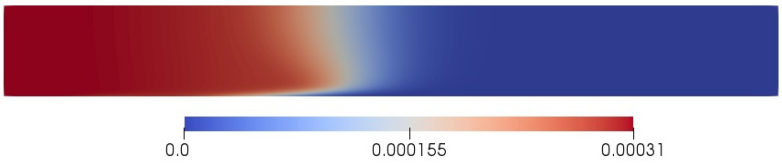

(a) C_{PO4} at $t = 200$s

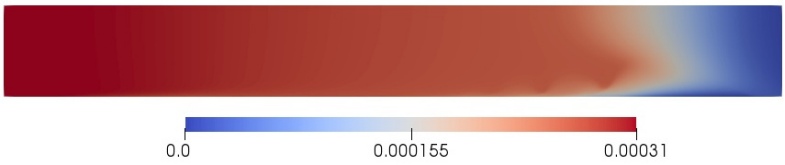

(b) C_{PO4} at $t = 400$s

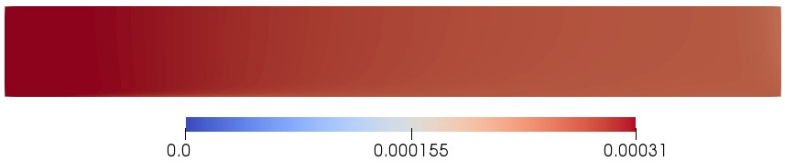

(c) C_{PO4} at $t = 2000$s

Figure F.7: Instantaneous concentrations of PO_4 from Case (1.a).

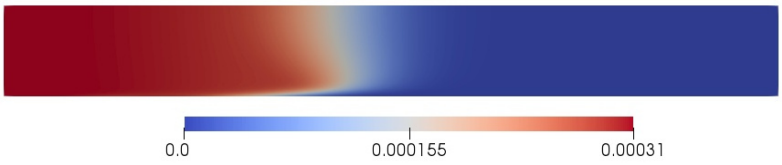

(a) C_{MG} at $t = 200$s

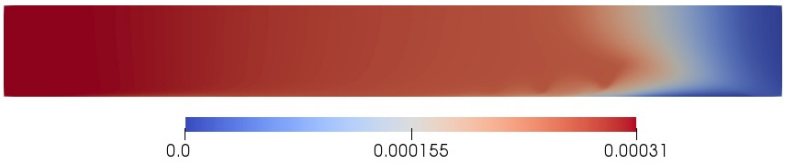

(b) C_{MG} at $t = 400$s

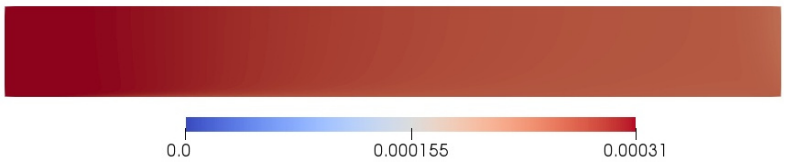

(c) C_{MG} at $t = 2000$s

Figure F.8: Instantaneous concentrations of MG from Case (1.a).

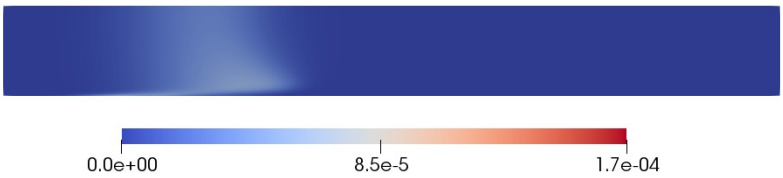

(a) C_{MAP} at $t = 200$s

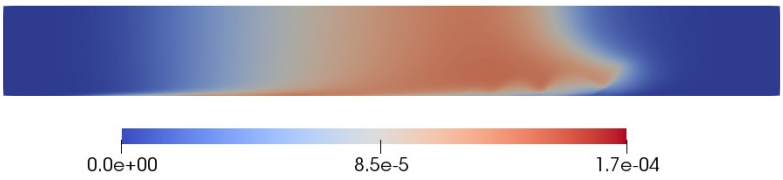

(b) C_{MAP} at $t = 400$s

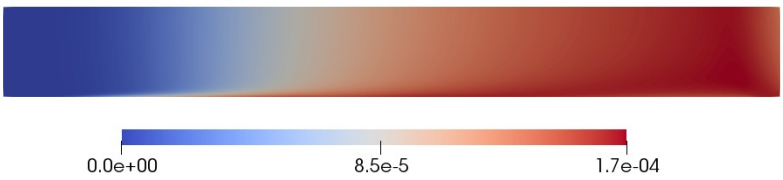

(c) C_{MAP} at $t = 2000$s

Figure F.9: Instantaneous concentrations of struvite from Case (1.b).

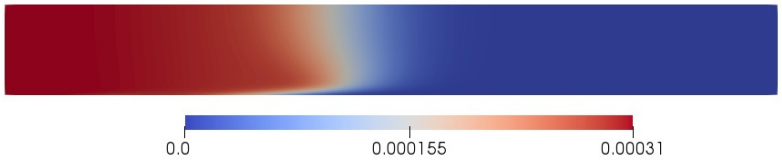

(a) C_{NH4} at $t = 200$s

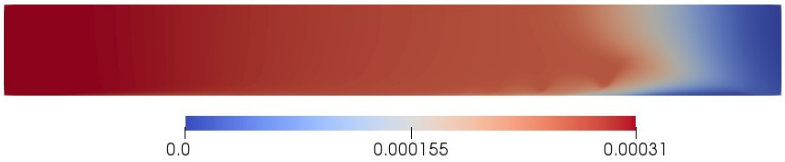

(b) C_{NH4} at $t = 400$s

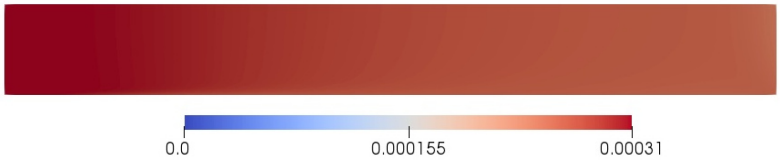

(c) C_{NH4} at $t = 2000$s

Figure F.10: Instantaneous concentrations of NH_4 from Case (1.b).

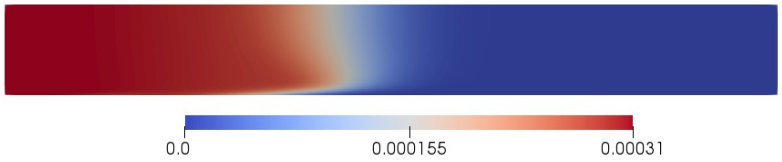

(a) C_{PO4} at $t = 200$s

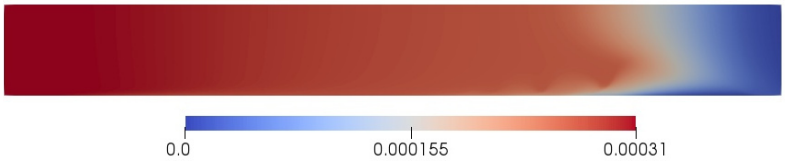

(b) C_{PO4} at $t = 400$s

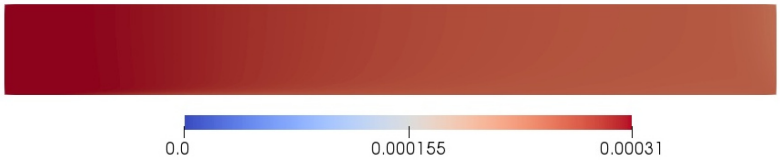

(c) C_{PO4} at $t = 2000$s

Figure F.11: Instantaneous concentrations of PO_4 from Case (1.b).

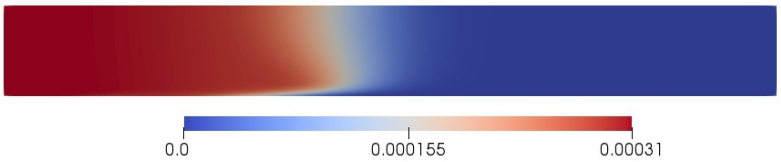

(a) C_{MG} at $t = 200$s

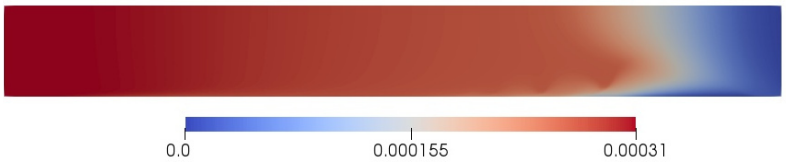

(b) C_{MG} at $t = 400$s

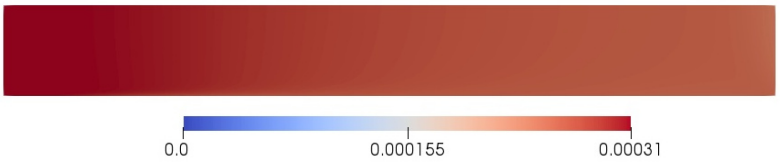

(c) C_{MG} at $t = 2000$s

Figure F.12: Instantaneous concentrations of MG from Case (1.b).

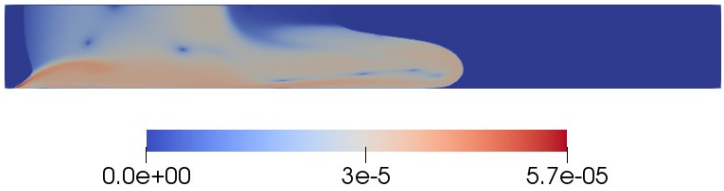

(a) $t = 800$s

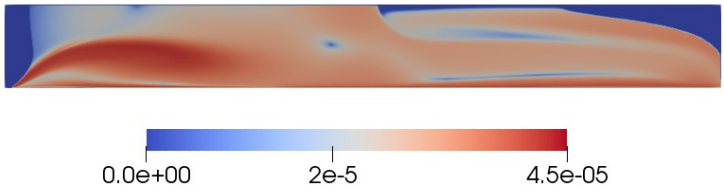

(b) $t = 1600$s

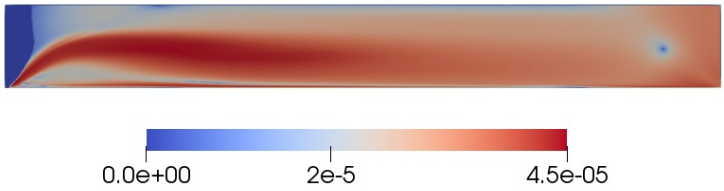

(c) $t = 6000$s

Figure F.13: The dispersed phase settling velocities from Case (2.a).

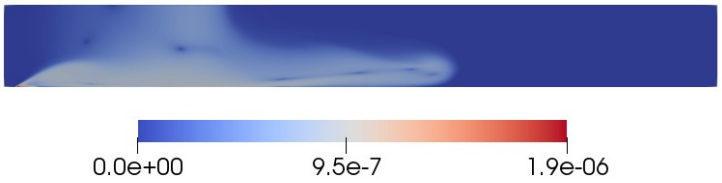

(a) $t = 800$s

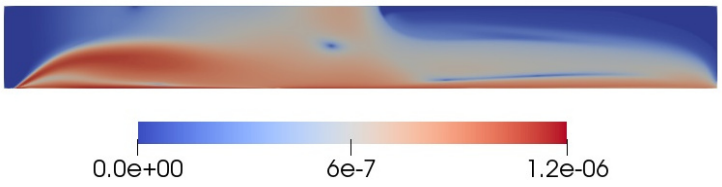

(b) $t = 1600$s

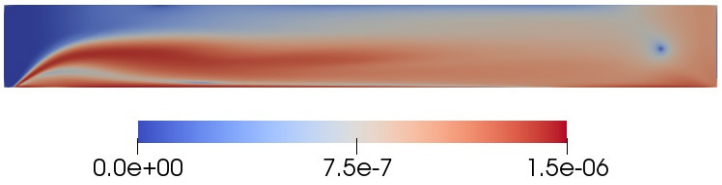

(c) $t = 6000$s

Figure F.14: The dispersed phase settling velocities from Case (2.b).

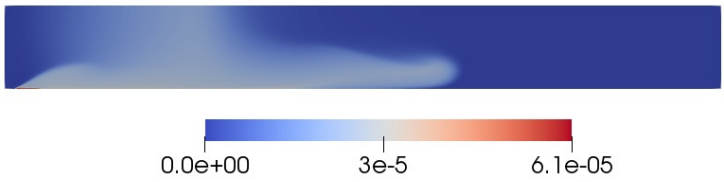

(a) α_d at $t = 800$s

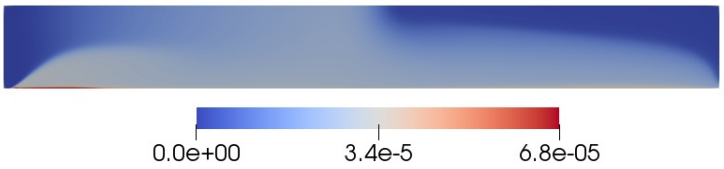

(b) α_d at $t = 1600$s

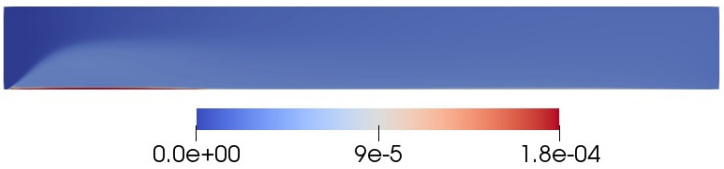

(c) α_d at $t = 6000$s

Figure F.15: The dispersed phase volume fractions from Case (2.a).

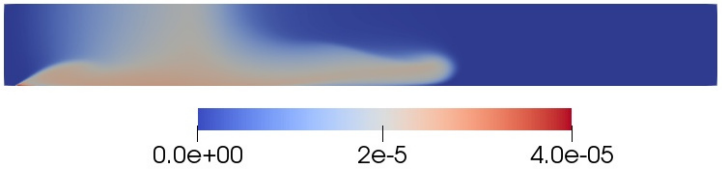

(a) α_d at $t = 800$s

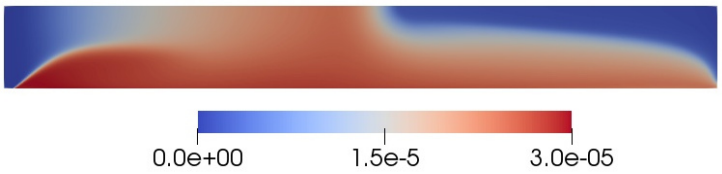

(b) α_d at $t = 1600$s

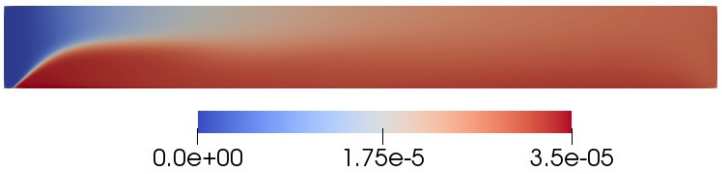

(c) α_d at $t = 6000$s

Figure F.16: The dispersed phase volume fraction from Case (2.b).

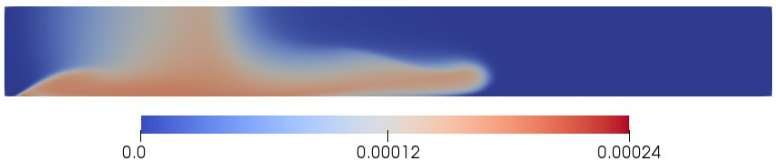

(a) C_{MAP} at $t = 800$s

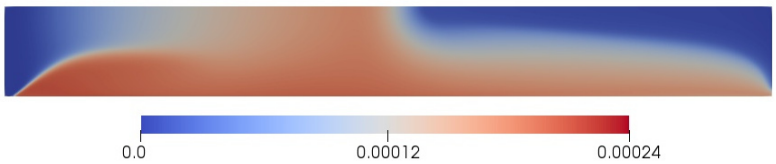

(b) C_{MAP} at $t = 1600$s

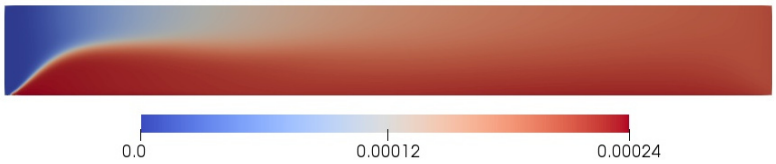

(c) C_{MAP} at $t = 6000$s

Figure F.17: Instantaneous concentrations of struvite from Case (2.a).

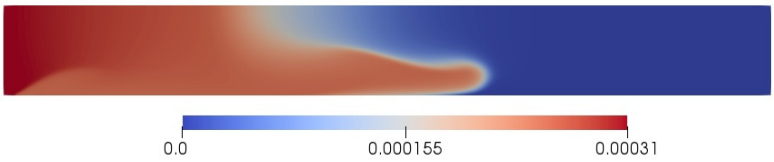

(a) C_{NH4} at $t = 800$s

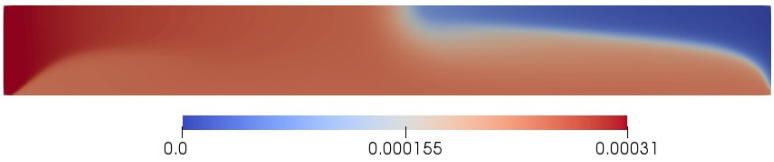

(b) C_{NH4} at $t = 1600$s

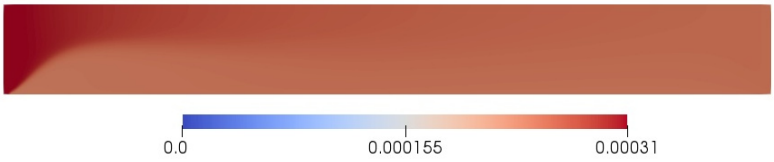

(c) C_{NH4} at $t = 6000$s

Figure F.18: Instantaneous concentrations of NH_4 from Case (2.a).

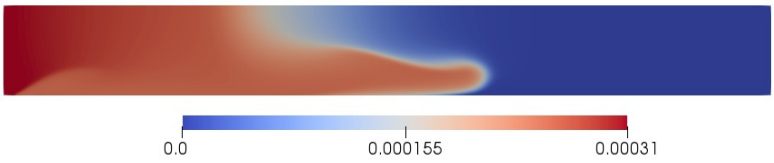

(a) C_{PO4} at $t = 800$s

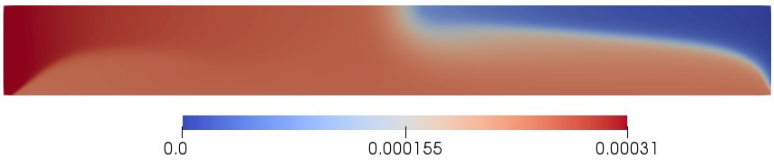

(b) C_{PO4} at $t = 1600$s

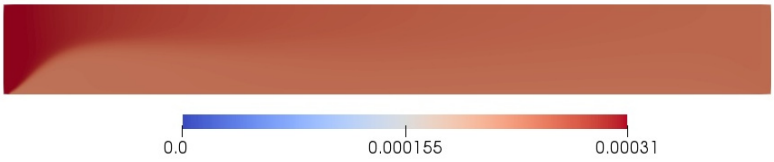

(c) C_{PO4} at $t = 6000$s

Figure F.19: Instantaneous concentrations of PO_4 from Case (2.a).

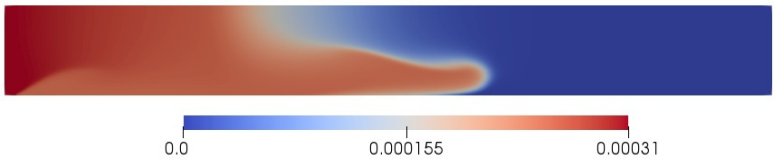

(a) C_{MG} at $t = 800$s

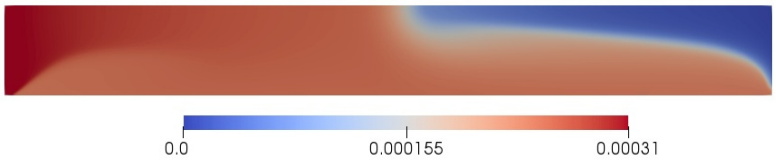

(b) C_{MG} at $t = 1600$s

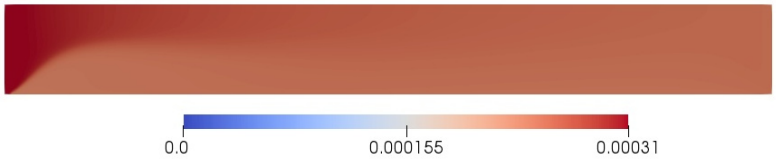

(c) C_{MG} at $t = 6000$s

Figure F.20: Instantaneous concentrations of MG from Case (2.a).

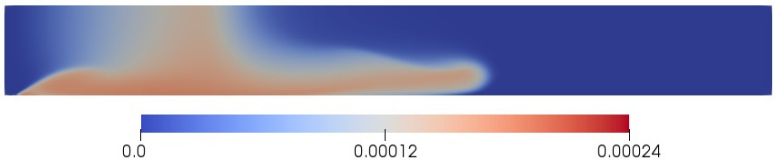

(a) C_{MAP} at $t = 800$s

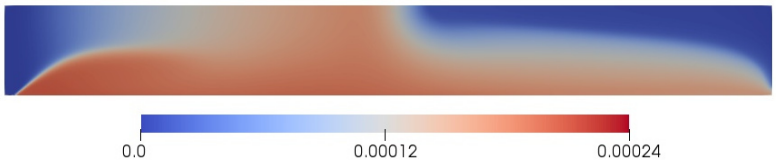

(b) C_{MAP} at $t = 1600$s

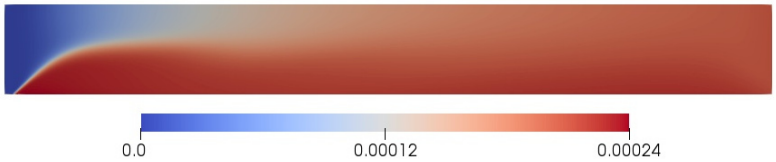

(c) C_{MAP} at $t = 6000$s

Figure F.21: Instantaneous concentrations of struvite from Case (2.b).

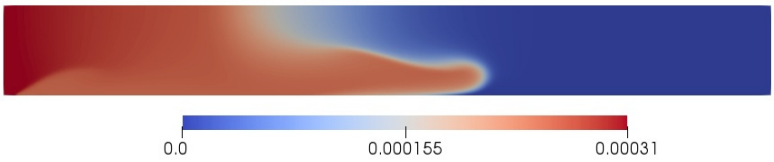

(a) C_{NH4} at $t = 800$s

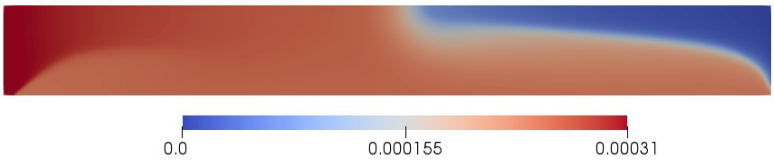

(b) C_{NH4} at $t = 1600$s

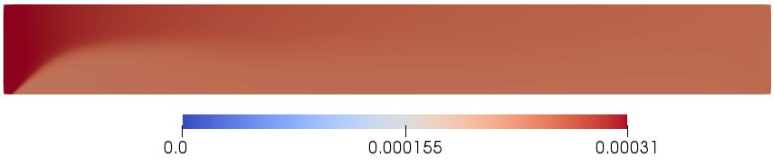

(c) C_{NH4} at $t = 6000$s

Figure F.22: Instantaneous concentrations of NH_4 from Case (2.b).

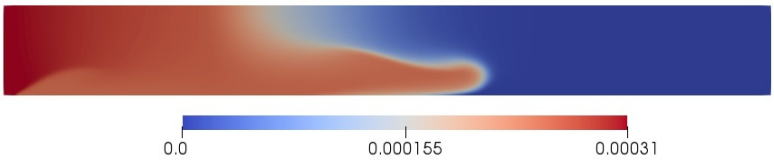

(a) C_{PO4} at $t = 800$s

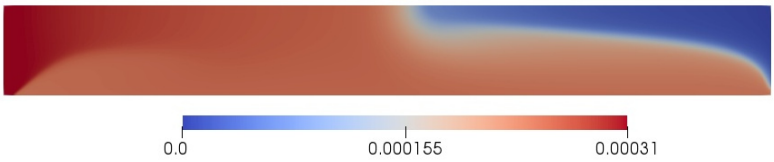

(b) C_{PO4} at $t = 1600$s

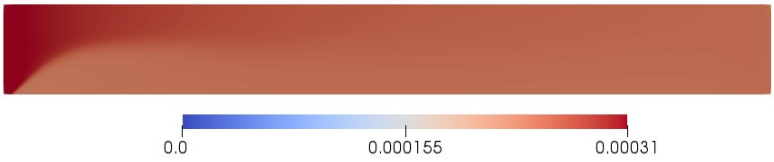

(c) C_{PO4} at $t = 6000$s

Figure F.23: Instantaneous concentrations of PO_4 from Case (2.b).

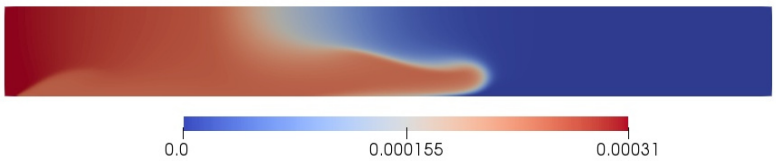

(a) C_{MG} at $t = 800$s

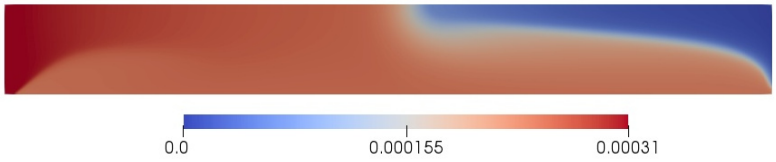

(b) C_{MG} at $t = 1600$s

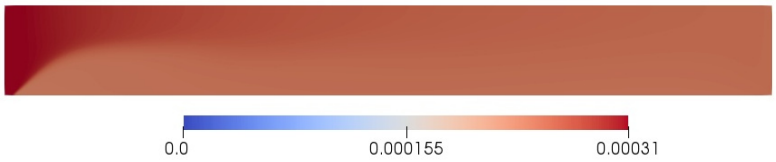

(c) C_{MG} at $t = 6000$s

Figure F.24: Instantaneous concentrations of MG from Case (2.b).

Bibliography

[1] A. Adnan. *Pilot-scale study of phosphorus recovery through struvite crystallization.* PhD thesis, University of British Columbia, 2002.

[2] A. H. Alexopoulos, D. Maggioris, and C. Kiparissides. CFD analysis of turbulence non-homogeneity in mixing vessels a two-compartment model. *Chemical Engineering Science*, 57(10):1735–1752, 2002. doi: 10.1016/S0009-2509(02)00053-2.

[3] M. I. Ali. *Struvite crystallization from nutrient rich wastewater.* PhD thesis, James Cook University, 2005.

[4] M. I. Ali and P. A. Schneider. An approach of estimating struvite growth kinetic incorporating thermodynamic and solution chemistry, kinetic and process description. *Chemical Engineering Science*, 63(13):3514–3525, 2008. doi: 10.1016/j.ces.2008.04.023.

[5] V. Alopaeus, J. Koskinen, and K. I. Keskinen. Simulation of the population balances for liquid - liquid systems in a nonideal stirred tank. Part 1 Description and qualitative validation of the model. *Chemical Engineering Science*, 54(24):5887–5899, 1999. doi: 10.1016/S0009-2509(99)00170-0.

[6] V. Alopaeus, J. Koskinen, K. I. Keskinen, and J. Majander. Simulation of the population balances for liquid-liquid systems in a nonideal stirred tank. Part 2-parameter fitting and the use of the multiblock model for dense dispersions. *Chemical Engineering Science*, 57(10):1815–1825, 2002. doi: 10.1016/S0009-2509(02)00067-2.

[7] H. Arastoopour, D. Gidaspow, and E. Abbasi. *Computational Transport Phenomena of Fluid-Particle Systems*. Mechanical Engineering Series. Springer International Publishing, Cham, 2017. ISBN 978-3-319-45488-7. doi: 10.1007/978-3-319-45490-0.

[8] K. Ashley, D. Cordell, and D. Mavinic. A brief history of phosphorus: From the philosopher's stone to nutrient recovery and reuse. *Chemosphere*, 84(6): 737–746, 2011. doi: 10.1016/j.chemosphere.2011.03.001.

[9] J. Bałdyga and J. R. Bourne. *Turbulent mixing and chemical reactions*. Wiley, 1999. ISBN 978-0471981718.

[10] J. Bałdyga and W Orciuch. Closure problem for precipitation. *Chemical Engineering Research and Design*, 75(2):160–170, 1997. doi: 10.1205/026387697523624.

[11] J. Bałdyga and W. Orciuch. Barium sulphate precipitation in a pipe - an experimental study and CFD modelling. *Chemical Engineering Science*, 56 (7):2435–2444, 2001. doi: 10.1016/S0009-2509(00)00449-8.

[12] P. Battistoni, A. De Angelis, M. Prisciandaro, R. Boccadoro, and D. Bolzonella. P removal from anaerobic supernatants by struvite crystallization: Long term validation and process modelling. *Water Research*, 36(8):1927–1938, 2002. doi: 10.1016/S0043-1354(01)00401-8.

[13] J. Becker. *Coupling of Population Balance Modelling and Computational Fluid Dynamics Applied to Turbulent Emulsification Processes in Complex Geometries*. PhD thesis, L'Universite Claude Bernard Lyon 1, 2013.

[14] Andrey V. Bekker, Tian S. Li, and Iztok Livk. Comparison of FEM and DPB numerical methodologies for dynamic modeling of isothermal batch gibbsite crystallization. *Industrial and Engineering Chemistry Research*, 50(7):3994–4002, 2011. doi: 10.1021/ie101942s.

[15] U. Berg, A. Ehbrecht, E. Röhm, P. G. Weidler, and R. Nüesch. Impact of Calcite on Phosphorus Removal and Recovery from Wastewater Using CSH-Filled Fixed Bed Filters. *Journal of Residuals Science and Technology*, 4(2): 73–81, 2007.

[16] M. I. H. Bhuiyan. *Investigation into Struvite Solubility, Growth and Dissolution Kinetics in the Context of Phosphorus Recovery from Wastewater*. PhD thesis, The University of British Columbia, 2007.

[17] M. I. H. Bhuiyan, D. S. Mavinic, and R. D. Beckie. A solubility and thermodynamic study of struvite. *Environmental Technology*, 28(9):1015–1026, 2007. doi: 10.1080/09593332808618857.

[18] M. I. H. Bhuiyan, D. S. Mavinic, and R. D. Beckie. Nucleation and growth kinetics of struvite in a fluidized bed reactor. *Journal of Crystal Growth*, 310 (6):1187–1194, 2008. doi: 10.1016/j.jcrysgro.2007.12.054.

[19] N. C. Bouropoulos and P. G. Koutsoukos. Spontaneous precipitation of struvite from aqueous solutions. *Journal of Crystal Growth*, 213(3-4):381–388, 2000. doi: 10.1016/S0022-0248(00)00351-1.

[20] L. Bravo, M. Kurman, C. Kweon, S. Wijeyakulasuriya, and PK. Senecal. Lagrangian Modeling of Evaporating Sprays at Diesel Engine Conditions: Effects of Multi-Hole Injector Nozzles With JP-8 Surrogates. Technical report, Army Research Laboratory, 2014.

[21] D. Brennan. *The Numerical Simulation of Two-Phase Flows in Settling Tanks*. PhD thesis, Imperial College of Science, Technology and Medicine, 2001.

[22] C. E. Brennen. *Fundamentals of Multiphase Flows*. Cambridge University Press, 2005. ISBN 0521848040. doi: 10.1088/1751-8113/44/8/085201.

[23] A. T. Britton, F. Sacluti, W. K. Oldham, A. Mohammed, D. S. Mavinic, and F. A. Koch. Value from waste: struvite recovery at the city of Edmon-

tons Gold Bar WWTP. *Proc. IWA Specialist Conference: Moving Forward - Wastewater biosolids sustainability.*, pages 575–581, 2007.

[24] L. A. Bromley. Thermodynamic properties of strong electrolytes in aqueous solutions. *AIChE Journal*, 19(2):313–320, 1973. doi: 10.1002/aic.690190216.

[25] I Celen and M Türker. Recovery of ammonia as struvite from anaerobic digester effluents. *Environmental technology*, 22(11):1263–72, 2001. doi: 10.1080/09593332208618192.

[26] I. Çelen, J. R. Buchanan, R. T. Burns, R. Bruce, and D. Raj Raman. Using a chemical equilibrium model to predict amendments required to precipitate phosphorus as struvite in liquid swine manure. *Water Research*, 41(8):1689–1696, 2007. doi: 10.1016/j.watres.2007.01.018.

[27] C. Chalons, R. O. Fox, F. Laurent, and M. Massot. Multivatiate Gaussian Extended Quadrature Method of Moments For Turbulent Disperse Multiphase Flow. *Multiscale Modeling and Simulation*, 15(4):1553–1583, 2017. doi: 10.1137/16M109209X.

[28] P. Chen, J. Sanyal, and M. P. Dudukovic. CFD modeling of bubble columns flows: Implementation of population balance. In *Chemical Engineering Science*, volume 59, pages 5201–5207, 2004. ISBN 0009-2509. doi: 10.1016/j.ces.2004.07.037.

[29] J. Cheng, C. Yang, and Z. S. Mao. CFD-PBE simulation of premixed continuous precipitation incorporating nucleation, growth and aggregation in a stirred tank with multi-class method. *Chemical Engineering Science*, 68(1):469–480, 2012. doi: 10.1016/j.ces.2011.10.032.

[30] C. W. Childs. A Potentiometric Study of Equilibria in Aqueous Divalent Metal Orthophosphate Solutions. *Inorganic Chemistry*, 9(11):2465–2469, 1970. doi: 10.1021/ic50093a017.

[31] B. Cieślik and P. Konieczka. A review of phosphorus recovery methods at various steps of wastewater treatment and sewage sludge management. The concept of "no solid waste generation" and analytical methods. *Journal of Cleaner Production*, 142:1728–1740, 2017. doi: 10.1016/j.jclepro.2016.11.116.

[32] D. Cordell, J. O. Drangert, and S. White. The story of phosphorus: Global food security and food for thought. *Global Environmental Change*, 19(2): 292–305, 2009. doi: 10.1016/j.gloenvcha.2008.10.009.

[33] D. Cordell, A. Rosemarin, J. J. Schröder, and A. L. Smit. Towards global phosphorus security: A systems framework for phosphorus recovery and reuse options. *Chemosphere*, 84(6):747–758, 2011. doi: 10.1016/j.chemosphere.2011.02.032.

[34] C. T. Crowe, J. D. Schwarzkopf, M. Sommerfeld, and Y. Tsuji. *Multiphase Flows with Droplets and Particles*. CRC Press, 2 edition, 2012. ISBN 0849394694. doi: 10.1201/b11103-4.

[35] C. P. Dahl. *Numerical modelling of flow and settling in secondary settling tanks*. PhD thesis, Aalborg University, 1995.

[36] M. Darwish, I. Sraj, and F. Moukalled. A coupled finite volume solver for the solution of incompressible flows on unstructured grids. *Journal of Computational Physics*, 228(1):180–201, 2009. doi: 10.1016/j.jcp.2008.08.027.

[37] C. W. Davies. *Ion Association*. Butterworth, London-Washington, 1962.

[38] L. E. De-Bashan and Y. Bashan. Recent advances in removing phosphorus from wastewater and its future use as fertilizer (1997-2003). *Water Research*, 38(19):4222–4246, 2004. doi: 10.1016/j.watres.2004.07.014.

[39] G. B. Deng, J. Piquet, X. Vasseur, and M. Visonneau. A new fully coupled method for computing turbulent flows. *Computers and Fluids*, 30(4):445–472, 2001. doi: 10.1016/S0045-7930(00)00025-6.

[40] O. Desjardins, R. O. Fox, and P. Villedieu. A quadrature-based moment method for dilute fluid-particle flows. *Journal of Computational Physics*, 227 (4):2514–2539, 2008. doi: 10.1016/j.jcp.2007.10.026.

[41] H. Dette and W. J. Studden. *The theory of canonical moments with applications in statistics, probability, and analysis*, volume 338. John Wiley & Sons, 1997. ISBN 0471109916.

[42] J. D. Doyle and S. A. Parsons. Struvite formation, control and recovery. *Water Research*, 36(16):3925–3940, 2002. doi: 10.1016/S0043-1354(02)00126-4.

[43] A. E. Durrant, M. D. Scrimshaw, I. Stratful, and J. N. Lester. Review of the Feasibility of Recovering Phosphate from Wastewater for Use as a Raw Material by the Phosphate Industry. *Environmental Technology*, 20(7):749–758, 1999. doi: 10.1080/09593332008616870.

[44] L. Egle, H. Rechberger, and M. Zessner. Overview and description of technologies for recovering phosphorus from municipal wastewater. *Resources, Conservation and Recycling*, 105:325–346, 2015. doi: 10.1016/j.resconrec.2015.09.016.

[45] S. Elghobashi. On predicting particle-laden turbulent flows. *Applied Scientific Research*, 52(4):309–329, 1994. doi: 10.1007/BF00936835.

[46] J. Emsley. *The 13th Element: The Sordid Tale of Murder, Fire, and Phosphorus*. John Wiley & Sons, Inc., 2002. ISBN 047144149X. doi: 047144149X.

[47] Kazi P Fattah, Donald S Mavinic, and Frederic A Koch. Influence of Process Parameters on the Characteristics of Struvite Pellets. *Journal of Environmental Engineering*, 138(12):1200–1209, 2012. doi: 10.1061/(ASCE)EE.1943-7870.0000576.

[48] J. H. Ferziger and M. Perić. *Computational methods for fluid dynamics*. Springer, 2003. ISBN 3540420746. doi: 10.1016/S0898-1221(03)90046-0.

[49] R. A. Fischer, D. Byerlee, and G. O. Edmeades. Can technology deliver on the yield challenge to 2050? *Fao*, 2050(June):1–48, 2009.

[50] S. C. Galbraith, P. A. Schneider, and A. E. Flood. Model-driven experimental evaluation of struvite nucleation, growth and aggregation kinetics. *Water Research*, 56:122–132, 2014. doi: 10.1016/j.watres.2014.03.002.

[51] W. Gautschi. *Orthogonal Polynomials: Computation and Approximation*. Oxford University Press on Demand, 2004.

[52] R. G. Gordon. Error bounds in equilibrium statistical mechanics. *Journal of Mathematical Physics*, 9(5):655–663, 1968. doi: 10.1063/1.1664624.

[53] R. G. Gordon. Error Bounds in Spectroscopy and Nonequilibrium Statistical Mechanics. *Journal of Mathematical Physics*, 9(7):1087–1092, 1968. doi: 10.1063/1.1664681.

[54] D. I. Graham and R. A. Moyeed. How many particles for my Lagrangian simulations? *Powder Technology*, 125(2-3):179–186, 2002. doi: 10.1016/S0032-5910(01)00504-6.

[55] M. Hanhoun, L. Montastruc, C. Azzaro-Pantel, B. Biscans, M. Frèche, and L. Pibouleau. Simultaneous determination of nucleation and crystal growth kinetics of struvite using a thermodynamic modeling approach. *Chemical Engineering Journal*, 215-216:903–912, 2013. doi: 10.1016/j.cej.2012.10.038.

[56] X. D. Hao, C. C. Wang, L. Lan, and M. C M Van Loosdrecht. Struvite formation, analytical methods and effects of pH and Ca 2+. *Water Science and Technology*, 58(8):1687–1692, 2008. doi: 10.2166/wst.2008.557.

[57] B. Heinzmann. P-Recycling in Berlin - from Pilot Scale Experiments to large Scale Application. Technical report, Baltic 21 - Phosphorus Recycling and Good Agricultural Application, Berlin, 2009.

[58] D. P. Hill. *The Computer Simulation of Dispersed Two-phase Flows*. PhD thesis, Imperial College of Science, Technology and Medicine, 1998.

[59] C. Hirsch. *Numerical computation of internal and external flows: The fundamentals of computational fluid dynamics, vol 1.* John Wiley & Sons, Ltd., 2nd edition, 1988. ISBN 9780750665940.

[60] H. M. Hulburt and S. Katz. Some problems in particle technology. A statistical mechanical formulation. *Chemical Engineering Science*, 19(8):555–574, 1964. doi: 10.1016/0009-2509(64)85047-8.

[61] N. Hutnik, K. Piotrowski, B. Wierzbowska, and A. Martynia. Continuous reaction crystallization of struvite from phosphate(V) solutions containing calcium ions. *Crystal Research and Technology*, 46(5):443–449, 2011. doi: 10.1002/crat.201100049.

[62] N. Hutnik, A. Kozik, A. Mazienczuk, K. Piotrowski, B. Wierzbowska, and A. Matynia. Phosphates (V) recovery from phosphorus mineral fertilizers industry wastewater by continuous struvite reaction crystallization process. *Water Research*, 47(11):3635–3643, 2013. doi: 10.1016/j.watres.2013.04.026.

[63] M. Ishii and T. Hibiki. *Thermo-Fluid Dynamics of Two-Phase Flow.* Springer, 2nd edition, 2011. ISBN 9781441979841. doi: 10.1007/978-1-4419-7985-8.

[64] R. I. Issa. Solution of the implicitly discretised fluid flow equations by operator-splitting. *Journal of Computational Physics*, 62(1):40–65, 1986. doi: 10.1016/0021-9991(86)90099-9.

[65] Hugo A. Jakobsen. *Chemical Reactor Modeling.* Springer, 2008. ISBN 9788578110796.

[66] H Jasak. *Error Analysis and Estimation for the Finite Volume Method with Applications to Fluid Flows.* PhD thesis, Imperial College of Science, Technology and Medicine, 1996.

[67] S. M. Jasinski. Phosphate Rock, Mineral Commodity Summary. *US Geological Survey mineral commodity summaries*, 2010(January):118—-119, 2010.

[68] Z. Jaworski and A. W. Nienow. CFD modelling of continuous precipitation of barium sulphate in a stirred tank. *Chemical Engineering Journal*, 91(2-3): 167–174, 2003. doi: 10.1016/S1385-8947(02)00150-X.

[69] A.G. Jones. *Crystallisation Process Systems*, volume 53. Butterworth Heinemann, 2013. ISBN 9788578110796. doi: 10.1017/CBO9781107415324.004.

[70] S. Kataki, H. West, M. Clarke, and D. C. Baruah. Phosphorus recovery as struvite: Recent concerns for use of seed, alternative Mg source, nitrogen conservation and fertilizer potential. *Resources, Conservation and Recycling*, 107:142–156, 2016. doi: 10.1016/j.resconrec.2015.12.009.

[71] J. Koralewska, K. Piotrowski, B. Wierzbowska, and A. Matynia. Kinetics of Reaction-Crystallization of Struvite in the Continuous Draft Tube Magma Type Crystallizers-Influence of Different Internal Hydrodynamics. *Chinese Journal of Chemical Engineering*, 17(2):330–339, 2009. doi: 10.1016/S1004-9541(08)60212-8.

[72] A. Kozik, N. Hutnik, and A. Matynia. Recovery of phosphate (V) ions from liquid waste solutions containing organic impurities. *Chemik*, 65(7):675–686, 2011.

[73] S. Kumar and D. Ramkrishna. On the solution of population balance equations by discretization - I. A fixed pivot technique. *Chemical Engineering Science*, 51(8):1311–1332, 1996. doi: 10.1016/0009-2509(96)88489-2.

[74] F. Laurent and T. T. Nguyen. Realizable second-order finite-volume schemes for the advection of moment sets of the particle size distribution. *Journal of Computational Physics*, 337:309–338, 2017. doi: 10.1016/j.jcp.2017.02.046.

[75] K. S. Le Corre. *Understanding Struvite Crystallization and Recovery*. PhD thesis, Cranfield University, 2006.

[76] R. J. LeVeque. *Finite Volume Methods for Hyperbolic Problems*, volume 54. Cambridge University Press, 2004. ISBN 9780521009249. doi: 10.1017/CBO9780511791253.

[77] L. Liberti, D. Petruzzelli, and L. De Florio. REM-NUT Ion Exchange Plus Struvite Precipitation Process. *Environmental Technology*, 22(11):1313–1324, 2001. doi: 10.1080/09593330409355443.

[78] Lorenzo Liberti, Nicola Limoni, Antonio Lopez, Roberto Passino, and Gianfranco Boari. The 10 m3h-1 RIM-NUT demonstration plant at West Bari for removing and recovering N and P from wastewater. *Water Research*, 20(6): 735–739, 1986. doi: 10.1016/0043-1354(86)90097-7.

[79] S. Lo. Application of Population Balance to CFD Modeling of Bubbly Flow Via the MUSIG Model. In *CFX International Users Conference*, volume AEAT-1096, 1999.

[80] E. Madadi-Kandjani and A. Passalacqua. An extended quadrature-based moment method with log-normal kernel density functions. *Chemical Engineering Science*, 131:323–339, 2015. doi: 10.1016/j.ces.2015.04.005.

[81] M. Manninen, V. Taivassalo, and S. Kallio. On the mixture model for multiphase flow. *Vtt Publications*, pages 1–67, 1996.

[82] D. L. Marchisio and R. O. Fox. Solution of population balance equations using the direct quadrature method of moments. *Journal of Aerosol Science*, 36(1):43–73, 2005. doi: 10.1016/j.jaerosci.2004.07.009.

[83] D. L. Marchisio, J. T. Pikturna, R. O. Fox, R. D. Vigil, and A. A. Barresi. Quadrature method of moments for population-balance equations. *AIChE Journal*, 49(5):1266–1276, 2003. doi: 10.1002/aic.690490517.

[84] D. L. Marchisio, R. D. Vigil, and R. O. Fox. Quadrature method of moments for aggregation-breakage processes. *Journal of Colloid and Interface Science*, 258(2):322–334, 2003. doi: 10.1016/S0021-9797(02)00054-1.

[85] Daniele L. Marchisio and Rodney O. Fox. *Computation Models for Polydisperse Particulate and Multiphase Systems*. Cambridge University Press, 2013. ISBN 9780521858489.

[86] A. E. Martell and R. M. Smith. *Critical Stability Constants*, volume 1. Plenum Press, New York, 1989. ISBN 0306352125. doi: 10.1007/978-1-4615-6761-5.

[87] A. Martynia, B. Wierzbowska, N. Hutnik, A. Mazienczuk, A. Kozik, and K. Piotrowski. Separation of Struvite from Mineral Fertilizer Industry Wastewater. *Procedia Environmental Sciences*, 18:766–775, 2013. doi: 10.1016/j.proenv.2013.04.103.

[88] J. H. McCabe. The Quotient-Difference Algorithm and the Pade Table: An Alternative Form and a General Continued Fraction. *Mathematics of Computation*, 41(163):183, 1983. doi: 10.2307/2007775.

[89] R. McGraw. Description of aerosol dynamics by the quadrature method of moments. *Aerosol Science and Technology*, 27(2):255–265, 1997. doi: 10.1080/02786829708965471.

[90] C. M. Mehta and D. J. Batstone. Nucleation and growth kinetics of struvite crystallization. *Water Research*, 47(8):2890–2900, 2013. doi: 10.1016/j.watres.2013.03.007.

[91] A. Mersmann. *Crystallization Technology Handbook*. Marcel Dekker Inc., New York, 2001. ISBN 0824705289.

[92] A. Miles and T. G. Ellis. Struvite precipitation potential for nutrient recovery from anaerobically treated wastes. In *Water Science and Technology*, volume 43, pages 259–266, 2001. doi: 10.1007/s13398-014-0173-7.2.

[93] D. M. Montag. *Phosphorrückgewinnung bei der Abwasserreinigung - Entwicklung eines Verfahrens zur Integration in kommunale Kläranlagen*. PhD thesis, RWTH Aachen University, 2008.

[94] F. M.M. Morel and J. G. Hering. *Principles and applications of aquatic chemistry*. John Wiley & Sons, Inc., New York, 1993.

[95] F. Moukalled and M. Darwish. A coupled finite volume solver for incompressible flows. *AIP Conference Proceedings*, 1048(January 2014):715–718, 2008. doi: 10.1063/1.2991028.

[96] F. Moukalled, L. Mangani, and M. Darwish. *The Finite Volume Method in Computational Fluid Dynamics: An Advanced Introduction with OpenFOAM® and Matlab®*, volume 113. Springer, 2015. ISBN 978-3-319-16873-9.

[97] J. W. Mullin. *Crystallization*. Elsevier, 2001. ISBN 0750648333. doi: 10.1021/op0101005.

[98] T. T. Nguyen, F. Laurent, R. O. Fox, and M. Massot. Solution of population balance equations in applications with fine particles: Mathematical modeling and numerical schemes. *Journal of Computational Physics*, 325:129–156, 2016. doi: 10.1016/j.jcp.2016.08.017.

[99] A. E. Nielsen. *Kinetics of Precipitation*, volume 18. Pergamon Press, 1964.

[100] K. N. Ohlinger, T. M. Young, and E. D. Schroeder. Kinetics Effects on Preferential Struvite Accumulation in Wastewater. *Journal of Environmental Engineering*, 125(8):730–737, 1999. doi: 10.1061/(ASCE)0733-9372(1999)125:8(730).

[101] K. N. Ohlinger, T. M. Young, and E. D. Schroeder. Postdigestion Struvite Precipitation Using a Fluidized Bed Reactor. *Journal of Environmental Engineering*, 126(4):361–368, 2000. doi: 10.1061/(ASCE)0733-9372(2000)126:4(361).

[102] A. A. Öncül, K. Sundmacher, and D. Thévenin. Numerical investigation of the influence of the activity coefficient on barium sulphate crystallization. *Chemical Engineering Science*, 60(19):5395–5405, 2005. doi: 10.1016/j.ces.2005.04.074.

[103] A. A. Öncül, K. Sundmacher, A. Seidel-Morgenstern, and D. Thévenin. Numerical and analytical investigation of barium sulphate crystallization. *Chemical Engineering Science*, 61(2):652–664, 2006. doi: 10.1016/j.ces.2005.07.037.

[104] A. A. Öncül, G. Janiga, and D. Thevenin. Comparison of Various Micromixing Approaches for Computational Fluid. *Industrial & Engineering Chemistry Research*, 48:999–1007, 2009. doi: 10.1021/ie800364k.

[105] A. Passalacqua, R. O. Fox, R. Garg, and S. Subramaniam. A fully coupled quadrature-based moment method for dilute to moderately dilute fluid-particle flows. *Chemical Engineering Science*, 65(7):2267–2283, 2010. doi: 10.1016/j.ces.2009.09.002.

[106] A. Passalacqua, J. Heylmun, M. Icardi, P. Bachant, and X. Hu. OpenQBMM, 2017.

[107] A. Passalacqua, F. Laurent, E. Madadi-Kandjani, J. C. Heylmun, and R. O. Fox. An open-source quadrature-based population balance solver for OpenFOAM. *Chemical Engineering Science*, 176:306–318, 2018. doi: 10.1016/j.ces.2017.10.043.

[108] L. Pastor, D. Mangin, R. Barat, and a. Seco. A pilot-scale study of struvite precipitation in a stirred tank reactor: Conditions influencing the process. *Bioresource Technology*, 99(14):6285–6291, 2008. doi: 10.1016/j.biortech.2007.12.003.

[109] S. V. Patankar. *Numerical Heat Transfer and Fluid Flow*. CRC press, 1980. ISBN 9788578110796.

[110] J. T. Pikturna. *Particle size prediction in reactive precipitation processes*. PhD thesis, Iowa State University, 2004.

[111] W. H. Press, S. Teukolsky, W. T. Vetterling, and B. P. Flannery. *Numerical Recipes 3rd Edition: The Art of Scientific Computing*, volume 1. Cambridge University Press, 2007. ISBN 0521880688. doi: 10.1137/1031025.

[112] J. Prywer, A. Torzewska, and T. Plociński. Unique surface and internal structure of struvite crystals formed by Proteus mirabilis. *Urological Research*, 40 (6):699–707, 2012. doi: 10.1007/s00240-012-0501-3.

[113] Md. S. Rahaman, D. S. Mavinic, A. Meikleham, and N. Ellis. Modeling phosphorus removal and recovery from anaerobic digester supernatant through struvite crystallization in a fluidized bed reactor. *Water Research*, 51:1–10, 2014. doi: 10.1016/j.watres.2013.11.048.

[114] Md M. Rahman, Ying Hao Liu, Jung Hoon Kwag, and Chang Six Ra. Recovery of struvite from animal wastewater and its nutrient leaching loss in soil. *Journal of Hazardous Materials*, 186(2-3):2026–2030, 2011. doi: 10.1016/j.jhazmat.2010.12.103.

[115] D. Ramkrishna. *Population Balances Theory and Applications to Particulate Systems in Engineering*. Academic Press, 2000. ISBN 0125769709.

[116] A. D. Randolph and M. A. Larson. *Theory of Particulate Processes*. Academic Press, 1988. ISBN 0125796528.

[117] S. Regy. *Phosphate Recovery By Stuvite Precipitation in a Stirred Reactor*. PhD thesis, 2001.

[118] M. Riella, R. Kahraman, and G. R. Tabor. Reynolds-Averaged Two-Fluid Model prediction of moderately dilute fluid-particle flow over a backward-facing step. *International Journal of Multiphase Flow*, 106(June):95–108, 2018. doi: 10.1016/j.ijmultiphaseflow.2018.04.014.

[119] H. Rusche. *Computational Fluid Dynamics of Dispersed Two-Phase Flows at High Phase Fractions*. PhD thesis, Imperial College of Science, Technology and Medicine, 2002.

[120] H. V. Rutishauser. Dcr Quotienten-Differenzen-Algorithmus. *Zeitschrift fur angewandte Mathematik und Physik ZAMP*, V(3):233–251, 1954.

[121] B. Selma, R. Bannari, and P. Proulx. Simulation of bubbly flows: Comparison between direct quadrature method of moments (DQMOM) and method of classes (CM). *Chemical Engineering Science*, 65(6):1925–1941, 2010. doi: 10.1016/j.ces.2009.11.018.

[122] M. S. Shalaby. Modeling and Optimization of Phosphate Recovery from Industrial Wastewater and Precipitation of Solid Fertilizer using Experimental Design Methodology. *Chemical and Biochemical Engineering Quarterly Journal*, 29(1):35–46, 2015. doi: 10.15255/CABEQ.2014.2107.

[123] A. Shokouhi. *Phosphorus Removal from Wastewater through Struvite Precipitation*. PhD thesis, Norwegian University of Life Sciences, 2017.

[124] V. L. Snoeyink and D. Jenkins. Water chemistry, 1980.

[125] O. Söhnel and J. Garside. *Precipitation: basic principles and industrial applications*. Butterworth-Heinemann, Oxford, 1992.

[126] Y. Song, P. Yuan, B. Zheng, J. Peng, F. Yuan, and Y. Gao. Nutrients removal and recovery by crystallization of magnesium ammonium phosphate from synthetic swine wastewater. *Chemosphere*, 69(2):319–324, 2007. doi: 10.1016/j.chemosphere.2007.06.001.

[127] B. L. Sørensen, O. L. Dall, and K. Habib. Environmental and resource implications of phosphorus recovery from waste activated sludge. *Waste Management*, 45:391–399, 2014. doi: 10.1016/j.wasman.2015.02.012.

[128] I. Stratful, M. D. Scrimshaw, and J. N. Lester. Removal of struvite to prevent problems associated with its accumulation in wastewater treatment works. *Water environment research : a research publication of the Water Environment Federation*, 76(5):437–43, 2001. doi: 10.2175/106143004X151491.

[129] K. Suzuki, Y. Tanaka, K. Kuroda, D. Hanajima, Y. Fukumoto, T. Yasuda, and M. Waki. Removal and recovery of phosphorous from swine wastewater by demonstration crystallization reactor and struvite accumulation device.

Bioresource Technology, 98(8):1573–1578, 2007. doi: 10.1016/j.biortech.2006.06.008.

[130] I. Takács, G. G. Patry, and D. Nolasco. A dynamic model of the clarification-thickening process. *Water Research*, 25(10):1263–1271, 1991. doi: 10.1016/0043-1354(91)90066-Y.

[131] A. W. Taylor, A. W. Frazier, and E. L. Gurney. Solubility products of magnesium ammonium and magnesium potassium phosphates. *Transactions of the Faraday Society*, 59:1580–1584, 1963. doi: 10.1039/tf9635901580.

[132] O. Ubbink. *Numerical prediction of two fluid systems with sharp interfaces*. PhD thesis, 1997.

[133] V. Vikas, Z.J. Wang, A. Passalacqua, and R.O. Fox. Realizable high-order finite-volume schemes for quadrature-based moment methods. *Journal of Computational Physics*, 230(13):5328–5352, 2011. doi: 10.1016/j.jcp.2011.03.038.

[134] V. Vikas, Z.J. Wang, and R.O. Fox. Realizable high-order finite-volume schemes for quadrature-based moment methods applied to diffusion population balance equations. *Journal of Computational Physics*, 249:162–179, 2013. doi: 10.1016/j.jcp.2013.05.002.

[135] R. Webster. An algebraic multigrid solver for Navier-Stokes problems. *International Journal for Numerical Methods in Fluids*, 18(8):761–780, 1994. doi: 10.1002/fld.1650180805.

[136] H. Wei and J. Garside. Application of CFD Modelling to Precipitation Systems. *Chemical Engineering Research and Design*, 75:219–227, 1997. doi: 10.1205/026387697523471.

[137] H. G. Weller. Derivation, Modelling and Solution of the Conditionally Averaged Two-Phase Flow Equations. Technical report, Imperial College of Science, Technology and Medicine, 1999.

[138] J. C. Wheeler. MODIFIED MOMENTS AND GAUSSIAN QUADRATURES. *Rocky Mountain Journal of Mathematics*, 4(1):287–296, 1974. doi: 10.1088/1126-6708/2009/09/011.

[139] D. L. Wright. Numerical advection of moments of the particle size distribution in Eulerian models. *Aerosol Science*, 38:352–369, 2007. doi: 10.1016/j.jaerosci.2006.11.011.

[140] L. D. Xavier, M. C. Cammarota, L. Yokoyama, and I. Volschan. Study of the recovery of phosphorus from struvite precipitation in supernatant line from anaerobic digesters of sludge. *Water Science and Technology: Water Supply*, 14(5):751–757, 2014. doi: 10.2166/ws.2014.033.

[141] J. Xue, F. Chen, N. Yang, and W. Ge. Eulerian-Lagrangian simulation of bubble coalescence in bubbly flow using the spring-dashpot model. *Chinese Journal of Chemical Engineering*, 25(3):249–256, 2017. doi: 10.1016/j.cjche.2016.08.006.

[142] W. C. Yan, Z. H. Luo, and A. Y. Guo. Coupling of CFD with PBM for a pilot-plant tubular loop polymerization reactor. *Chemical Engineering Science*, 66 (21):5148–5163, 2011. doi: 10.1016/j.ces.2011.07.004.

[143] Y. Yang, N. Nakada, R. Nakajima, M. Yasojima, C. Wang, and H. Tanaka. pH, ionic strength and dissolved organic matter alter aggregation of fullerene C60 nanoparticles suspensions in wastewater. *Journal of Hazardous Materials*, 244-245:582–587, 2013. doi: 10.1016/j.jhazmat.2012.10.056.

[144] X. Ye, Y. Gao, J. Cheng, D. Chu, Z. Ye, and S. Chen. Numerical simulation of struvite crystallization in fluidized bed reactor. *Chemical Engineering Science*, 176:242–253, 2018. doi: 10.1016/j.ces.2017.10.048.

[145] Xin Ye, Dongyuan Chu, Yaoyin Lou, Zhi Long Ye, Ming Kuang Wang, and Shaohua Chen. Numerical simulation of flow hydrodynamics of struvite pellets in a liquid-solid fluidized bed. *Journal of Environmental Sciences (China)*, 57:391–401, 2016. doi: 10.1016/j.jes.2016.11.019.

[146] Zhilong Ye, Yin Shen, Xin Ye, Zhaoji Zhang, Shaohua Chen, and Jianwen Shi. Phosphorus recovery from wastewater by struvite crystallization: Property of aggregates. *Journal of Environmental Sciences*, 26(5):991–1000, 2014. doi: 10.1016/S1001-0742(13)60536-7.

[147] G. H. Yeoh, C. P. Cheung, and J. Tu. *Multiphase Flow Analysis Using Population Balance Modeling: Bubbles, Drops and Particles*. Butterworth-Heinemann, Oxford, 2009. ISBN 0009-2509. doi: 10.1002/aic.

[148] K. Yetilmezsoy and Z. Sapci-Zengin. Recovery of ammonium nitrogen from the effluent of UASB treating poultry manure wastewater by MAP precipitation as a slow release fertilizer. *Journal of Hazardous Materials*, 166(1): 260–269, 2009. doi: 10.1016/j.jhazmat.2008.11.025.

[149] C. Yuan, F. Laurent, and R. O. Fox. An extended quadrature method of moments for population balance equations. *Journal of Aerosol Science*, 51: 1–23, 2012. doi: 10.1016/j.jaerosci.2012.04.003.

[150] T. Zhang, L. Ding, and H. Ren. Pretreatment of ammonium removal from landfill leachate by chemical precipitation. *Journal of Hazardous Materials*, 166(2-3):911–915, 2009. doi: 10.1016/j.jhazmat.2008.11.101.